

UNIVERSITÀ DEGLI STUDI DI PADOVA

Dipartimento di Fisica e Astronomia “Galileo
Galilei”

Corso di Laurea Magistrale in Fisica

Study of light-driven phenomena in integrated Opto-Microfluidic Lithium Niobate platforms

Laureando
Lorenzo De Bortoli

Relatore
Prof.ssa **Cinzia Sada**

Correlatore
Dr. **Riccardo Zamboni**

A.A. 2016-2017

Abstract

In last decades microfluidics has gained an increasing interest by the scientific community due to its capability of control liquids on the microscale. Especially, droplet microfluidics technology provides a high manipulation level on very small volumes of fluids. This feature makes it a promising candidate for biological, medical and chemistry applications. With a compact and simple microfluidic device, droplets can be coalesced, mixed, sorted and employed either as micro chemical reactors or as carriers of biological sample.

From the experimental point of view there are many ways to produce and see micro droplets. The device used for this thesis consists of an opto-microfluidic chip made of lithium niobate, in which are integrated a microfluidic circuit and an optical waveguide, normal to the channel and produced by titanium diffused in lithium niobate. Droplets flowing in the channel are detected using a laser light transmitted in the optical waveguide. After having illuminated the microfluidic channel, where a "train" of water droplets in oil pass through, the light is collected by another waveguide facing on the other side of the channel: the intensity transmitted is recorded by way of a tailored electronic circuit. The water droplet in oil makes the signal of the light transmitted beam change in intensity, from a fixed value, relative to oil, to another basically due to the different refractive index of the droplet respect the surrounding flux. The signal variation is not sharp, but is preceded by a peak of intensity. Thus, the acquisition profile of the transmitted light intensity identifies the phenomenon of droplet passage, but up to now no studies were reported from a theoretical point of view. In this thesis, we aimed to clarify this aspect and provide a fine comprehension of it. Therefore, we correlated the curves obtained to some physical parameters of the droplets and to give a theoretical explanation to the shape of such a profile.

Since the length and the velocity of the droplets are proportional to the ratio of the liquids' fluxes flowing in the microfluidic channel, it is possible to measure and analyse the effect of the droplet passage and find new physical observables to identify the droplet, its shape and relative velocity. In particular, since the optical transmitted light across the droplet presents intensity modulation, great care was devoted to identifying their origin and their systematic behaviour. The aim was that of relating the modulation intensity peaks to the meniscus of the droplet and then to investigate all the other zones in its middle with an accurate phenomenological analysis. The idea that features in the light transmitted intensity signal could be

related with the meniscus of the droplet, as well as intuitive, has never proved in literature and has confirmed by a simulation carried out in the frame of this thesis. In fact, a theoretical analysis of this phenomena is made: assuming ray optic, two-dimensional version of the problem and after having chosen the best shape for the source, a program that simulate the passage of a droplet in the microfluidic channel was written. After having simulates the physical interaction between the droplet that advances in the channel and the light exiting the waveguide, the software computes the transmitted intensity in order to reproduce the acquisition profile. The numerical profiles thus obtained are reported and commented, also by varying the parameters of the simulation. Finally, comparisons between the results of the simulations and the experimental profiles enable us to understand better the shape of the droplet. Based on these results we analysed also the shape that the interface water-oil should be in order to reproduce the low transmitted intensity typical of the droplet's centre.

Performing an accurate analysis over a wide range of the fluxes ratio $\phi = \frac{Q_{oi}}{Q_{water}}$ also the role of the so called "secondary peaks" is investigated and fingerprints for a detailed description of the transmitted intensity profile are provided. This, up to our knowledge, has not been investigated yet. Finally, we can identify the droplet passage, so that to estimate its length with perspectives of setting up an automatized and fast data analysis procedure. This feature exploits an integrated opto-microfluidic device, independent from the standard imagining processes and with the possibility to perform a feedback loop with manipulation stages.

Moreover, the same measures, with a one-to-one comparison with synchronous acquisitions of microscope images of the droplets, let us investigate also the sensibility of the optical transmitted light from the overall geometrical shape of the droplet. New physical observables in the acquisition profile allow us to describe and identify the transition from different production regimes of the droplets, also in different geometrical configuration of the microchannels, in a more accurate way than other imaging technique presented in literature.

Contents

Introduzione	1
1 Optofluidic device in Lithium Niobate	5
1.1 Microfluidic channel and droplet generation	7
1.1.1 Droplet microfluidic	8
1.1.2 Theoretical model for the T-junction	10
1.1.3 Microchannel realization in Lithium Niobate	13
1.1.4 Lithium niobate wettability	14
1.2 Waveguides in Lithium Niobate	17
1.2.1 Titanium diffusion	17
1.2.2 Near field (NF) characterization	19
1.3 Device realization	20
1.3.1 Experimental apparatus and droplet detection	22
1.3.2 Data acquisition and analysis	23
1.4 Experimental results	25
2 Droplet simulation	35
2.1 The simulation software	35
2.2 Simulations with interference	41
2.3 Comparison with experimental data	43
2.4 Role of the parameters	44
2.4.1 Dependence on the non physical parameters	45
2.4.2 Dependence on droplet shape	51
2.5 Center of the droplet	54
3 Analysis of droplet shape	59
3.1 Role of the "secondary peaks"	69
3.2 High production frequency analysis	72
3.3 Droplet's shape evolution dynamics	77
3.3.1 Droplet as a lens	79
3.3.2 Spherical droplets	81
3.4 Reconstruction of droplet shape	83
Conclusione	87
Bibliography	89

Introduction

Opto-microfluidics consists of integrating microfluidic and microphotonic components onto the same platform, where fluid and light are driven to interact. This combination offers new opportunities for a large variety of applications [1, 2, 3]: among the others, effective compact bio-sensors have attracted great attention because they combine the high sensitivity of micro-photonic devices to the properties of small amounts of fluids that surround them [4, 5]. Microfluidics was originally developed for ink-jet printing and, later, in biotechnology [4, 5, 6] and in micro-analytical chemistry [7]. As a matter of fact, reagents can be strongly reduced from millilitres and microliters to nanolitres and femtolitres whereas hours of reaction time could be decreased to mere seconds or less. Due to the strong advances in fluid handling techniques at the micron scale, sophisticated microfluidic networks were realized, including all kinds of devices (like pumps, valves, fluid mixers and microchannels) to manipulate, deliver and control fluids within one compact chip [8, 9]. On this basis, the lab-on-a-chip technology has known a broad success, by allowing several biological analysis and diagnosis to be conducted in parallel onto miniaturized and planar micro-fluidic platforms. Optofluidic integration could represent a further development of the lab-on-a-chip technology [9]: this has actually driven most of the current works and efforts for integrating the optical devices that are usually implemented in biological and chemical detection schemes (like optical light sources and photodetectors) onto compact and planar optofluidic platforms [3]: in this field, the incorporation of chemical and physical sensors perfectly integrated with the microfluidic circuit is under debate [10] as well as the possibility of monolithical integration is still far from being available. Among all the characteristics required to optofluidic integration, compactness and tunability were addressed as key features to achieve a high degree of functionality and large-scale integration. A broad range of highly flexible optofluidic devices were therefore presented to bring new tools in integrated optics applications, like tunable attenuators, optofluidic lasers and light sources, tunable filters, optical switches and tunable interferometers [11, 12, 13, 14]. In parallel, a new class of optically controlled photonic devices were also demonstrated to optically manipulate micronscale dielectric objects within fluid environment through tightly focused laser beams, such as optical tweezers and stretchers, as well as traps and sorters that were applied: in this case, the micro-elements were mainly microspheres, tapered fibers and biological targets as cells. In most cases the proposed devices exploited hybrid configurations and were designed to provide only one specific investigation such as mechanical response upon stretching [15, 16, 17] or target movement in a given direction to get sorting being the most wide-spread and tracing by way of

imaging techniques [14]. In particular, single-cells' mechanical properties were also investigated, providing information on "local properties" of the cells [17, 18] with some investigation on the cellular deformation which can be studied by exploiting an optical stretcher (OS) [19]. In general it emerged that to make significant progress in the field of biology and microfluidics, it is necessary to understand the complexity of the microenvironment of the cells, since results obtained in static two-dimensional cell cultures do not have the power to predict events that occur within a dynamic environment, e.g. cellular stress and toxicity of drugs in the systems of co-cultivation cell and biocompatibility of synthetic materials used [20, 21]. The best way to do this is to use microfluidics to control the environment. It is worth mentioning that many efforts were applied to the application of microfluidics for biological issues, with special attention to cell's investigation or biological reactions. When the biological targets have small dimensions, standard technique are those mostly exploited whilst microfluidics and opto-microfluidics still remained un-investigated tools of analysis. In these cases, the microfluidic circuit was mostly realised on a given flexible and easily-moulded material (mainly polymers PDMS, PMMS) while optical features were either performed by external optical fibers therein integrated/coupled or re-alised on solid substrates (glass, silica, ..) to which the microfluidic circuitic is bonded [22, 23] with technologies that were not reconfigurable nor tunable. Furthermore, when hybrid configuration were used, stability and careful alignment of the different components was a critical issue especially for measurements reproducibility. Only recently it was proposed the first monolithic, perfectly aligned, robust and portable optofluidic device suitable for real medical analysis, where both microfluidic circuits and optical waveguides are simultaneously fabricated on a glass substrate by femtosecond laser micromachining (FLM) [24, 25]. Although the main advantages of FLM technology [26] are the possibility to create both optical waveguides [27] and microfluidic channels (if combined with chemical etching [28, 29]) and also its extreme 3D-flexibility that allows fabricating microchannels with Y-junctions or variable cross-sections, again the features of the device, once planned, remain fixed. Up to now, neither light-reconfigurable or devices or multifunctional stages have proposed yet as well as system that activate a function in real time depending on the other stages feedback. This is true even when droplet-based device were investigated, i.e. focusing on the creation of discrete volumes with the use of immiscible phases. Thanks to its scalability and parallel processing, in fact, even the droplets microfluidics has been used in a wide range of applications including the synthesis of biomolecules, drug delivery and diagnostic testing and bio-sensing [30]. Although continuous flow devices offer fine control over flow characteristics, scaling up is a challenge as the size of devices scales almost linearly with the number of parallel experiments. Droplet microfluidics has the ability to perform a large number of reactions without increasing device size or complexity [31] and a high versatility connected to the generation and manipulation of discrete droplets inside micro-devices. Different methods have been devised that produce highly monodisperse droplets in the nanometer to micrometer diameter range, at rates of up to twenty thousand per second. Due to high surface area to volume ratios at the microscale, heat and mass transfer times and diffusion distances are shorter, facilitating faster reaction times. Unlike continuous-flow systems, droplet-based microfluidics allows also for independent control of each droplet, thus generating micro-reactors that can be individually transported, mixed, and analysed [32].

In this scenario, the integration of a large number of different stages on a single substrate chip is a key point for promoting new insights in many applications that need portable devices to speed the analysis and allow investigation of new phenomena [33]. Among the others, lithium niobate (LiNbO_3) crystals have been proposed in microfluidics application since it demonstrated to be bondable to other polymeric materials and allows for high efficient surface acoustic waves (SAW) generation to move droplets on the substrate in a very controlled way. Recently, in fact, micro-pumps based on the piezoelectric properties of LiNbO_3 have been reported to move the liquid in a closed square loop channel and flow mixing, pyroelectric and photogalvanic particle trapping [34] were proposed. Quite surprisingly, all the above mentioned applications were realized without producing a microfluidic circuit directly on LiNbO_3 substrates (apart from [35]) and without the integration of optical sensing stages or complex multifunctionals platform although it is a material thoroughly exploited in the photonic and integrated optics industry. As a matter of fact lithium niobate can host high quality optical waveguides and complex devices such as multiplexer, switch and optical modulators are commercially available thanks to its high wide transparency (75% from 350-3450nm): the Ti in – diffusion technique [36] is routinely employed together with standard photolithography for the production of optical circuit as well as ion implantation [36]. Moreover, diffractive optical elements, such as gratings, were designed exploiting its photorefractive effect (i.e a suitable inhomogeneous illumination induces in the material a correlated modification in the refractive index due to the electro-optic effect) [37]. This property is strongly enhanced by local doping with metal impurities with two valence states such as iron and copper [37]. Up to now the investigation on this field was mainly focused on bulk doped LiNbO_3 crystals but, recently, the interest in the local doping has been increasing thanks to its versatility and integration with other optical functionalities.

The final objective of the main project in which this thesis was carried out is to develop a new concept of a portable and reconfigurable opto-microfluidic platform that can be optically designed in different but even complementary Lab-on-chip systems, triggered by optical real-time feedbacks and addressed to develop new label-free tools for targets' isolation and investigation as well as collective induced behaviours. It comprehends the design and realization that integrates in the same substrate and in a monolithically way different stages by combining: sample preparation, label-free tracing, analysis, sensing and storage of the biological target (namely cells) to be investigated. The key element of novelty relies on the exploitation of light/field-induced interactions with the material thanks to the light confinement in optical waveguides that are designed to illuminate the fluid fluxing in microfluidic channels and to collect the light therefore transmitted. Measures of optical transmission allow not only to estimate the fluid absorbance, its refractive index but also to detect the passage of "objects" eventually dispersed in the fluid such as biological cells or droplets.

In this frame of reference, the interaction features of the light exiting from an optical waveguides and crossing the fluid to be then collected into another optical waveguide is of paramount importance to identify the fluid as well as dispersed phases in there dispersed. Basically, a description of the physical phenomena occur-

ring have not been studied yet and consequently the data recording of the optical transmission in this opto-microfluidic is still unknown.

The objective of this thesis is exactly to give a physical explanation and to find fingerprints for a detailed analysis of the trasmission optical profile, that up to our knowledge has not been investigated yet.

The contents are distributed as follows:

- In **Chapter 1** a description of droplet microfluidic is performed, as well as a brief summary of the main techniques to engrave microchannels and produce wavelenght in LiNbO_3 . Moreover, a sketch of the experimental apparatus and examples of optical acquisition profiles are presented. Finally, an analysis of the droplet length over a wide range of fluxes ratio ϕ is performed.
- In **Chapter 2** the first objective of this thesis is reached. Using a code, specifically written to simulate the interaction between waveguided light and water droplet in oil, we demonstrate the physical meaning of two important zones of the acquisition profile.
- In **Chapter 3** the optical acquisition profiles, compared with the microscope images of the droplet, are presents for a wide range of ϕ and employed to reach plenty of relevant results, such as the transition from two production regimes of the droplet and the comprehension of the remaining part of the acquisition profile not yet explained.

Chapter 1

Optofluidic device in Lithium Niobate

Lithium niobate is a synthetic material, described for the first time by Zachariasen and widely investigated by Nassau and Abrahams at Bell Laboratories in the sixties. It is a solid, transparent material not soluble in water or organic solvents.

Lithium niobate is a crystal, which exhibits a mirror symmetry about three planes that are 60° apart, that can be seen in Figure 1.1.

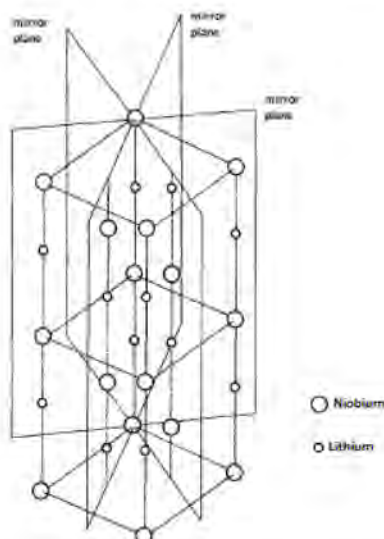


Figure 1.1: Orthohexagonal cell of LiNbO_3 with the three mirror plane symmetry.

Three-fold rotational symmetry around the axis in intersection of these three planes. These symmetries classify LiNbO_3 in the space group $R\bar{3}c$, with point group $3m$. There are three different cells that can be chosen: hexagonal, rhombohedral and orthohexagonal. In literature authors usually refer to the orthohexagonal one, which are reported in Figure 1.1. Anyway, in Figure 1.2, the hexagonal and rhombohedral unit cells together with a comparison of the two has been reported.

The orthohexagonal cell is described by three mutually orthogonal reference axes, defined as follow:

- the z -axis (also indicated as c -axis or optical axis) is the one around which the crystal exhibits its three-fold rotation symmetry;
- the y -axis is the one laying on the mirror plane;

- the x -axis is the one perpendicular to others.

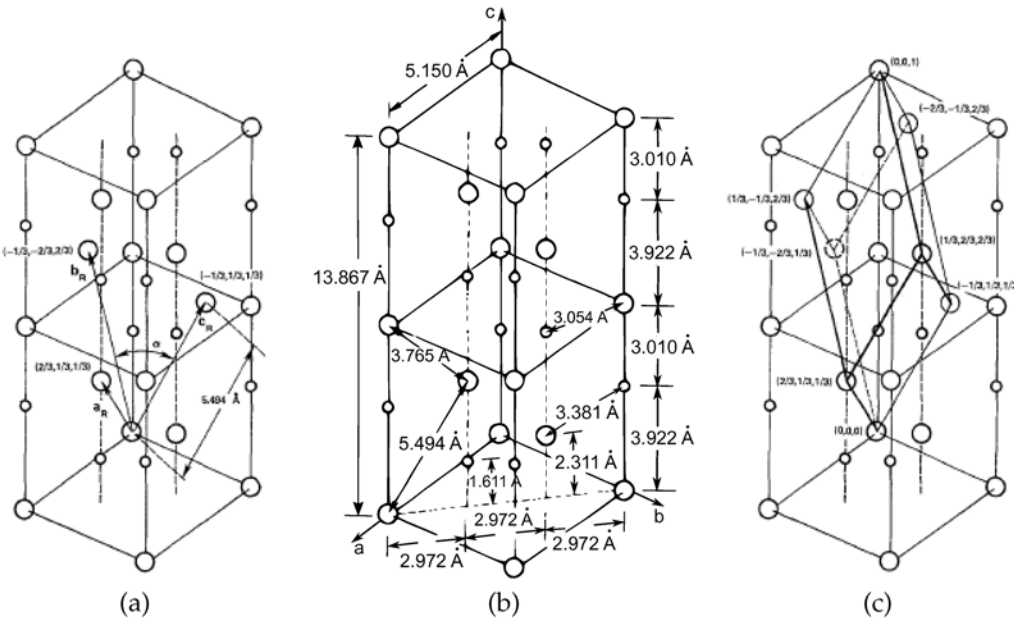


Figure 1.2: **Rhombohedral and hexagonal unit cells.** Rhombohedral cell (a); hexagonal cell (b); comparison between rhombohedral and hexagonal cells (c).

Atomic structure of lithium niobate depends on ferroelectric or paraelectric phase of the crystal. The structure consists of planes of oxygen in a slightly distorted hexagonal close-packed configuration (see Figure 1.3). Octahedrals formed by this oxygens, are regularly filled by lithium atoms, niobium and vacancy, following this order along c axis. Below Curie temperature ($T_C \sim 1160^\circ \text{ C}$ in ferroelectric phase) lithium atoms are shifted by 44 pm from plane of oxygens and niobium atoms by 27 pm from the centre of octahedra. The spontaneous polarization of ferroelectric phase is caused by these shifts. While in paraelectric phase both shifts of lithium and niobium are zero.

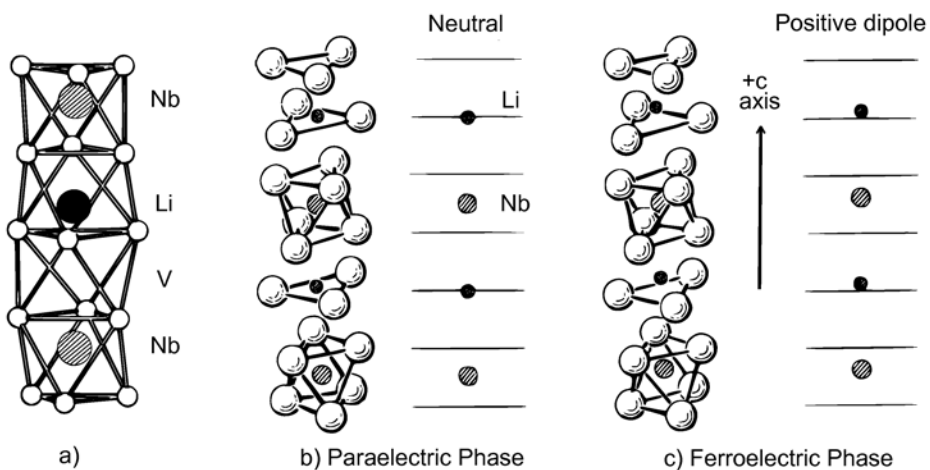


Figure 1.3: **Atomic structure of LiNbO_3 in paraelectric and ferroelectric phases.** In (a) white dots represent oxygen atoms, forming the planes and he regular filling with niobium, vacancy and lithium is showed. In (b) and (c) are presented the shift of the atoms.

Due to the crystallographic structure and the symmetry properties of lithium niobate, its permittivity tensor, in the orthohexagonal cell reference framework, is anisotropic. It can be represented by a 3×3 matrix with the form:

$$\bar{\epsilon} = \begin{bmatrix} \epsilon_{11} & 0 & 0 \\ 0 & \epsilon_{22} & 0 \\ 0 & 0 & \epsilon_{33} \end{bmatrix} \quad (1.1)$$

This leads to its characteristic optical property: the *birefringence*. Two refractive indices can be defined, depending on the orientation of electric field: ordinary one $n_o = \sqrt{\epsilon_{11}/\epsilon_0}$ (electric field perpendicular to the z-axis of the crystal), extraordinary one $n_e = \sqrt{\epsilon_{33}/\epsilon_0}$ (electric field parallel to the z-axis), where ϵ_0 is the vacuum electric permittivity.

Both indices are function of the wavelength λ of the incident light. At room temperature and with $\lambda = 632.8$ nm their values are: $n_o = 2.2866$ and $n_e = 2.2028$.

Impurities and structural modifications are extremely important in the study of lithium niobate since they can modify considerably its physical properties. For example both the refractive indices (n_o and n_e) are strongly dependent on the extrinsic impurities and can be tailored by doping the crystal. This is an advantage for our scopes, because the doping with titanium allow for the realization of optical waveguides (and so, for the creation of a fully integrated optofluidic device).

1.1 Microfluidic channel and droplet generation

Microfluidics is the research field that studies, controls and manipulates the dynamics extremely small amounts of fluids, with volumes from tens of nanolitres down to picolitres, flowing inside confined geometries with a characteristic length of the order of tens of micrometres or less. It is characterized by low value of the Reynolds number Re , typically lower than one hundred ($Re < 100$).¹ In these conditions laminar flow is established and no mixing happens, allowing an excellent control of fluids. Moreover, microfluidics provides an extremely steady control on the manipulated samples and a very low reagents consumption. For these reasons, since its birth, microfluidics has been employed in a wide range of application, from chemical synthesis to information technology, from biological analysis to drug delivery [38].

The more promising field of microfluidics is the Lab-On-a-Chip (LOC) technology, as Betella writes in [38]. The aim of a LOC is to transfer all laboratory operations into small portable microfluidic devices.

Many micro-devices that are able to pull the fluids inside the channels and to manipulate small amounts of liquids have been already realized, but it is still a challenge the integration of all of them in a single multi-purpose micro-device. Moreover they usually need macro syringe pumps or pressure controllers to operate and finally the analysis is carried out putting the chip under the objective of a "big" microscope.

¹Where $Re = \frac{\rho \mu L}{\eta}$ with: ρ is density of fluid, μ the mean velocity, L a linear dimension of the flow and η is the dynamic viscosity of the fluid. So, Reynolds number indicate the ratio between inertial and viscous forces.

In Bettella's PhD thesis [38] is described the realization of a fully integrated opto-microfluidic platform on lithium niobate, with provides, in the same material, a microfluidic stage and an optical stage for the analysis. In this thesis work all the measures are taken using this device, briefly illustrated in this chapter.

1.1.1 Droplet microfluidic

The characteristic dimension of a microfluidic channel normally ranged from $10 \mu\text{m}$ to $300 \mu\text{m}$ and the typical fluid velocity usually does not exceed 1 m/s . This allows the Reynolds number to be always below 100, so the typical regime of microfluidic experiments is the laminar flow. This actually makes molecular diffusion the only way for mixing different fluids. This could be a problem if we want to perform fast reactions.

The solution is to confine the fluids of interest inside droplets surrounded by another immiscible fluid phase used to carry the droplets along the microfluidic channels. Due to the turbulent nature of the fluid inside the droplet [39, 40, 41, 42] reaction can be performed. These particular features of droplets have made microfluidics effectively employable in a broad range of applications.

The fluids that make up the droplets is generally called the *dispersed phase*, while the outer fluid surrounding the droplets is called the *continuous phase*.

A wide variety of techniques have been developed to produce droplets inside a microfluidic chip. All of them are linked by the fundamental requirements of *high reproducibility* and *very low dispersion* in volume contribution [38].

As Bettella extensively discusses, the methods can be divided in two distinct typologies: *passive* methods and *active* methods.

- *Passive methods* are merely based on the interaction between two immiscible fluids constrained in confined geometry and the generation of droplets does not require any contribution from specific energy sources. The properties of the droplets are tailored just by the control of inlet fluxes or pressure of the fluids. Realizing these methods need an accurate geometrical design of the microfluidic channels, a suitable choice of the fluids employed and selected wettability properties of the materials.
- *Active methods*, on contrary, need the exploitation of an external source of energy for the generation of droplets. In Bettella's work many of these techniques have been presented.

Passive methods constitute the simplest way to produce droplets with a high control on their volume and, for this reason, are often preferred to active methods. A more detailed description of the passive methods will be presented below.

All type of passive methods require the control either on the fluxes of the continuous phase (Q_c) and the dispersed phase (Q_d) or on their inlet pressure (p_c and p_d) [38]. Moreover, the most important feature of such a generator is the *geometry* of the channels. In Figure 1.4 we can see the three most important configurations: *co-flowing*, *flow-focussing* and *cross-flowing*.

- *Co-flowing configuration:* the geometry is characterized by two coaxial channels with the innermost that interrupts. The dispersed phase flows in the inner channel, while the continuous flows in the outer one. When the dispersed phase emerges from the inner channel, after an initial stage where it flow together with the continuous one, droplets are formed by Rayleigh-Plateau instability; [38]
- *Flow-focussing configuration:* The channel are arranged in a cross and the continuous phase, that flows in the arms, shrinks symmetrically the dispersed phase, that flows in the main channel, until pinch-off is reached. With this geometry an high stability over a wide range of droplet production frequencies is obtained; [38]
- *Cross-flowing configuration:* the channel containing the dispersed phase, crosses at a wide angle the main channel, where the continuous phase is flowing. The dispersed phase obstruct the main channel interrupting the continuous phase stream before droplet break-up takes place. In the subsection below, this problem will be debated better. Different geometries have been studied, as T-junction (discussed below), Y-junction and multiple junction. [38, 43, 44, 45].

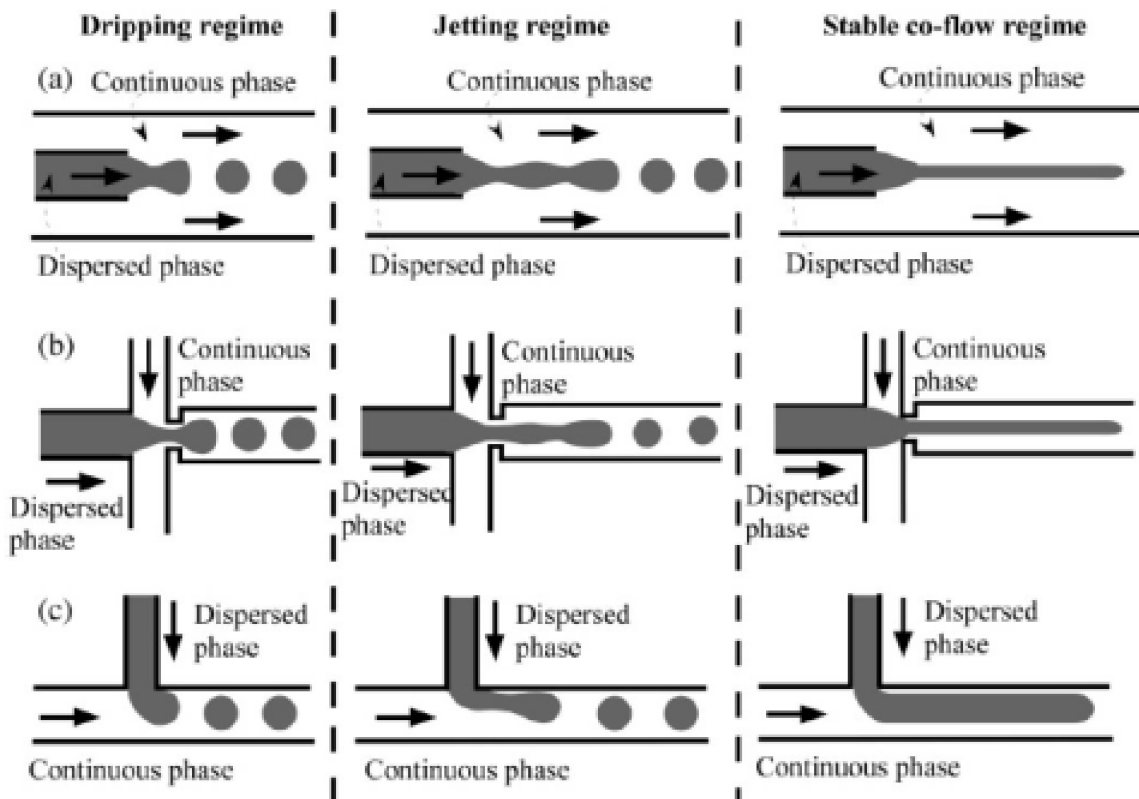


Figure 1.4: **The three configurations** [38]: (a) co-flowing; (b) flow-focussing; (c) cross-flowing. The three typical operational regimes (*dripping*, *jetting* and *coflow*) are shown from the left to the right.

In general, depending on the physical properties of the fluids (such as densities ρ_c and ρ_d , viscosities μ_c and μ_d and interfacial tension σ) or on other parameters

(such as the fluxes of the continuous and dispersed phase Q_c and Q_d , the wettability properties, the contact angle with the channel surface θ_c and θ_d) the device can operate in three different regimes (they too shown in Figure 1.4).

- *Co-flow*: in this regime the two phase flow parallel to each other and no droplets are formed. It occurs when the fluids velocities are small, interfacial tension is high and the viscosities are similar [38];
- *Jetting*: after an initial co-flow regime instability let the droplets form. This regime allows for a fast production of small droplet, but has also a wide volume dispersion [38]
- *Dripping*: the break-up takes place immediately and no co-flow regime is established. This regimes produces droplets at high frequency. [38]

In addition, there is another regime: the *squeezing*. It can be obtained at a low flux of the continuous phase and allows for the production of larger droplets, also indicated as *plugs*, which fill entirely the main channel. In Figure 1.5 we can see the production process in a T-junction working in the squeezing regime.

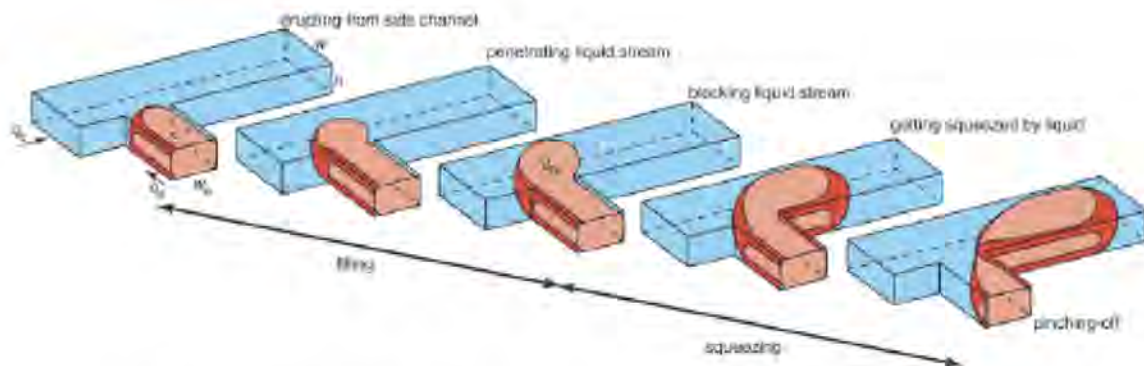


Figure 1.5: **Different stages of droplet generation in a T-junction, in the *squeezing* regime** [38]. First the dispersed phase emerges in the main channel blocking the flow of the continuous phase, then the increasing pressure shrinks the neck of the dispersed phase until breakup take place.

1.1.2 Theoretical model for the T-junction

We want now to provide a more detailed description of this geometry. In the T-junction, with the cross-flowing configuration, droplets are produced thanks to the forces exerted by the continuous phase on the dispersed one [38]. When the dispersed phase begins to occupy the channel, the continuous is forced to flow in a narrower gap, so its velocity increase and the pressure gradient across the tip and the neck (of the entering thread) grows gradually. The effect is an increase both in the *shearing viscous force* (proportional to the velocity of the continuous phase) and in the force driven by the *pressure gradient*. These two forces overcome on the *capillary force* (which tends to maintain attached the droplet at the thread of the dispersed phase) and when this happens, the break-up of the droplet occurs.

All the regimes and the physical processes that could happen are characterized by

different balances between the three forces mentioned above.

In this thesis work we are interested in the *dripping* and *squeezing* regimes, both in cross-flowing and flow-focussing configuration. In the dripping regime the main contribution to droplet pinch-off is the shearing viscous force, while in the squeezing the break-up is driven by the pressure gradient, since the dispersed phase obstructs completely the main channel, blocking the continuous phase. Therefore, an important parameter to distinguish between the two different regimes is the *capillary number* Ca [38]:

$$Ca = \frac{\mu_c v_c}{\sigma} \quad (1.2)$$

where μ_c and v_c are respectively the viscosity and the average velocity of the continuous phase, while σ is the interfacial tension. Ca expresses the ratio between the viscous shear stress and the capillary pressure, so greater is Ca and higher is the contribution of the viscous shear force, on contrary, smaller is Ca and more important is the role of the other forces.

The precise role of the capillary number, as a parameter to distinguish between the squeezing and dripping, were first provided by Garstecki *et al.* [46] and finally proved by the simulation of De Menech *et al.* [47]. They set the critical separation value at $Ca^* = 0.015$: at higher values of Ca dominates the viscous shear force and dripping regime is established, while at smaller values the biggest term is the squeezing pressure and the droplet occupy the entire width of the channel.

Independently on the regime, droplets are produced thanks to the three forces cited above. Different theories are under investigation, but the best fitting theory of experimental data is that of Christopher *et al.* [48].

They indicated h the height of the channels, w_c and w_d the widths of the continuous and dispersed phase channels respectively. In addition, they fixed Q_c and Q_d the fluxes of the two phases, and considered an emerging dispersed phase thread as sketched in Figure 1.6. The tip is depicted as a spherical shape with radius b connected to the dispersed phase by a neck with a width s (at the beginning of the process $s = w_d$). As authors suggest, breaking point starts when the three forces balance each other:

$$F_\sigma + F_\tau + F_p = 0 \quad (1.3)$$

where F_σ , F_τ and F_p are the just presented three forces that acts on the liquid-liquid interface. In addition they computed an approximate form for every force:

- **Capillary force:** it is given by the difference between Laplace pressures at the upstream and downstream ends of the emerging droplet (with an approximation of curvature), multiplied by the area of interface bh :

$$F_\sigma \sim \left[-\sigma \left(\frac{2}{b} + \frac{2}{h} \right) + \sigma \left(\frac{1}{b} + \frac{2}{h} \right) \right] bh = -\sigma h \quad (1.4)$$

- **Drag force:** it is the force generated due to viscous shear applied from continuous phase flowing on the emerging dispersed phase. The authors approximate the shear stress rate with the average velocity of continuous phase v_c divided by the gap size between the wall and the tip of the droplet $w_c - b$.

$$F_\tau \sim \eta_c \frac{v_{gap}}{w_c - b} bh \sim \eta_c \frac{Q_c b}{(w_c - b)^2} \quad (1.5)$$

- **Squeezing pressure force:** this force is obtained from a lubrication analysis [49] for the pressure during flow in a thin gap with aspect ratio $(w_c - b)/b$.

$$F_p \sim \Delta p_c b h \sim \frac{\eta_c v_{gap}}{w_c - b} \frac{b}{w_c - b} b h = \frac{\eta_c Q_c b^2}{(w_c - b)^3} \quad (1.6)$$

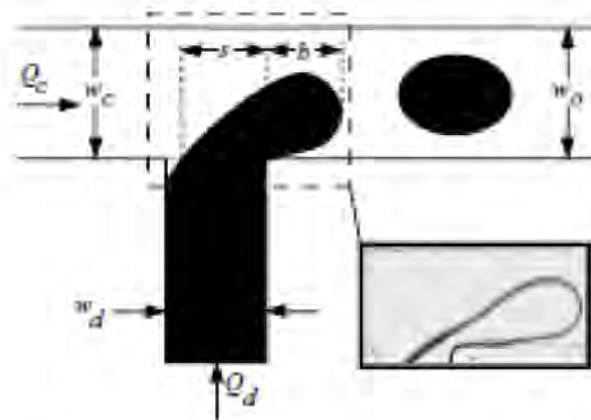


Figure 1.6: Schematic diagram of the emerging droplet taken from the paper of Christopher *et al.* [48].

From equation 1.2 and the approximations listed before, authors derived a scaling law for droplet length, frequency and volume. The result is that they depend on $\varphi = \frac{Q_d}{Q_c}$ and Ca .

The total droplet length is computed as the sum of the one before the neck starting shrinking through and an additional during neck shrinking, which authors approximate as $v_{growth} \cdot t_{squeeze}$, where $t_{squeeze} \approx \frac{w_d}{v_c} \approx \frac{w_d w_c h}{Q_c}$ and $v_{growth} = \frac{Q_d}{b h}$.

Length normalized to w_c was derived as a result of some easy algebraic passage:

$$\bar{L} = \bar{b} + \frac{\Lambda}{b} \varphi \quad (1.7)$$

where $\bar{b} = \frac{b}{w_c}$, $\bar{L} = \frac{L}{w_c}$ and $\Lambda = \frac{w_d}{w_c}$. With similar arguments they derived also the semi-empirical trend for frequency for constant value of φ :

$$\bar{f} = \frac{\eta_c w_c}{\sigma} f \propto Ca^{1-\delta} \quad (1.8)$$

and the trends of the rescaled volume:

$$\bar{V} = \frac{V}{w_c^2 h} = \bar{L} \bar{b} = \bar{b}^2 + \Lambda \varphi \quad (1.9)$$

which, for constant φ can be expressed in terms of Ca :

$$\bar{V} = \frac{\varphi Ca}{\bar{f}} \propto Ca^\delta \quad (1.10)$$

The exponents has been experimentaly determined in the range $10^{-3} < Ca < 5 \cdot 10^{-1}$ as $(1 - \delta) = 1.31 \pm 0.03$ and so $\delta = -0.31 \pm 0.03$.

Other approaches are presented in [38], but an exhaustive theory able to provide a scaling law for the droplet volume and lenght over the entire range covered by the capillary number in the squeezing regime seems to lack still now.

Anyway, in the last section of this chapter the computed lenghts of the droplets as functions of $\phi = \frac{Q_c}{Q_d} = 1/\varphi$ will be presented and we will see a more general trend for them.

1.1.3 Microchannel realization in Lithium Niobate

Althought microfluidics was born in silicon, nowadays the most employed materials for the realization of the channels are polymers, like PDMS and PMMA.[38] Anyway, lithium niobate could be a valid alternative to these materials for the realization of devices able to produce, manipuled and analyze droplets. However, in literature, the only attempts to engrave microfluidics channels on lithium niobate were presented in the last years by our colleagues at the University of France-Comté, Besançon (France), and by Bettella in his work. [38, 44, 50]. The best results were obtained by adaptation of common process used in microelectronics for silicon, such as chemical etching and micromachining, and in optics for glass, such as femtosecond laser damaging. Possible solutions are [38, 51]:

- **Chemical Etching:** it is usually used for ridge waveguides on LiNbO_3 [52], thank to its chemical stability. Process consists in a bath of hydrofluric acid solution (HF), which etches the surface of sample with rate between 1 and $0.06 \mu\text{m h}^{-1}$ depending on crystal cut. This rate makes this technique too slow to have application, even if optical quality is reached.
- **Reactive Ion Etching:** it consists in etching of samples with plasma of reactive ions. In case of LiNbO_3 plasmas successfully used are SF_6 , CF_4 and CHF_3 . Results reported in [53] are rate up to 50 nm min^{-1} . Same similar technique are used in [54] with Inductive Coupled Plasma at rate of 190 nm min^{-1} . Micrometer structures with optical quality are achievable with these rates waiting hours, but specific facilities are needed.
- **Focused Beam lithography:** the sample is etched with focused ion beam. Heavy ions are usually used in this technique differently from electron beam in order to have more resolution (heavier particles have higher momentum, less wavelength so less diffraction). Typical roughens of surfaces are at submicrometre length scales [55]. Although this quality etching rate around 10 nm makes this technique more appropriate for Nanofluidic approaches.
- **Laser Ablation:** it is the process of removing material from a surface by irradiating it with laser beam. it is popular for fabrication of optical waveguides [56, 57]. Possibility to design almost any 2D pattern make it perfect not only for optical waveguided circuits, but also Microfluidic ones. Furthermore engraving depth can finely controlled, and it is an already widely used technique in lithium niobate for different purposes (from index changing to waveguides

design). Some tests of $200 \times 100 \mu\text{m}$ channels with this technique have been realized [50]. However this technique requires specific facilities and bottom surface of channels present stripes in correspondence to laser scan.

- **Mechanical Micromachining:** it is not a specific technique, but series of them. In general a micromachining process use mechanical techniques to manipulate material at scale of micrometer. Most interesting for Microfluidic structure building are micro-mechanical drilling and milling. Recent improvements in micromachining technology allow some astonishing test of fabrication on lithium niobate like [58] and [59].

1.1.4 Lithium niobate wettability

For microfluidic applications, one of the most important property of a material is the wettability, i.e. the interaction between the fluids and the surface of the material. It is the result of microscopic interactions between the molecules of the surface and of the fluid and it usually depends on the chemical composition and the physical morphology of the surface, as well as on the chemical and physical properties of the fluid (namely: surface tension, molecules polarization and polarizability).

It is defined *static contact angle CA*, the angle between the solid surface and the liquid-air interface of a small droplet of the liquid deposited on the surface. Furthermore, it is defined *wettability coefficient k* the cosine of *CA*, that, according to Young's law (eq 1.11), depends on the interfacial tensions of the liquid-solid (σ_{sl}), solid-air (σ_{sa}) and liquid-air (σ_{al}) interfaces:

$$k = \cos CA = \frac{\sigma_s - \sigma_{sl}}{\sigma_{al}} \quad (1.11)$$

In Figure 1.7 we can see the contact angle *CA*.

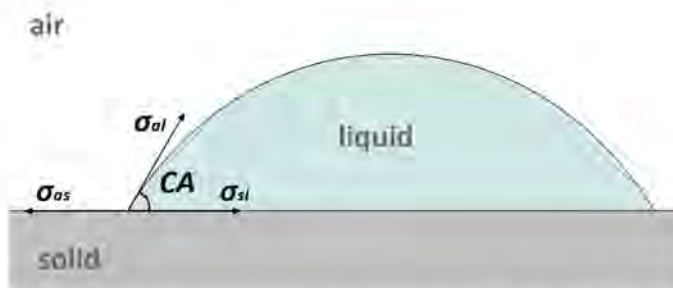


Figure 1.7: **Contact angle CA.** σ_{al} , σ_{sl} and σ_{sa} indicate the surface tensions between air-liquid, solid-liquid and solid-air.

We can employ *k* as an estimation of the wettability of a surface [60]. Higher is the contact angle and lower is the wettability, vice versa lower is the contact angle and higher is the tendency of the fluid to spread and wet the surface.

In droplet microfluidic it is fundamental that the dispersed phase has a high contact angle and, on the contrary, continuous one should completely wet the solid, because, in this case, dispersed phase is never in contact with the solid walls of the channel. In this way, droplets are surrounded by a thin film of continuous phase and

every process inside the microfluidic devide is governed only by the geometry rather than by the wetting properties.

Usually all the hydrocarbons oils have similar wettability properties on the same substrate. Since they interact only with Van der Waals forces the contact angle is very small. On the contrary, water interacts mostly by means of hydrogen bond or polarized bond, so it present lower wettability (high contact angle). For this thesis work hexadecane, an alcane (more information in §1.3) is used as continuous phase, while DI water as the dispersed one.

A detailed study of water and hexadecane wettability properties on lithium niobate had been carried out in [38] and here we report the results. Liquid droplets of 500 nL had deposited on the surface of a crystal of lithium niobate (obtain by commercial double polished wafers from Crystal Technology) and pictures varying all possible setting respect to optical axis of crystal from two perpendicular directions had taken. For every setting more than 10 droplets was measure, average contact angles are reported in Figure 1.8.

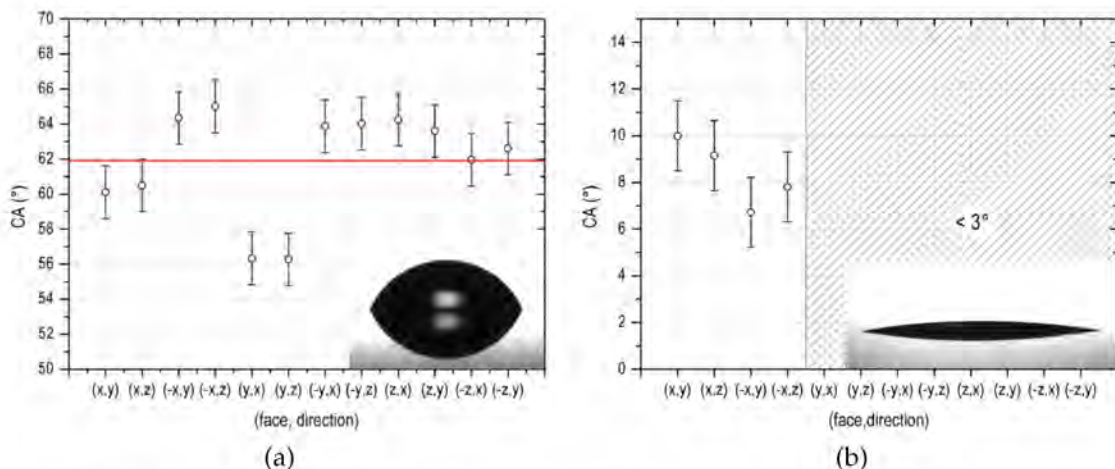


Figure 1.8: **Contact angle (CA) measurements on lithium niobate** [38] for different crystal cuts and crystallographic directions for water (a) and hexadecane (b).

Hexadecane, as expected, wet completely the surface, having a contact angle less than 10° . Instead, a moderate hydrophobicity of lithium niobate has been observed, since a wetting angle of $62^\circ \pm 1^\circ$ has been measured.

Chip sealing

After the microfluidic channel has been engraved on the surface of the crystal, in order to complete the microfluidic device it must be closed. Different solutions had been tested in [38]), but the device used for this work is sealed with an adhesive polymer named Norland Optical Adhesive 68 (NOA68) by Norland Production Incorporation, that is a liquid photopolymer which becomes 100% solid after curing under UV light at 350 ÷ 380 nm.

Channel functionalization

The sealing techniques described in the previous section imply the top wall of the microfluidic channel to be made of a different material rather than lithium niobate. This implies that the wettability properties of the channel are different for the top and the bottom. In fact, in [38], the microfluidic chip with the sealing type described, could not produce water droplet in oil, because the injected fluids entered a co-flow regime (Figure 1.10 (a)). This is due to the too low hydrophobicity and high oleophilicity of lithium niobate respect to that of standard polymers materials (which has a contact angle ranging from 100° to 120° for water and $\sim 35^\circ$ for hexadecane).

The solution found was a functionalization of the microfluidic channel with a procedure extensively described in [38]. The contact angle measurements on functionalized lithium niobate crystall are shown in Figure 1.9. As can be seen contact angles both for water and hexadecane raised: the first reached an average value of $101^\circ \pm 1^\circ$ and the second of $35^\circ \pm 1^\circ$. The wettability of lithium niobate is now perfectly compatible with the one of PDMS [61].

Finally, in Figure 1.10 (b) we can see the images of droplets after the functionalization of the channel.

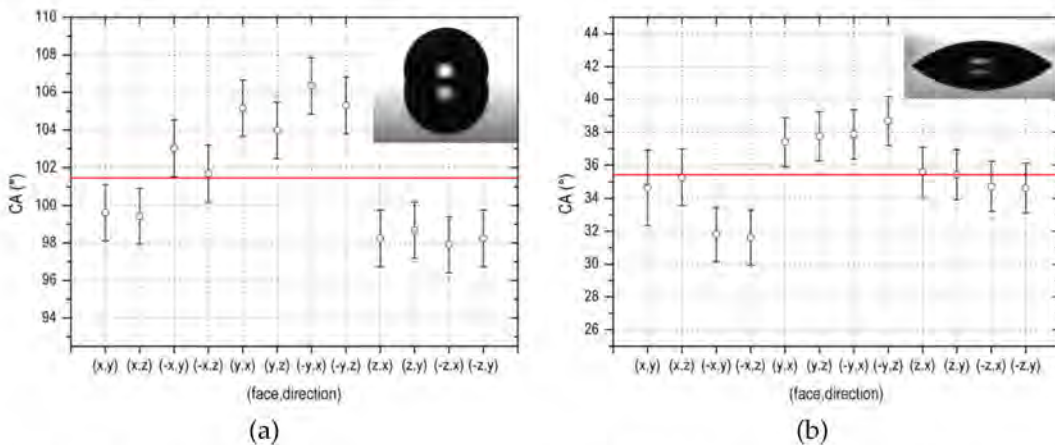


Figure 1.9: **Contact angle (CA) measurements on lithium niobate surface after the functionalization [38]** for different crystal cuts and crystallographic directions for water (a) and hexadecane (b).

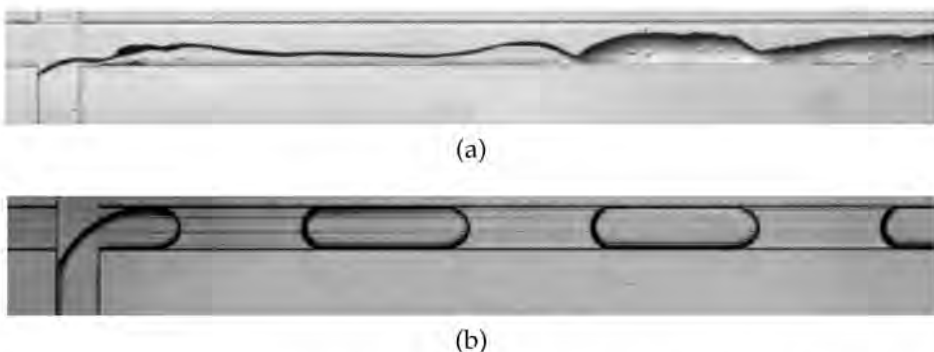


Figure 1.10: **Effect of functionalization on the production of droplets [38]**. In panel (a) the co-flow regime that is established before the functionalization of the channel is showed, in panel (b) on the contrary, we can see the squeezing regime reached after the functionalization.

1.2 Waveguides in Lithium Niobate

For realizing an optomicrofluidic chip completely integrated in lithium niobate, microfluidic channels must be coupled with integrated waveguides. Lithium niobate is one of the most popular materials in the field of integrated optic, it is widely used in photonics industry for the realization of waveguides (but also for electro-optical and acousto-optical modulators and switches, thanks to the piezoelectric, electro-optic and photorefractive properties of the material).

Waveguides are the most important element in every integrated optical circuit and many techniques are available for their fabrication on lithium niobate. In the following a brief list will be provided, because it is beyond the scope of this thesis a further detailed description of waveguide production.

- **Titanium In-diffusion:** is the most popular technique for waveguide realization in LiNbO_3 [62, 63]. Its wide use derives from its simplicity, flexibility and good result in light confinement along both extraordinary and ordinary axes.
- **Proton-exchange:** refractive index change is obtained by immersion of LiNbO_3 in a liquid source of hydrogen ions (usually benzoic acid or toluic acid) at temperature $150 \div 400$ [64]. H^+ substitute ions of lithium in the crystal. Disadvantages are mainly connected to the spoiling of the electrooptic effect and that only modes polarized on extraordinary axis survived.
- **ion-implantation:** consists in the bombardment of crystal with ions and relative implantation there. The net result is a damaged crystal surface with change of refraction index of order of 0.1 [38]. Variety of ions (H, B, C, O, F, Si, P, Ag) at different energies (from 1 MeV up to more than 20 MeV) and fluencies ($10^{12} \div 10^{17}$ ions/ cm^2) have been tested [65, 66, 67]. Change of index strongly depends on material, ion and nuclear interaction [68].
- **Laser writing:** consists in the refractive index change with photorefractive effect and structural modification. Small Δn can be reached (order of 10^{-3}) damaging irreversibly the crystal structure with focused laser beam [69] or with femtosecond pulsed laser. Change in refraction index depend strongly on the energy of the beam [70].

1.2.1 Titanium diffusion

The waveguides of the optofluidic device used in this work were realized via titanium diffusion. Frabication method is accurately described in [38, 51], here we cited only the main steps of the standard procedure:

- A photoresist layer was deposited on the surface of the sample;
- a mask was kept in contact with the photoresist layer while the sample was illuminated with an UV lamp, this imposes the degradation of the unmasked regions;
- a titanium thin film (order of nm) was deposited on the surface by sputtering deposition;

- the photoresist layer was removed in a solvent. This left on the crystal surface only the desired titanium stripes;
- the titanium was diffused into the crystal by high temperature thermal annealing in an oxygen atmosphere ($T=1100^{\circ}\text{C}$, 2 hours).

These steps can be seen in Figure 1.11



Figure 1.11: Main steps for the fabrication of waveguides by titanium in-diffusion.

In general, metal diffusion of dilute system is described starting with the Fick's law:

$$\frac{\partial C(x, t)}{\partial t} = \frac{\partial}{\partial x} \left(D \frac{\partial C(x, t)}{\partial x} \right) \quad (1.12)$$

where $C(x, t)$ is the dopant concentration, while D is diffusion coefficient and, in general

$$D = D(C, T) \quad (1.13)$$

so it can depend on both temperature and concentration.

The dependence on T , it is usually modeled by an exponential law (according to Arrhenius theory):

$$D(T) = D_0 e^{-\frac{E_a}{k_B T}} \quad (1.14)$$

where E_a is the activation energy.

In the case of dilute system $D \sim D(T)$ and the dependence on C can be ignored.

There are, at fixed T , when $D \sim D(T)$, two different types of solutions: one describes the diffusion if the thin film of metal is not completely diffused, while the other one describes the same situation but with exhausted film.

In the first case the film of dopant is approximated to an infinite source and, at the surface of the crystal, the concentration of dopant is constant and equal to the saturation concentration C_s . The solution is an error function:

$$C(x, t) = C_s \operatorname{erfc} \left(\frac{x}{\sqrt{4Dt}} \right) \quad (1.15)$$

In the second case, the solution approximates the thin metal layer with negligible width at $t = 0$, which mean $C(x, t = 0) \neq 0$ only for $x = 0$. With reflection boundary condition, the solution of Fick's Law is a Gaussian profile:

$$C(x, t) = \frac{M}{\sqrt{\pi Dt}} \exp \left(-\frac{x^2}{4Dt} \right) \quad (1.16)$$

where M is the total amount of dopant deposited in the film.

In the case of the waveguides used for this thesis, the general condition to be achieved is that of a completely diffused dopant. Basically, a simple gaussian can be used for fitting the diffusion profile along the direction orthogonal to the surface.

A compositional characterization of the waveguide and the typical concentration profile as a function of depth is reported in Figure 1.12 [38]. As just discussed, the hypothesis of a gaussian shape is satisfied.

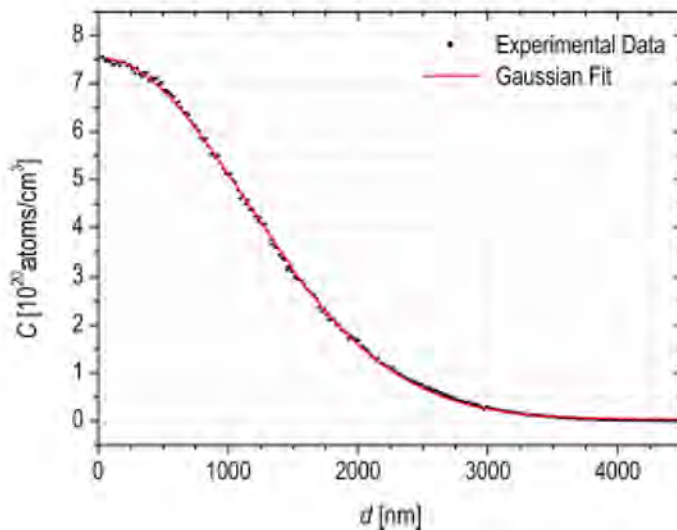


Figure 1.12: **Concentration profile obtained by the SIMS measurement.** Profile of a 37 ± 1 nm titanium film on a x-cut LiNbO₃ substrate after diffusion in O₂ at 1030°C for 2 hours. [38]

1.2.2 Near field (NF) characterization

The near field technique allows to record the light intensity exiting from the waveguide in maps, which corresponding to a 2D image, of its spatial distribution, taken at a given distance from the waveguide output.

In order to measure the near field image of the mode sustained by the waveguides a new experimental setup, sketched in Figure 1.13, was built [38, 51].

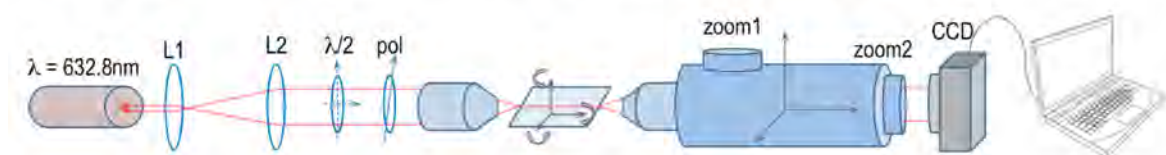


Figure 1.13: **Scheme of the near field setup** [38].

The setup includes [38]:

- a laser source from He–Ne at a wavelength of 632.8 nm with a nominal power of 4mW;
- an half-wave plate and a polarizer to turn and select the polarization of the source in order to exit the TE or TM mode of the waveguide;

- two confocal lens used to increase the laser beam width from 1 mm to 4 mm (the width of the subsequent objective)
- a $20\times$ objective to focus the laser beam;
- a three-dimensional translational and rotational stage to move the sample;
- a microscope in horizontal position endowed with an objective $20\times$ with a working distance of 1.2 cm and two different zoom levels, moved by a three dimensional translational and rotational stage;
- a LaserCam-HR camera by Coherent Inc. to record the near field image.

The reference framework is fixed with the axes oriented in the same directions of the crystallographic directions of the sample with z-propagating waveguides aligned along the laser beam.

The entire procedure of the near field analysis is accurately described in [38]. Here, is important to know only that it allows to record the intensity transmitted by the waveguide. In Figure 1.14 is reported the final image, just to understand the shape of the waveguide (namely, the intensity transmitted) and to see the mode excited.

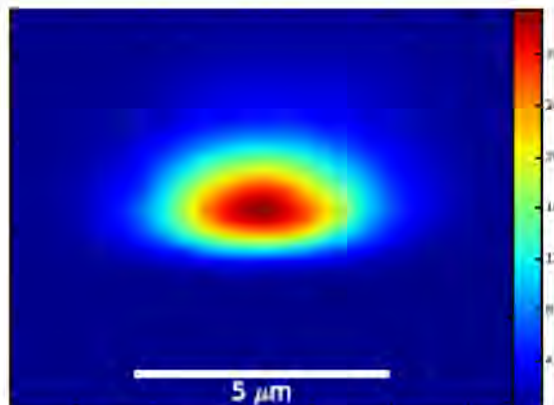


Figure 1.14: Example of the characteristic TE mode (the first one) for a waveguide of nominal width $5\ \mu\text{m}$.

1.3 Device realization

It is beyond the scope of this work providing an accurate description of how is produced the microfluidic chip, but just for information the microchannels for the device of this thesis are realized with a mechanical micromachining with DISCO DAD 321 precision saw. The technique is quite fast and have wide range of possible size for channels, still maintaining good surface quality (for more information see [38, 51]). Dicing have been done thank to collaboration with university of France-Comté, Besançon (France). DISCO DAD 321 mount circular polymeric blades with diamond particles that has a diameter of 56 mm and a thickness of $200\ \mu\text{m}$. In [38] an accurate discussion of the techniques is done and more methods for the production of the microchannel are presented.

In summary, the microfluidic droplet generator used in this thesis is a cross-junction geometry device performed with the dicing saw described and sealed with NOA68. The width of the channels was set to 200 μm and the nominal depth was 100 μm . The other measures are reported in Figure 1.15.

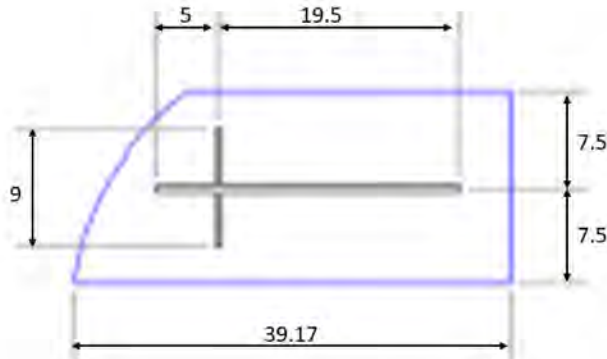


Figure 1.15: **Scheme of the microfluidic device.** Quotes are expressed in millimeters.

We have described the process to build all the elements for an integrated optofluidic device in a single chip made of lithium niobate. In the final sample, z-propagating optical waveguides were realized with the process described in the section below (and the light transmitted by them was recorded with the near field setup). A single microfluidic channel was engraved on the surface perpendicularly to the waveguide, dividing it into two facing parts: one injecting the light signal and the other one collecting the output.

A photo of the microfluidic chip used for the measure in this thesis (that resemble the scheme of Figure 1.15) is reporte in Figure 1.16 (a). In the panel (b) the chip and the cross-junction are highlighted, while the waveguides (one order of magnitude smaller than the channel) are normal to the channel and not visible.

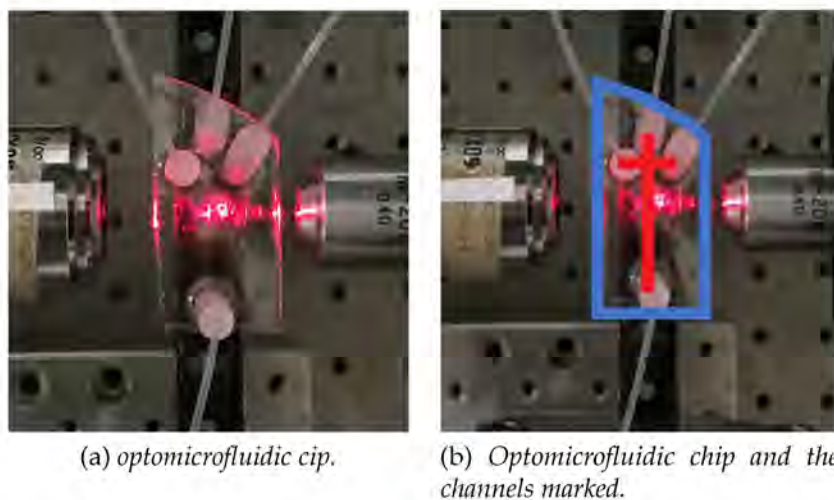


Figure 1.16: **Optofluidic chip in Lithium Niobate**, while is illuminated by the laser light and with the tubes attached at the beginning of the microchannels. In the panel (b) the microfluidic chip is highlighted in blue and the microfluidic channels in red. Obviously the lines do not represent the correct scale.

The key parameter to be studied in this opto-fluidic system is the light transmitted across the microfluidic channel. As can be seen in Figure 1.17, even in the case of the open channel in air, the single mode of the output waveguide was visible at the near field image collected at the surface of the crystal.

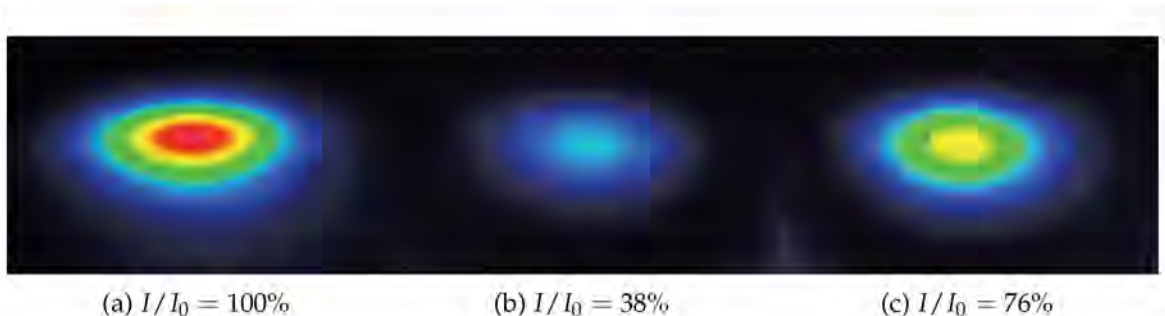


Figure 1.17: Near field images of a waveguide (nominal width $5 \mu\text{m}$) coupled to a $200 \mu\text{m}$ wide microfluidic channel. [38] In (a) TE single mode before the channel was engraved; (b) after the channel was engraved and filled with air; (c) after the channel was filled with hexadecane.

The waveguides realized by titanium in-diffusion in lithium niobate are suitable for optofluidic applications and the signal loss across the microfluidic channel is quite low considering that the channel has a width of $200 \mu\text{m}$, much larger than the waveguide dimensions [38].

1.3.1 Experimental apparatus and droplet detection

In order to be able to perform time resolved measurements of fluid samples flowing along the microfluidic channel after sealing, it was mandatory to modify the acquisition system. The CCD camera was replaced by a simple photodiode, since the aim is now to measure the overall intensity exiting from the output waveguide. A transimpedance was put in series to the photodiode in order to amplify the photo-generated current and convert the signal into a voltage which has been monitored with an Aligent MSO-X 2012A oscilloscope. Moreover a system of ELVEFLOW OB1 Mk3 pressure driven pumps coupled with Coriolis based flow sensors, integrated with a PID system, was employed in order to inject the fluids and control their fluxes (with an apposite software, supplied by the same company) inside the microfluidic channels.

Every time a fluid fills the microfluidic channel and its advancing meniscus reached the waveguide, the light output signal measured by the photodiode increase abruptly and got a higher stationary value, as is expected.

After was proved that the system work correctly, the aim was to generate a train of droplet and to record the signal.

The microfluidic device, used as a droplet generator, presented in the section before (characterized by a cross-junction channels geometry) and visible in Figure 1.16, has been used to create droplet both in cros-flowing and flow-focussing configuration. In Figure 1.18 a scheme of the experimental apparatus just described is reported.

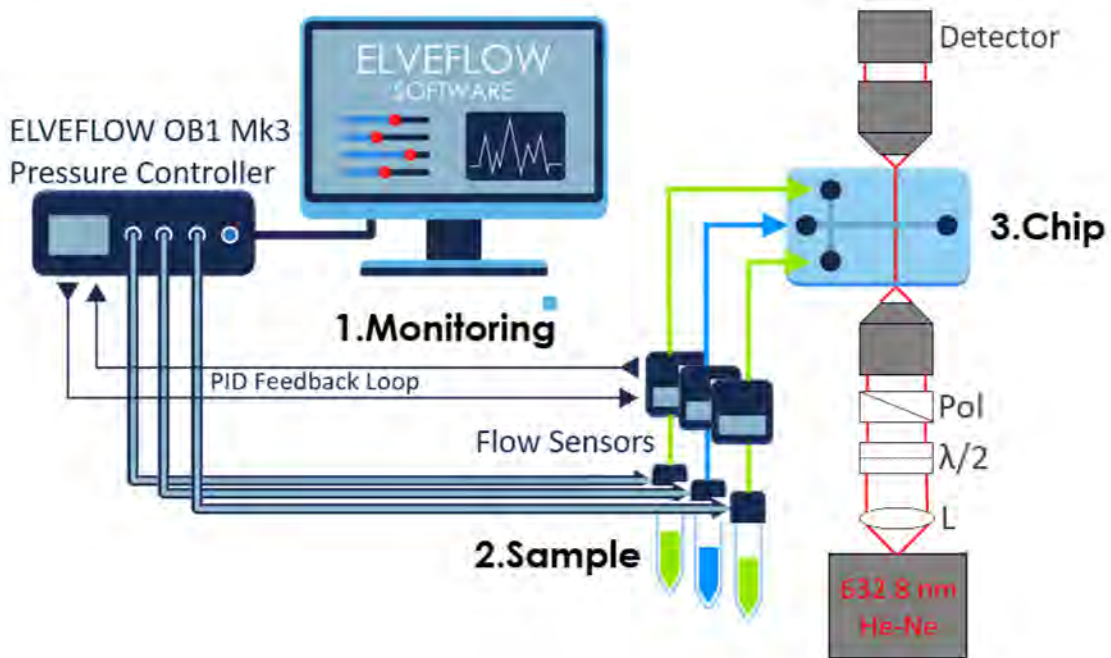


Figure 1.18: Experimental apparatus.

If we want to produce droplets with the cross-flowing configuration, one of the lateral inlets must be sealed in order to exploit the cross-junction as a T-junction. The injected fluids were hexadecane² as the continuous phase and DI water as the dispersed phase. A surfactant (SPAN®80)³, was added to the continuous phase to reduce the interfacial tension between the two fluids. The surfactant concentration was set to 0.08% (w/w) [38]. From now on, to facilitate reading, we refer to the continuous phase simply with the term "oil" and to the dispersed one with "water". The signal, instead of been monitored with the oscilloscope, was collect with an Analog to Digital Fast Card NI 6023E in order to obtain a file of data that can be analysed later. This card can guarantee a measurements sensitivity of voltage reading of 0.0023 mV and maximum sample rate of 200 KS/s.⁴

1.3.2 Data acquisition and analysis

As shown in Figure 1.19, when a train of droplets is generated, the voltage signal recorded by the acquisition system has the shape of a square wave, where the higher plateaus refers to the flow of the continuous phase, while each lower plateau indicates the passage of a water droplet. The peculiarity is that, both the rise and the fall of the square wave are characterized by a sharp peak. These peaks correspond to the passage of the advancing and receding menisci (see Figure 1.20).

²Hexadecane: $\text{CH}_3(\text{CH}_2)_{14}\text{CH}_3$, CAS number: 544-76-3, Mn=226.44 g/mol, viscosity 3cP, density 0.77 g/cm³ @ 25°C.

³SPAN®80: $\text{C}_{24}\text{H}_{44}\text{O}_6$, CAS number: 1338-48-8, Mn: 428.62 g/mol.

⁴For all the measure taken in this thesis, the sample rate has been fixed to 100KHz.

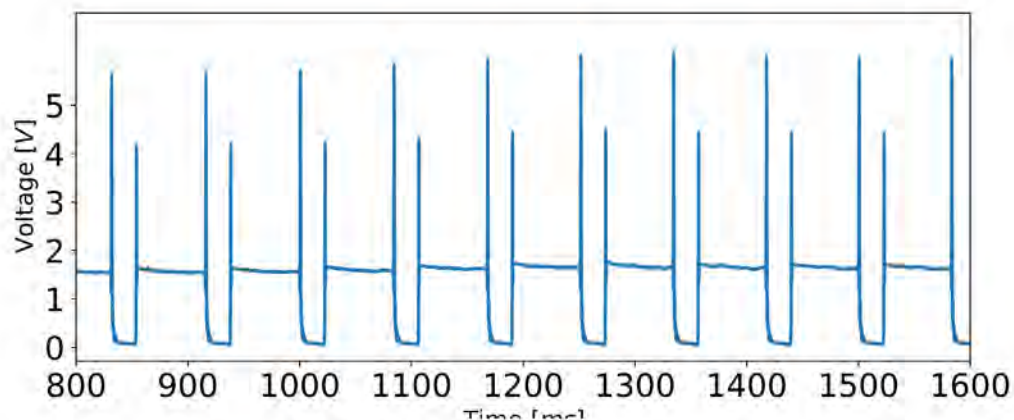


Figure 1.19: Example of the voltage signal from the photodiode at the passage of a train of water droplets in oil. Droplet obtained fixing the fluxes of the continuous and dispersed phase at $Q_c = 30\mu\text{l}/\text{min}$ and $Q_d = 10\mu\text{l}/\text{min}$.

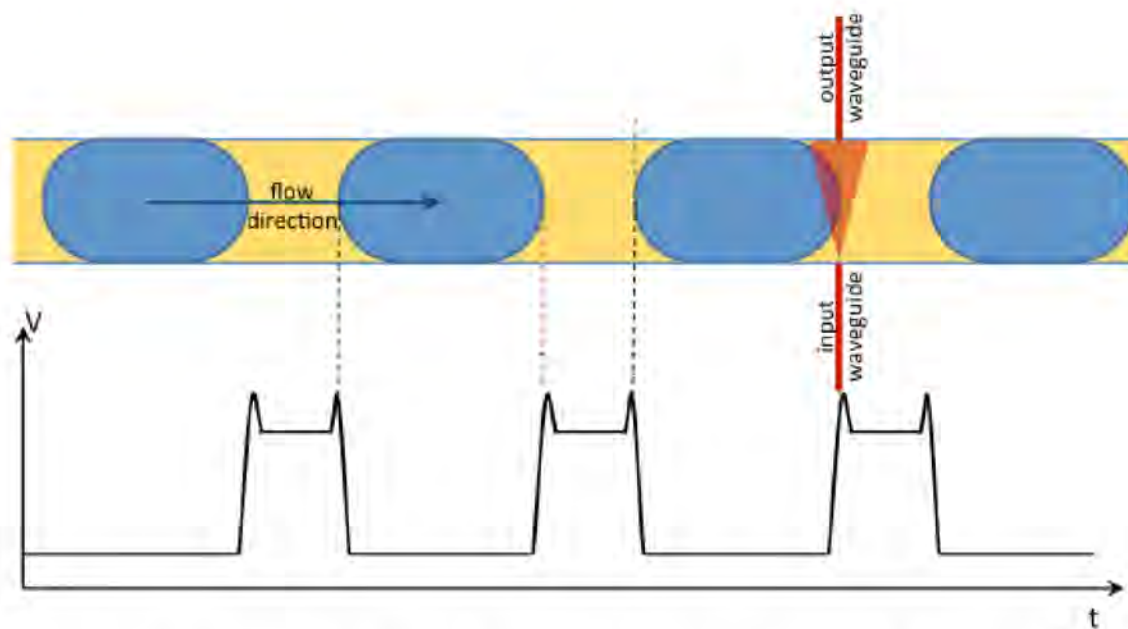


Figure 1.20: Scheme showing the time intervals associated with the droplet passage.

In Figure 1.19 all the droplets have a length that clearly must depend on the speed of the droplets. Equally the speed of the droplet depends on the fluxes of the liquids injected in the channel. The particular case of Figure 1.19 is obtained with $Q_c = 30\mu\text{l}/\text{min}$ (flux of the continuous phase) and $Q_d = 10\mu\text{l}/\text{min}$ (flux of the dispersed phase).

In Figure 1.19 we can see the acquisition profile of nine droplets. With the high sample rate at our disposal, very defined profile of a single droplet can be obtained. Choosing $Q_c = 70\mu\text{l}/\text{min}$ and $Q_d = 10\mu\text{l}/\text{min}$ (so $\phi = 7$) an acquisition file of a train of droplets was taken and in Figure 1.21 the zoom in the region of a droplet let us observe the details of the optical transmission profile. In the same figure a comparison

with other four droplets' profiles randomly selected in the file (containing the signal of 241 droplets) is shown.

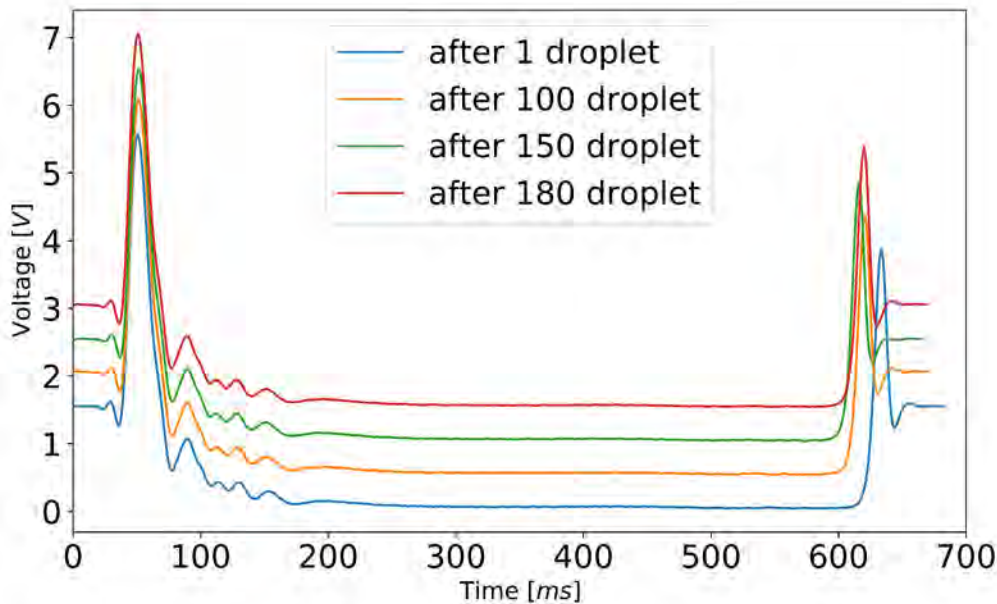


Figure 1.21: **Acquisitions profiles of droplets with $\phi = 7$.** The profiles of the droplets are randomly selected in the file and the plot of each one is traslated along the V-axis, in order to make the graphic more legible.

The profile shows the just cited peaks, but also a more detailed internal structure of the droplets. The aim of this thesis work was exactly to make a complete analysis of the different parts of such a profile. We will return on this point in the next chapters.

1.4 Experimental results

In this thesis the measures were done with the same protocol. For every acquisition we controlled the fluids' flux and operate in the squeezing regime (namely, the generated droplet fills entirely the channel).

Since the length and the velocity of the droplets are proportional to the ratio of the liquids' fluxes flowing in the microfluidic channel, every acquisition profiles was taken fixing $Q_d = 10\mu l/min$, and varying the values of Q_c from $30\mu l/min$ to $400\mu l/min$. In addition droplets were produced both in cross-flowing and flow-focussing configuration, since the optofluidic devide allows for the realization of each one. The data taken were subsequently analysed with a software specifically written for the computing of droplet's length.

In order to have a comparison between the optofluidic acquisitions (the profile in Figure 1.21) and the real shape of the droplet, microscope images (at the same fluids' fluxes just cited) were taken. The acquisition setup is sketched in Figure 1.22

The microscope employed was an inverted microscope Eclipse Ti-E, Nikon with a plan $4\times/0.10$ objective with a 30 mm working distance. The image sequences

was recorded using a fast camera Phantom VRI v7.3. The analysis of the images, presented below together with the optofluidic one, has been performed with an ad-hoc software developed by Enrico Chiarello, in the framework of LaFSI group at the department of Physics of the University of Padova.



Figure 1.22: Sketch of the experimental setup employed for the collection of the images.

With the measures taken we are able to make an accurate analysis over a wide range of ϕ . In this section the aim is to study the lenght of the droplets, but in chapter 3 a complete analysis of the evolution of the shape as function of the fluxes will be made.

The acquisition files for the different values of ϕ were analysed with a Python software specifically written. The code found the peaks and computes the temporal distance between them, in order to obtain a time-lenght of the every droplet in the file. All the measures obtained were represented in an histogram (an example in Figure 1.23). The mean values was considered as the real value of droplets length and, as uncertainty, the standard deviation was choosen.

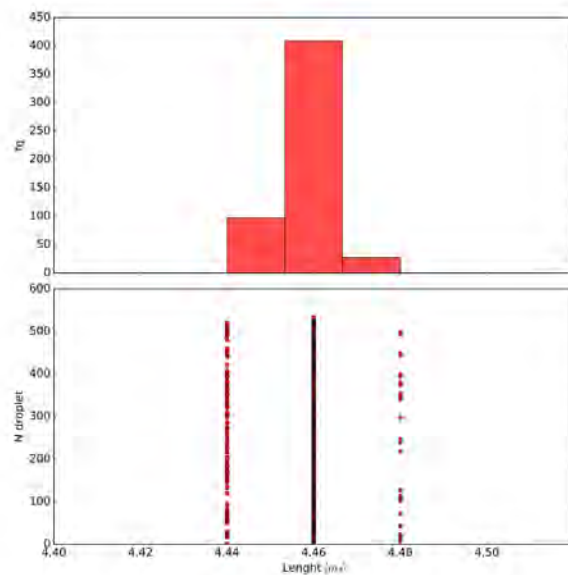


Figure 1.23: Example of hystogram of the lengths of the droplets in a single acquisition file. Acquisition taken with $Q_{oil} = 100 \mu\text{l}/\text{min}$ and $Q_{water} = 10 \mu\text{l}/\text{min}$.

The microscope images were analysed with another ad-hoc code, just cited above.

The software computes the length (in μm) and the velocity (in cm/s) of all the droplet in the image sequence and provides an histogram of them, as can be seen in Figure 1.25. As in the optofluidic acquisitions, the mean value and standard deviation are computed. In order to make a comparison with the optofluidic results, the values obtained in μm had also converted in ms (simply using the relative velocity).

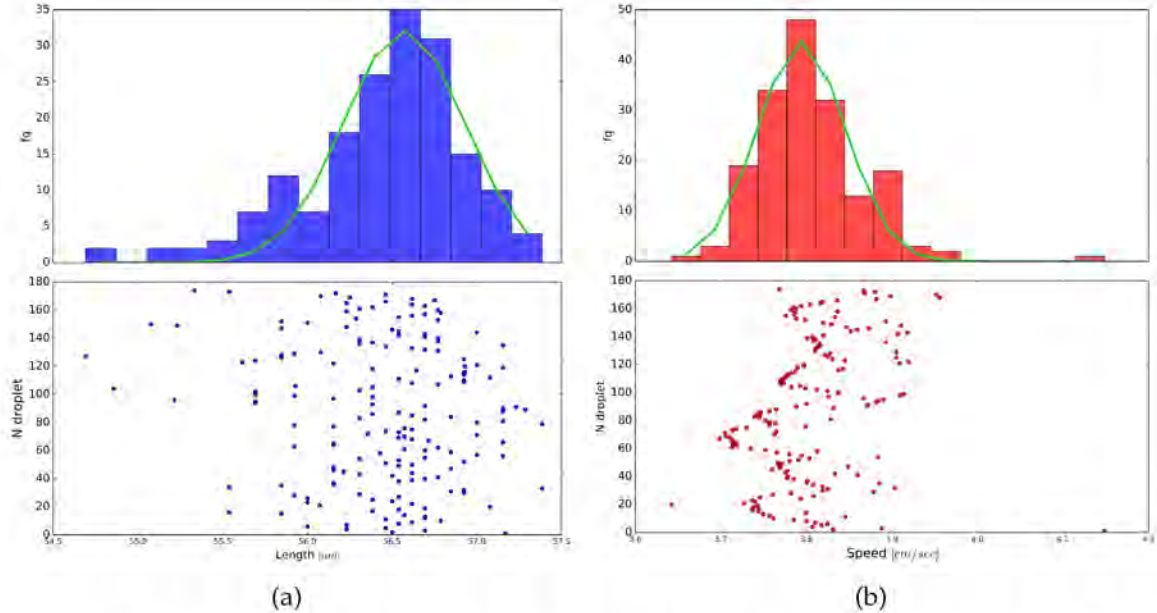


Figure 1.24: **Example of histograms of lengths and velocity of the droplets in an image sequence.** Acquisition taken with $Q_{\text{oil}} = 100 \mu\text{l/min}$ and $Q_{\text{water}} = 10 \mu\text{l/min}$.

The data analysis was made for different values of the flux ratio ϕ both in cross-flowing and flow-focussing configuration⁵. The experimental value of flux ϕ_{exp} , for both continuous and dispersed phase, was computed with the data collected by the flow sensors, that allows the recording of pressure and flux values with a sample rate of 20 Hz, for the entire acquisition time. Finally, ϕ_{exp} was computed as the mean value of the recorded data with the mean error calculated from the standard deviation as uncertainty. The results obtained are reported below.

Analysis in the cross-flowing configuration

It is important to remember that two different acquisitions were performed. The first with the optofluidic apparatus, the other one with the microscope. In the tables below (1.1 and 1.2) all the measures (with relative error) are listed, i.e. the lengths computed with the optofluidic system (L_{opto} , in ms) and with the microscope (L_{micro} , both in μm and ms) and the velocities obtained from the microscope acquisitions.

⁵In all the acquisitions we set $Q_{\text{water}} = 10 \mu\text{l/min}$, so the value of Q_{oil} is straightforward. In flow-focussing every channel inject a half of the entire Q_{oil} .

ϕ_{theo}	ϕ_{exp}	$\sigma_{\phi_{exp}}$	$L_{opto}(\text{ms})$	$\sigma_{L_{opto}}(\text{ms})$
3	3.001	0.008	19.81	0.08
5	4.99	0.01	8.81	0.06
6	6.00	0.02	7.30	0.03
7	7.00	0.02	5.70	0.09
8	8.00	0.02	4.42	0.02
9	9.00	0.03	3.92	0.03
10	10.00	0.03	3.27	0.02
12	12.01	0.03	2.17	0.02
14	14.00	0.04	1.70	0.02
16	16.00	0.05	1.40	0.02
18	18.01	0.05	1.11	0.02
20	19.94	0.06	0.81	0.02

Table 1.1: The values of the length $L_{opto}(\text{ms})$ for every flux, with the relative error, for the cross-focussing configuration. Measures taken with the optofluidic system.

ϕ_{theo}	ϕ_{exp}	$\sigma_{\phi_{exp}}$	$L_{micro}(\mu\text{m})$	$\sigma_{L_{micro}}(\mu\text{m})$	$v(\text{cm/s})$	$\sigma_v(\text{cm/s})$	$L_{micro}(\text{ms})$	$\sigma_{L_{micro}}(\text{ms})$
3	3.001	0.008	665	12	3.9	0.2	17	1
4	4.01	0.08	557	8	4.5	0.1	12	1
5	4.99	0.01	490	10	5.4	0.1	9	1
6	6.00	0.02	449	8	6.2	0.1	7.2	0.4
7	7.00	0.02	421	6	7.2	0.2	5.8	0.3
8	8.00	0.02	398	5	8.1	0.2	4.9	0.2
9	9.00	0.03	370	6	9.0	0.2	4.1	0.2
10	10.00	0.03	357	5	9.7	0.2	3.7	0.2
12	12.01	0.03	328	5	11.5	0.3	2.9	0.2
14	14.00	0.04	311	5	13.8	0.4	2.3	0.1
16	16.00	0.05	288	6	15.0	0.3	1.9	0.1
18	18.01	0.05	272	5	16.7	0.3	1.6	0.1
20	19.94	0.06	259	5	18.8	0.4	1.4	0.1

Table 1.2: The values of the length L_{micro} (both in μm and ms) and the velocity v for every flux, with the relative error, for the cross-focussing configuration. Measures taken with the microscope.

In Figure 1.25 are plotted the length in μm (a) and the velocities (b) (acquisition with the microscope) as function of ϕ . Under the figure, in Table 1.3, the results of power and linear interpolations (respectively for $L_{micro}(\mu\text{m})$ and v) are reported.

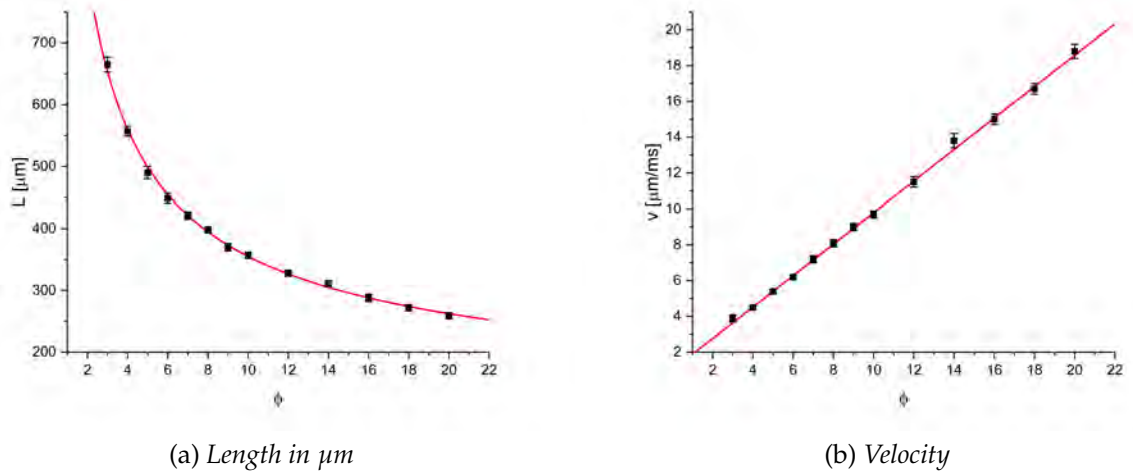


Figure 1.25: **Length and velocity of the droplets.** Measures taken with the microscope. In (a) are shown the lengths with a power interpolation (red curve), while in (b) the velocities, with a linear interpolation (red curve).

$L = A\phi^C + B$			$v = v_0 + m\phi$	
$A(\mu\text{m})$	$B(\mu\text{m})$	C	$v_0(\text{cm/s})$	$m(\text{cm/s})$
1120 ± 29	93 ± 22	-0.63 ± 0.05	1.01 ± 0.07	0.879 ± 0.009

Table 1.3: The values of A , B and C from the power interpolation of $L_{micro}(\mu\text{m})$ and v_0 , m from the linear interpolation of v .

$L_{opto}(\text{ms})$ and $L_{micro}(\text{ms})$ are plotted in Figure 1.26. The points were fitted with a power law $L = A\phi^C + B$ and the results of the interpolations are shown in the Table 1.4 under the graphics.

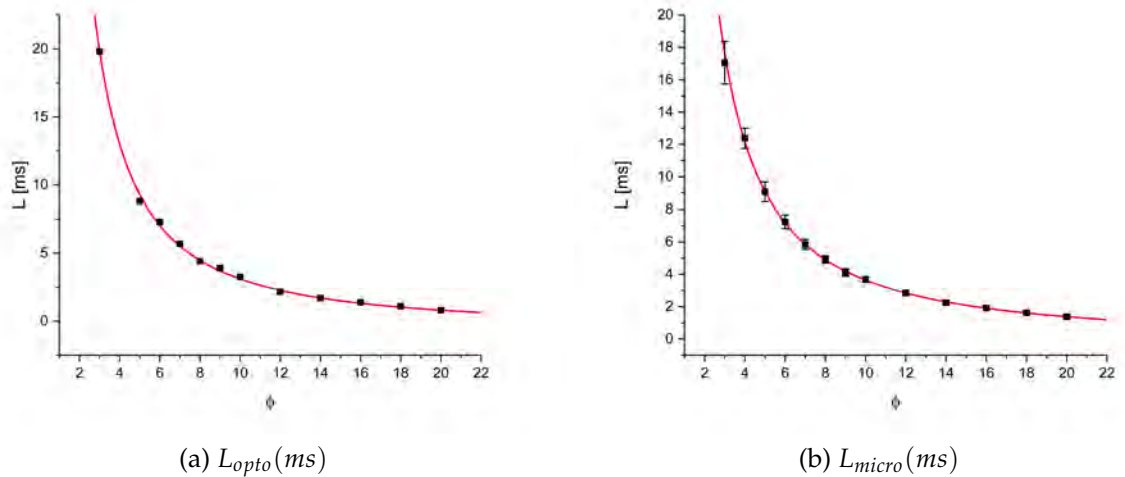


Figure 1.26: **Plotted values of $L_{opto}(\text{ms})$ and $L_{micro}(\text{ms})$ as function of the ϕ .** $L_{opto}(\text{ms})$ (a) and $L_{micro}(\text{ms})$ (b) interpolated with a power law (red curves).

	$A(\text{ms})$	$B(\text{ms})$	C
Optofluic	98 ± 7	-0.5 ± 0.1	-1.43 ± 0.05
Microscope	72 ± 2	-0.22 ± 0.07	-1.27 ± 0.02
Compatibility	3.6	2.3	55.2

Table 1.4: The values of A , B and C from the power interpolation of both $L_{\text{opto}}(\text{ms})$ and $L_{\text{micro}}(\text{ms})$, with the relative compatibility.

As we can see the compatibility is not so good, but we have to say that the two methods are completely different. On the contrary, considering the enormous diversity, the results is excellent. In fact, both cases shows a well defined power trend of the length as a function of ϕ . The reduced χ^2 values (51 for optofluidic and 0.07 for microscope) are not reliable, in fact the error on the optofluidic measurse is too small. From §1.1.2 we remember Christopher *et al.* [48] demonstrate that $L \propto \frac{1}{\phi}$. Basically, the resulting curve should be an hyperbole and this means that the computed value of C (the exponent in the power law interpolation) it was supposed to be compatible with $C_{\text{Christopher}} = -1$. This does not happen, neither for the optofluidic method nor for the microscope acquisition, exhibiting a compatibility (with -1) of 47 and 114 respectively.

Analysis in the flow-flowing configuration

The same kind of analysis was performed also for droplets generated in flow-focussing configuration. As just done before, we report below all the measures, with relative errors (Tables 1.5 and 1.6), acquired with the both optofluidic method and microscope.

ϕ_{theo}	ϕ_{exp}	$\sigma_{\phi_{\text{exp}}}$	$L_{\text{opto}}(\text{ms})$	$\sigma_{L_{\text{opto}}}(\text{ms})$
6	6.01	0.01	3.94	0.02
8	8.00	0.02	2.62	0.02
10	10.01	0.02	2.004	0.02
12	12.00	0.02	1.55	0.03
14	14.01	0.03	1.24	0.02
16	16.03	0.03	1.00	0.02
18	18.01	0.04	0.83	0.02
20	20.04	0.04	0.71	0.03
22	22.04	0.04	0.605	0.02

Table 1.5: The values of the length $L_{\text{opto}}(\text{ms})$ for every flux, with the relative error, for the flow-focussing configuration. Measures taken with the optofluidic system.

ϕ_{theo}	ϕ_{exp}	$\sigma_{\phi_{exp}}$	$L_{micro}(\mu\text{m})$	$\sigma_{L_{micro}}(\mu\text{m})$	$v(\text{cm/s})$	$\sigma_v(\text{cm/s})$	$L_{micro}(\text{ms})$	$\sigma_{L_{micro}}(\text{ms})$
4	4.01	0.08	417	9	4.33	0.09	10	1
6	6.01	0.01	340	4	6.12	0.09	5.6	0.2
8	8.00	0.02	300	4	7.9	0.2	3.8	0.2
10	10.01	0.02	277	2	9.5	0.1	2.9	0.1
12	12.00	0.02	259	2	11.5	0.1	2.3	0.1
14	14.01	0.03	252	3	13.2	0.2	1.9	0.1
16	16.03	0.03	240	2	15.3	0.2	1.57	0.05
18	18.01	0.04	230	3	17.1	0.2	1.3	0.1
20	20.04	0.04	223	2	19.2	0.4	1.16	0.04

Table 1.6: The values of the length L_{micro} (both in μm and ms) and the velocity v for every flux, with the relative error, for the flow-focussing configuration. Measures taken with the microscope.

With the same scheme as before, in Figure 1.27 are plotted the length in μm (a) and the velocities (b) (acquisition with the microscope) as function of ϕ . In Table 1.7 the results of the power and linear interpolation are reported.

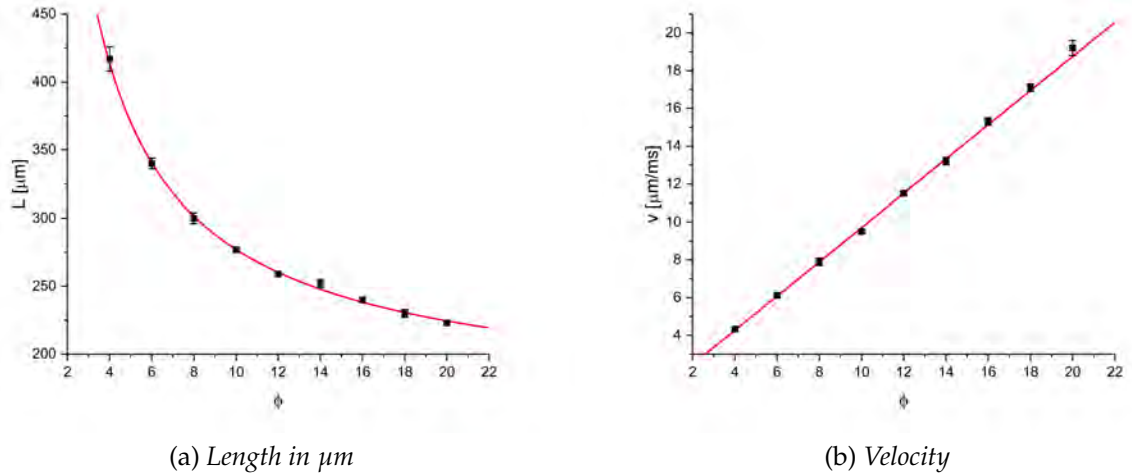


Figure 1.27: **Length and velocity of the droplets.** Measures taken with the microscope. In (a) are shown the lengths with a power interpolation (red curve), while in (b) the velocities, with a linear interpolation (red curve).

$L = A\phi^C + B$			$v = v_0 + m\phi$	
$A(\mu\text{m})$	$B(\mu\text{m})$	C	$v_0(\text{cm/s})$	$m(\text{cm/s})$
810 ± 71	157 ± 11	-0.83 ± 0.08	0.6 ± 0.1	0.91 ± 0.01

Table 1.7: The values of A , B and C from the power interpolation of $L_{micro}(\mu\text{m})$ and v_0 , m from the linear interpolation of v .

$L_{opto}(\text{ms})$ and $L_{micro}(\text{ms})$ are plotted in Figure 1.28. The points were fitted with a power law $L = A\phi^C + B$ and the results of the interpolations are shown in the Table 1.8 under the graphics.

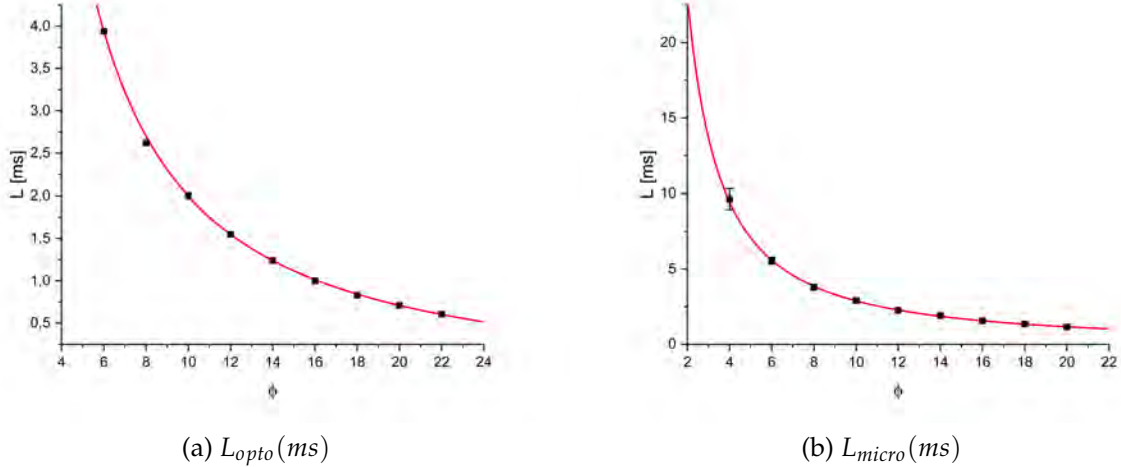


Figure 1.28: Plotted values of $L_{opto}(\text{ms})$ and $L_{micro}(\text{ms})$ as function of the ϕ . $L_{opto}(\text{ms})$ (a) and $L_{micro}(\text{ms})$ (b) interpolated with a power law (red curves).

	$A(\text{ms})$	$B(\text{ms})$	C
Optofluic	37 ± 1	-0.27 ± 0.03	-1.21 ± 0.02
Microscope	56 ± 4	-0.03 ± 0.08	-1.28 ± 0.04
Compatibility	4.6	2.8	1.6

Table 1.8: The values of A , B and C from the power interpolation of both $L_{opto}(\text{ms})$ and $L_{micro}(\text{ms})$, with the relative compatibility.

As we can see, also with the flow-focussing configuration the two methods show a well defined power trend, with the addition of the fact that the results are also compatible. In this configuration the reduced χ^2 values are 3.0 and 0.2 respectively for optofluidic and microscope acquisitions, so the power interpolation reproduce well the experimental data.

No scaling relation of the length as function of ϕ is reported in literature (except for [71]) for the flow-focussing configuration (the theoretical scaling derived from Christopher *et al.* is valid only for the cross-flowing) and we can confirm a power trend.

A demonstration that the experiment is well done, is the measure of the velocities. In fact, at a fixed values of ϕ the quantity of fluid injected in the microchannel is the same and we expect that the droplet velocity is the same independently from the configuration. In other word the trend should be the same both for cross-flowing and flow-focussing configuration. This is exactly what happens as we can notice in Table 1.9

	v_0 (cm/s)	m (cm/s)
Cross-flowing	1.01 ± 0.07	0.879 ± 0.009
Flow-focussing	0.6 ± 0.1	0.91 ± 0.01
Compatibility	3.4	2.31

Table 1.9: The values of v_0 and m from the linear interpolation of the velocity measures for both cross-flowing and flow-focussing configurations.

In the end, we have shown that the optofluidic system described in this chapter, is a good tool for the analysis of droplet flowing in a microchannel. In fact, the classic analysis using microscopes, image recording and post-processing need a continuous calibration of the acquisition parameters that can not be pre-selected (moreover, fast CCD cameras are very expansive). Instead, with the optofluidic method the analysis is automated, since the acquisition rate depends only on detector (photodiode) and electronics.

In the rest of the thesis we will demonstrate that the optofluidic method allows us to recognize details of the droplet shape that are impossible to see with the naked eye.

Chapter 2

Droplet simulation

The optical transmission profile detected by the optomicrofluidic circuit presented reproducible fingerprints, each droplet showing the same waveform of the signal in every macroscopic variation. This suggested that such characteristic waveform contains lots of physical information, from the properties of the flow (droplet shape, angle of contact, etc...) to physical properties of the two phases. Indeed the interpretation of such waveform results not so straightforward.

Interaction between two complex systems such as waveguided light and microfluidic droplet makes this system rich of physical phenomena to be investigated. To understand them, a code that simulates the interaction at the droplet surface, and inside it, was written to compute the light transmission across the droplet and the relative effects of optical transmission.

2.1 The simulation software

The simulation software was built considering the microfluidic channel of defined geometry with a cartesian three dimensional system as in Figure 2.1, with the x and y coordinates representing depth and height and the z coordinate indicating the flowing direction. In this system the waveguide is directed in the x direction and its section on the surface of the channel can be seen in the figure below (the blue rectangles).

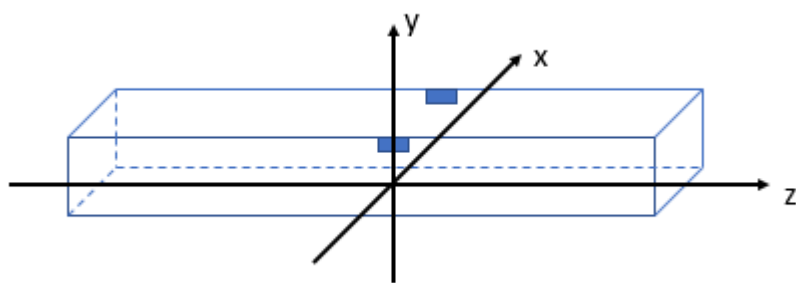


Figure 2.1: **Representation of the microfluidic channel with the axis chosen for the simulation:** the little blu rectangles represent the waveguide. Figure not in scale.

In order to simulate the transmittivity, it is necessary to estimate the ratio between the intensity of transmitted and incident light through a medium with refractive index $n(\lambda, T)$ (where, λ is the wavelength and T the temperature). In the present case, a droplet (with refractive index $n_{droplet}$) passes through the microfluidic channel, eclipsing the light source (the waveguide). Formally, the method is equivalent to simulate the transmittivity of a medium with refractive index $n(t)$ (with t the passage time) and an exposed interface $S(t)$, where S indicate its shape. So, the problem, basically, consists on a ray-tracing through a medium with a dynamically variable shape.

Since the aim is to understand the physical meaning of the peaks of intensity in the acquisition profile, the exposed interface is essentially the meniscus of the droplet. To quantify the role of this meniscus a geometric optic simulation is realized. As said before, the purpose of this simulation is to weight the lens effect of the droplet meniscus. Clearly, for a complete description, Maxwell's equations (using finite element method) should be solved with a specific set of boundary conditions. This is a particularly complicated problem, so, in this thesis, it was simplified adopting the approximation of rays optic.

The mesh for the simulation has to take into account that waveguide's output has typical dimension of few micrometers, but the channel has dimension of hundreds micrometers requiring lots of computational power.

Furthermore the uncertainty of the droplet shape (there are not a definitive description of droplet shape during the flow in literature yet) is the real bottleneck for a complete and correct computational description of the system. So the finite element method should result more expensive and not so clearer than a simple geometric approach. For the same reasons the system is considered with a 2D approximation, in particular the rays move only on the plane orthogonal to the channel wall.

In writing the code, every part of the system has been schematized. After having fixed the channel sides (height in the y direction $h_{ch} = 50\mu\text{m}$ and depth in the x direction $l_{ch} = 80\mu\text{m}$), a model was studied for represent the source.

The waveguide's output, as seen from the near field images in chapter 1, seems to resemble an ellipse and for this reason the code simulates it with an elliptic profile. For doing this, a defined number N_{sou} of punctual source points organized in N_{ell} number of concentric ellipses are simulated. For having a good distribution of the source points in the ellipses, we have $N_{sou} = 10 \cdot N_{ell} + 1$. In this way, every ellipse has exactly 10 source points within it, the last being positioned in the common center of the ellipses.

An example with $N_{ell} = 4$ ellipses and $N_{sou} = 41$ source points is in Figure 2.2.

In the reference frame of Figure 2.1 the source is centered in $(x, y, z) = (0, 48, 0)\mu\text{m}$ with semiaxes (of the major ellipse) of $S_y = 1.8\mu\text{m}$ and $S_z = 2\mu\text{m}$.

As just said, a simple geometrical approach, using ray optic, has been chosen. So, from each source point, were generated a fixed number N_a of optic rays, each one with a different angle respect to the x -axis, from $+N_A$ to $-N_A$, where

$$N_A = \arcsen \left(\frac{\sqrt{n_{NbLiO_3(Ti)}^2 - n_{NbLiO_3}^2}}{n_{hex}} \right) \sim 8.9^\circ \quad (2.1)$$

is the *numerical aperture* [72] and n_{NbLiO_3} is the refraction index of the Lithium Ni-

bate, $n_{NbLiO_3(Ti)}$ the one of sputtered Niobate, n_{hex} the refraction index of the oil (hexadecane).

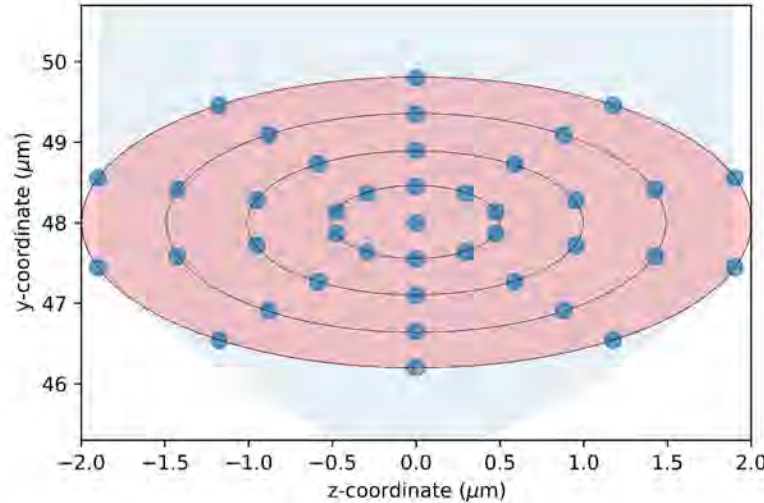


Figure 2.2: **Simulated source:** 4 ellipses with 10 source point for each, plus the isolated central point.

The main difficulty in writing the code was the choice of droplet meniscus shape. Indeed there is no unique, clear and definitive model in literature for droplet shape in microfluidic, still being studied in forms of images recorded by imaging procedures. So, a quite intuitive and simple (from the computational point of view) approach has been used.

The simulation discretizes the time (or similar, the z-axis) in N_t intervals (steps) and at each one correspond a different z-coordinate (during the flow of the meniscus) and so a different droplet profile. The problem is to fix this droplet profile. We have chosen an elliptic one, in the sense that, at each step, in the (x, y) plane, the droplet is an ellipse with definite values of semiaxes. This means that the semiaxes must grow as function of the t-steps.

To define this function, other two parameters has been defined: z_{fin} and $z_{fin_{real}}$. The first one is the z at which the simulation is concluded (namely, is the value of the z coordinate that correspond to the value N_t in the steps). The second one is the z at which the semiaxes of the droplet has the same values of the channel sides (namely, is the value at which the droplet fill completely the channel).

In order to respect this hypothesis, was found that the semiaxes must grow in a particular way, namely:

$$x_{dr}(z) = \frac{l_{ch}}{\sqrt{1 - \left(\frac{z_{fin_{real}} - z_{fin}}{z_{fin}}\right)^2}} \left(1 - \left(\frac{z - z_{fin}}{z_{fin}}\right)^2\right)^k \quad (2.2)$$

$$y_{dr}(z) = \frac{h_{ch}}{\sqrt{1 - \left(\frac{z_{fin_{real}} - z_{fin}}{z_{fin}}\right)^2}} \left(1 - \left(\frac{z - z_{fin}}{z_{fin}}\right)^2\right)^k \quad (2.3)$$

Moreover the choice of z_{fin} let us define a relation between z and t (the steps)

$$z(t) = \frac{tz_{fin}}{N_t} \quad (2.4)$$

k is a free parameter, its natural value should be $k = 1/2$, but varying it one can modify the shape of the droplet. In Figures 2.3 and 2.4 we can see, respectively, the elliptic droplet sections for different values of t and the growth of the semiaxes as function both of t and z .

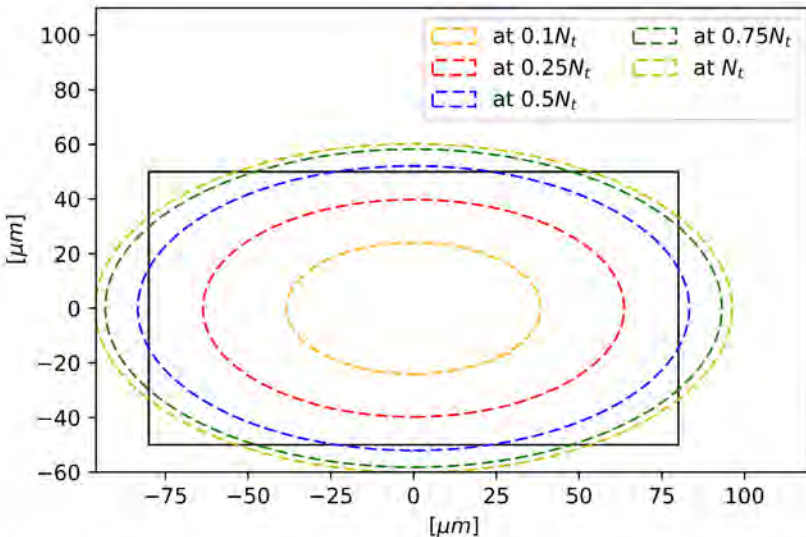


Figure 2.3: **Section of the hypothetical droplet at some fixed step of the simulation.** The black rectangle is the section channel in the (x, y) plane and the dashed ellipses are the section of the droplet (at different values of the t -step) in the (x, y) plane.

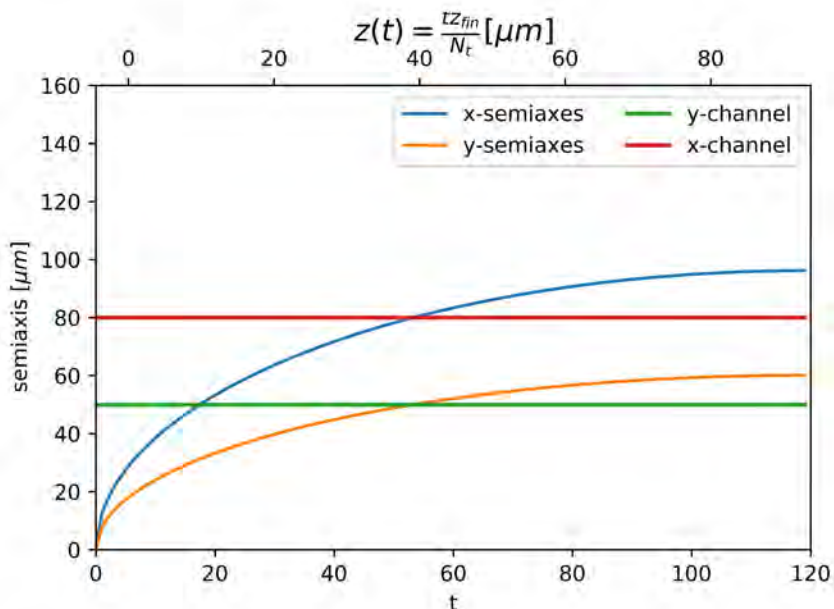


Figure 2.4: **Grown of the semiaxis:** with fixed values of $k = 1/2$, $z_{fin} = 90$, $z_{fin_{real}} = 40$ and $N_t = 120$, 4 ellipses with 41 source points.

We can notice that, for every $z > z_{fin_real}$ the semiaxes are longer than the relative channel's size. Obviously, this has no physical meaning, but is just a way to give a shape to the meniscus. All results in the region beyond z_{fin_real} will not be considered as physical. Anyway, despite this, we will see that the simulation work as expected.

Every ray, based on its emission angle, can have a different behavior.

- A ray can center the guide facing on the other side of the channel without touching the droplet, in this case we call it a *directed ray* (represented in blue in Figure 2.5);
- otherwise, it can enter the droplet and undergoing to refractions. We call *refracted ray* (represented in red in Figure 2.5) every ray that, after leaving the droplet, centers the waveguide.



Figure 2.5: **Refracted and directed rays.** Example of a refracted ray (red one) and a directed ray (blue one). The shape of the droplet is not the correct one, but was chosen for a better comprehension of the rays' role.

The code essentially computes $N_{dir}(t)$ and $N_{ref}(t)$, the directed and refracted rays at each step t (or, similar, at each z) and makes the sum of them in order to obtain the total number of rays $N_{tot}(t) = N_{dir}(t) + N_{ref}(t)$ collected by the waveguide after the interaction.

In Figure 2.6 we can see the result of the simulation, namely the graphic of the collected light intensity, that is estimated as $\frac{N_{tot}}{N_{sou}N_a}(t)$, as a function of t . Moreover, in the same figure, $\frac{N_{dir}}{N_{sou}N_a}(t)$ and $\frac{N_{ref}}{N_{sou}N_a}(t)$ are also shown, i.e. the collected intensity of directed and refracted rays.

It is clear that the plot could be divided in three zones.

- The first is the one where the collected intensity of refracted rays is zero and the one of directed is constant. This is the interval of time in which the meniscus of the droplet is too small to interact in an useful way with the light leaving the waveguide (in the sense that, even if a ray hits the droplet, it exits with an angle that do not permit it to enter the waveguide). When $t \sim 40$ some rays begin to interact efficiently with the droplets and the semiaxes are enough long

to hide a part of the source.

- The second one goes from $t \sim 40$ to $t \sim 60$. Here the number of directed rays fall down and the number of refracted grow. When $N_{dir}(t) = 0$ the droplet has completely filled the channel (so $z = z_{fin_{real}}$), in fact, looking at Figure 2.4 we can see that (with the choosen values for the parameters) $t \sim 55$ corresponds to $z \sim 40$ (the value set up for $z_{fin_{real}}$).
- The last one is for $t > 60$ and is the zone where the simulation has no physical meaning. In fact, it gives a wrong result because we expect, from the experimental data, that the refracted rays goes to zero (we will see this later).

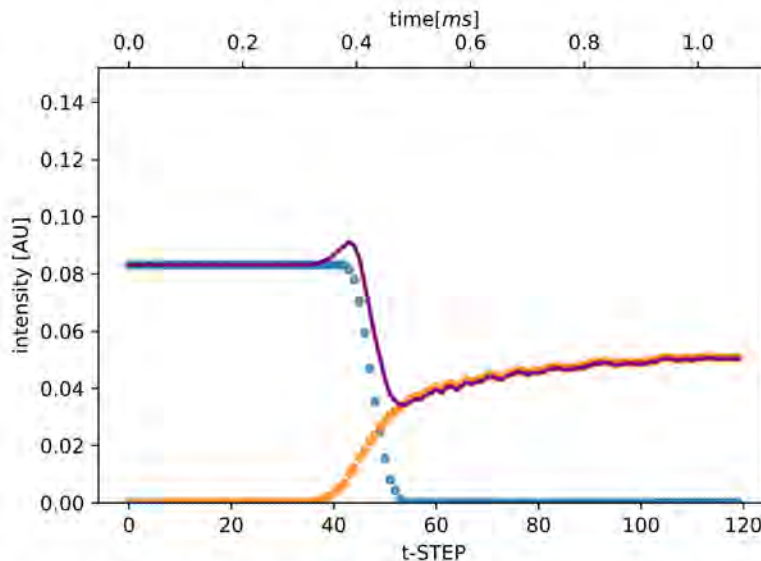


Figure 2.6: Result of the simulation. The blue dots are the number of directed rays, the orange dots, instead, are the number of refracted rays. The sum of them is the green line. The parameters used are: 4 ellipses with 41 source points, $k = 1/2$, $z_{fin} = 90$, $z_{fin_{real}} = 40$ and $N_l = 120$, $N_a = 100$.

In order to better understand it, the software computes the mean angle of all directed and refracted rays, at every step. In Figure 2.7 is shown as function of the t -steps. As we expect that mean angle of directed rays, in the first zone, has a null costant value (due to the fact that the number of rays that go straight to the top is equal to the ones that go straight to the bottom) and for $t \sim 40$ it begins to increase. In fact, in the second zone, a portion of the ray that should go straight to the bottom interact with the droplet. In the third zone there are no more directed rays, and so does not exist a mean angle (so it is set to zero).

For the refracted rays is a bit different (more simple). At the beginning there are no refracted rays, so does not exist a mean angle (set to zero). In the second and in the third zones they begin to increase and their mean angle does the same (the initial value is negative and equal to $-NA$, as we should expect).

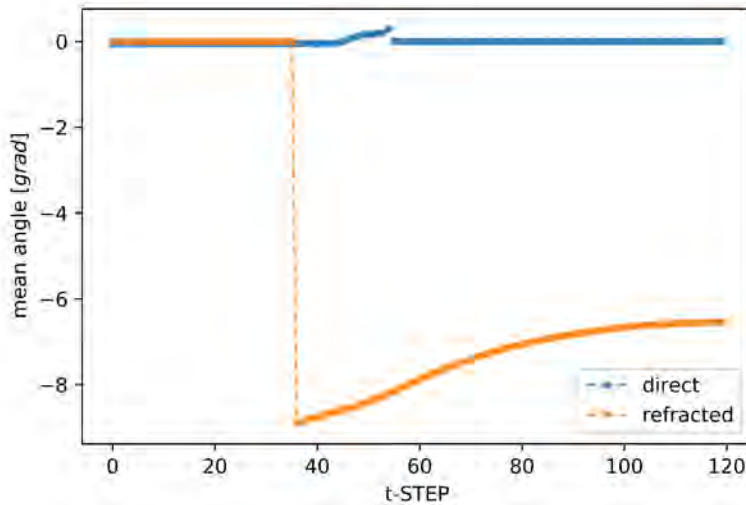


Figure 2.7: Mean angle for directed and refracted rays as function of the t -steps. The parameters used are: 4 ellipses with 41 source points, $k = 1/2$, $z_{fin} = 90$, $z_{fin_real} = 40$ and $N_t = 120$, $N_a = 100$.

2.2 Simulations with interference

As we can note from the result in Figure 2.6, the refraction effect alone does not describe the experimental evidence of a peak in intensity. In order to reproduce this, the code was further implemented and interference between the directed and refracted rays was added. The refracted rays, in fact, due to the longer optical path, suffer from a phase shift with respect the directed one.

In order to compute this shift, the code calculates the mean optical path of every ray, at every step. Using this value of optical path, interference was considered using the standard formula (equation 2.5). This means that, at every t -step, the number of rays entering the waveguide (facing on the other side of the channel) is no more the simple sum of directed and refracted, but:

$$N_{tot}^{int}(t) = N_{dir}(t) + N_{ref}(t) + 2\sqrt{N_{dir}(t)N_{ref}(t)} \cos \left[\frac{2\pi}{\lambda} \left(\frac{OA_{mean}(t)}{N_{dir}(t)} + \frac{OA_{mean}^{ref}(t)}{N_{ref}(t)} \right) \right] \quad (2.5)$$

where $OA_{mean}(t)$ and $OA_{mean}^{ref}(t)$ are, respectively, the optical path of directed and refracted rays at every step and λ is the wavelength of the laser light.

In Figure 2.8 the values of $N_{tot}^{int}(t)$ are shown as function of the t -step. In the same plot is reported also the curve obtained with the simple sum of directed and refracted rays, for comparison.

The contribute of interference introduces intensity fluctuations which entity is significantly greater (about 50%) than the contribute of the directed and refracted beams (just discussed in the previous section). The positions of the peaks are at a relative distance δ close to 5 steps and develop within the transient region corresponding to the meniscus passage.

In order to take into account that the detection of the outcoming rays is carried

out by a photodiode, and it integrates the output, the interference contribute was approximated by a convolution of the maxima with a spline (third degree). The result is presented in Figure 2.9.

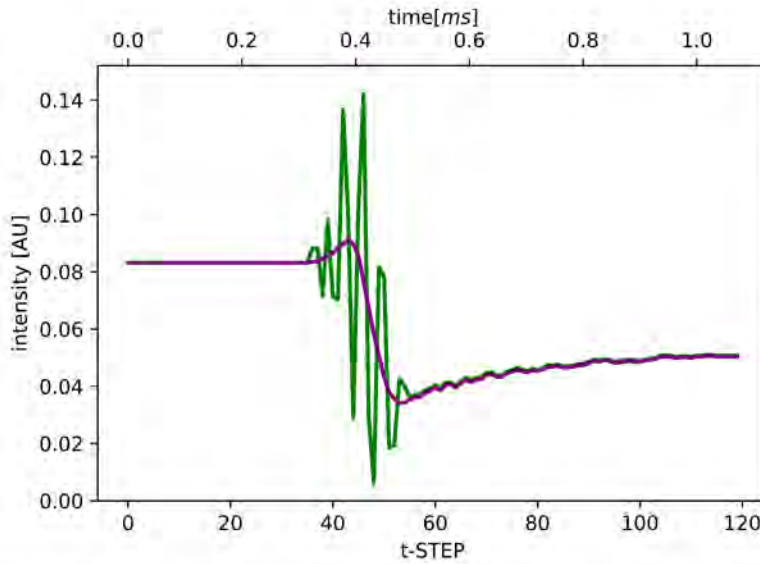


Figure 2.8: Result of the simulation with interference. The green line is the result obtained plotting the N_{tot}^{int} value computed with interference. The purple line is the simple sum of directed and refracted rays (the same in Figure 2.6). The parameters used are: 4 ellipses with 41 source points, $k = 1/2$, $z_{fin} = 90$, $z_{fin_{real}} = 40$ and $N_t = 120$, $N_a = 100$.

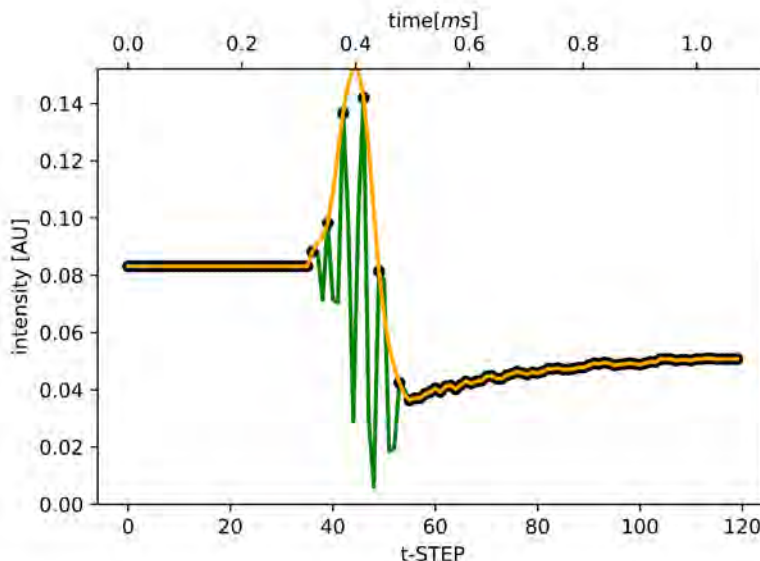


Figure 2.9: The result of the simulation with interference after the "integration". The yellow line is the spline between the maxima of the interference figure. The parameters used are: 4 ellipses with 41 source points, $k = 1/2$, $z_{fin} = 90$, $z_{fin_{real}} = 40$ and $N_t = 120$, $N_a = 100$.

2.3 Comparison with experimental data

Our acquisition system has a sample rate of 100 KHz, namely he takes 10^5 points per second. In order to compare the experimental data with the result of our simulation, we need to relate the t -steps to the "real" time and this can be done if we know the sample rates both of the simulation and the experimental apparatus. So, in the simulation, the parameter $Q = Q_{oil} + Q_{water}$ has been introduced, namely the total flux of fluids in the channel. In this way the sample rate f of the simulation can be evaluated as:

$$f = \frac{N_t Q}{4l_{ch}h_{ch}z_{fin}} \quad (2.6)$$

For the sake of summary, we present the results got comparing the acquisition with $70\mu l/min$ of Hexadecane and $10\mu l/min$ of water with the simulation carried out as described in the previous section, fixing $Q = 80\mu l/min$. The result, shown in the Figure 2.10, would reproduce the first peak of intensity, the one associated with the first meniscus of the droplet. The experimental profile has been zoomed in the zone of the peak. Anyway, the entire profile has just been showed in the first chapter (Figure 1.21).

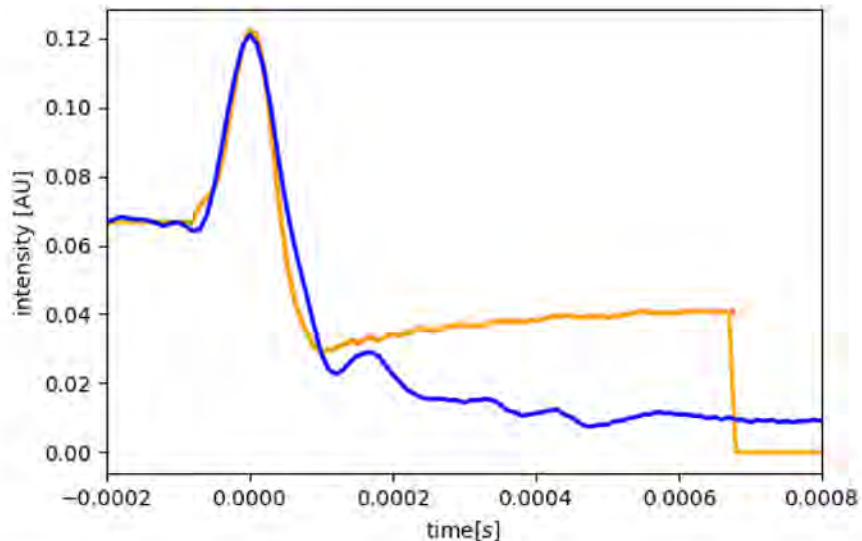


Figure 2.10: **Comparison with the first peak.** The blu line is a zoom of the acquisition profile around the first peak, the yellow one the numerical profile. The parameters used for the simulation are: 4 ellipses with 41 source points, $k = 1/2$, $z_{fin} = 90$, $z_{fin,real} = 40$ and $N_t = 120$, $N_a = 100$. For the comparison, the origin of the time axis has been fixed in the center of the peak, so part of the graphic is before zero.

Obviously, the same thing can be done for the peak relative to the second meniscus of the droplet. The difference, now, is that the simulation must take into account that semiaxes of the droplet must decrease at increasing t -step. The result of the simulation is shown in Figure 2.11.

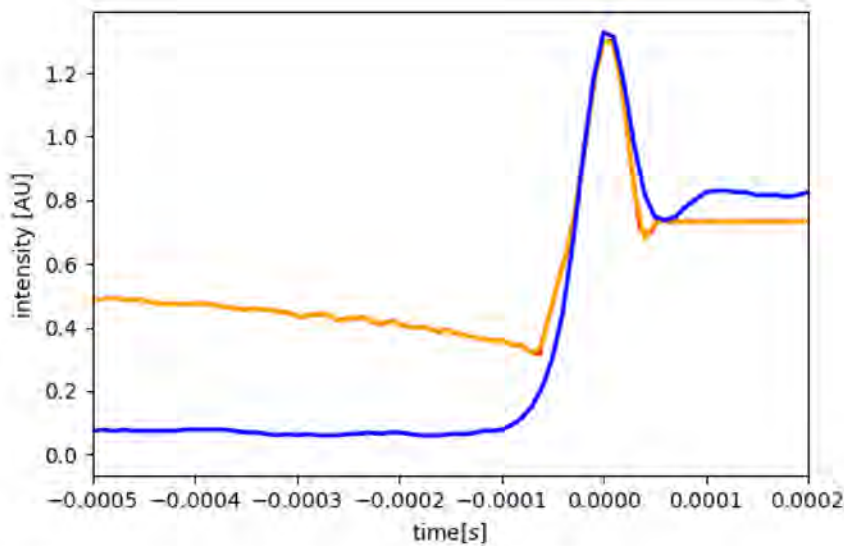


Figure 2.11: **Comparison with the second peak.** The parameters used for the simulation are: 4 ellipses with 41 source points, $k = 1/2$, $z_{fin} = 90$, $z_{fin_{real}} = 30$ and $N_t = 120$, $N_a = 100$.

Until now it can be confirmed that: *the major peaks in intensity are a direct result of the interference between the directed and refracted rays during the droplet's passage*. So, the first part of the droplet as a shape that resembles a lens. In other word, the peaks in intensity find an explanation in the geometrical nature of the menisci. A complete description of the phenomenon should take in account the fact that light is a wave. However, also with all the approximations taken, the result is very promising. The simulation perfectly reproduces the greatest peaks, but do not fit correctly the "body" of the droplet. In particular:

- The simulation does not let us understand the role of the so called *secondary peaks*, which is discussed, in a phenomenological way, in the next part of this thesis work.
- Moreover, the simulation, with this particular choice of droplet's shape and semiaxes' grown, can not reproduce the voltage in the middle of the droplet. However, this will be solved in the last section of this chapter.

2.4 Role of the parameters

In this section we want to analyse the changes in the numerical profile when a variation of parameters is taken into account. To perform this type of analysis we present here a focus around the best parameters value.

There are four parameters (N_{ell} , N_a , $z_{fin_{real}}$ and k), that can be divided in two categories:

- **Non physical parameters:** The number of ellipses N_{ell} (directly linked to the number of source points N_{sou} , as just said in the first section) and the number of rays N_a ;

- **Physical parameters:** $z_{fin_{real}}$ and k .

It is clear that the non physical parameters would not affect the result of the simulation, otherwise the code would not be useful. In fact, increasing the number of rays or the number of sources we expect that the numerical profile rather improves, but does not noticeably vary the shape of the computed curve.

Instead, the physical parameters are directly related to the shape of the droplet, so a variation of them, could have a deep impact.

First of all, we want to investigate the variation of the numerical profile with the non physical parameters.

2.4.1 Dependence on the non physical parameters

For now on, the values of the sides of the channel section and the position of the waveguide are fixed as in the last paragraph. In addition the number of steps was set to $N_t = 120$.

To study the role of the rays and sources number, a systematic study has been performed. First of all, we choose the droplet shape setting a priori the values of $z_{fin_{real}} = 40$ and $k = 1/2$.

We can now fix one of the non physical parameters and let the other one vary.

Fixing the source points and varying the rays

We begin fixing N_{ell} ¹ and let N_a vary. The chosen values for the source are listed below and all the numerical profiles obtained will be compared in the same plot.

Two ellipses: In Figure 2.12 are shown the numerical profiles in which $N_{ell} = 2$ (and so, $N_{sou} = 21$) and $N_a = 50, 100, 200, 500$ rays;

Three ellipses: In Figure 2.13 are shown the numerical profiles in which $N_{ell} = 3$ (and so, $N_{sou} = 31$) and $N_a = 50, 100, 200, 500$ rays;

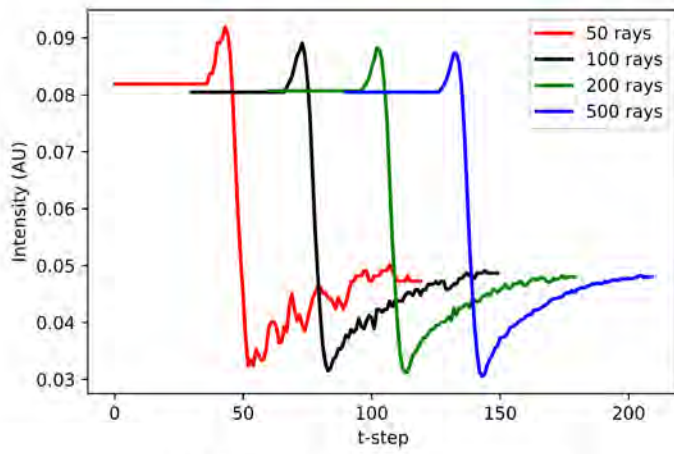
Four ellipses: In Figure 2.14 are shown the numerical profiles in which $N_{ell} = 4$ (and so, $N_{sou} = 41$) and $N_a = 50, 100, 200, 500$ rays;

In Figure 2.16, the simulated sources, are shown .

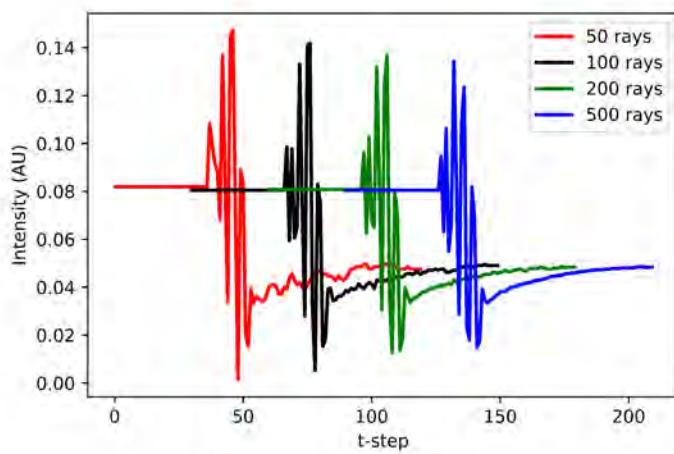
Fixing the rays and varying the source points

The other possibility is to fix N_a and let N_{ell} vary. In Figure 2.15 a comparison between the numerical profiles for different shape of the source is shown. We report only the integrated profiles, for the sake of simplicity .

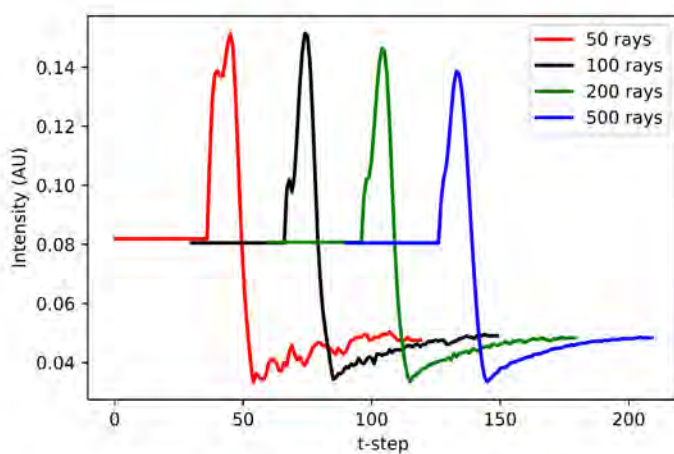
¹Unless otherwise advised, N_{sou} is fixed to be $N_{sou} = 10N_{ell} + 1$. With such a choice 10 source points are put in every ellipse, plus one in the center (see Figure 2.2).



(a) Simulations without interference.

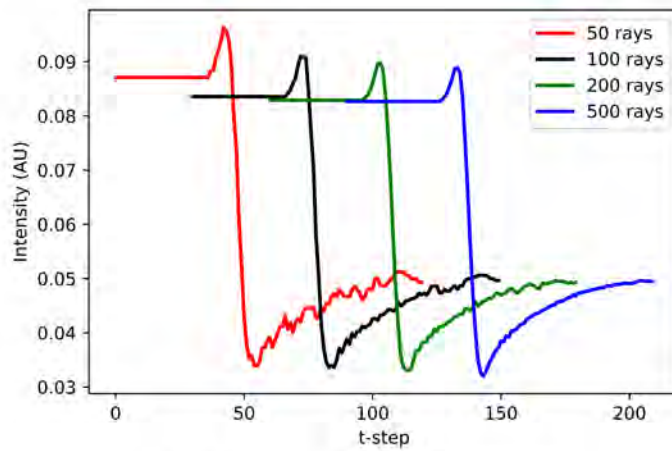


(b) Simulations with interference.

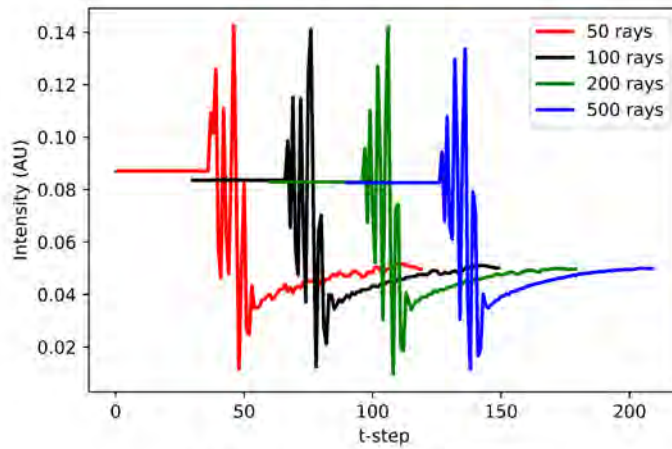


(c) Simulations with integrated interference.

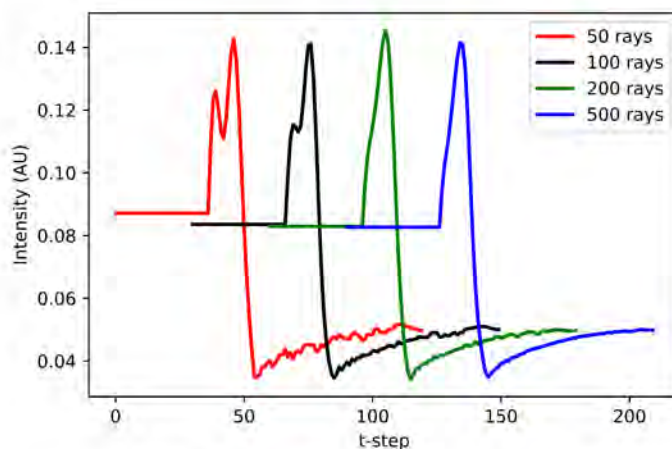
Figure 2.12: The results of the simulations with 2 source ellipses. Shift the profiles on the right of 30 steps was made to simplify the plot clearness.



(a) Simulations without interference.

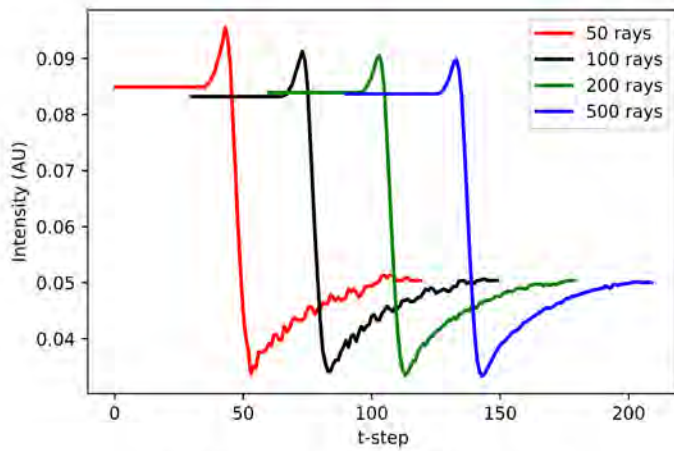


(b) Simulations with interference.

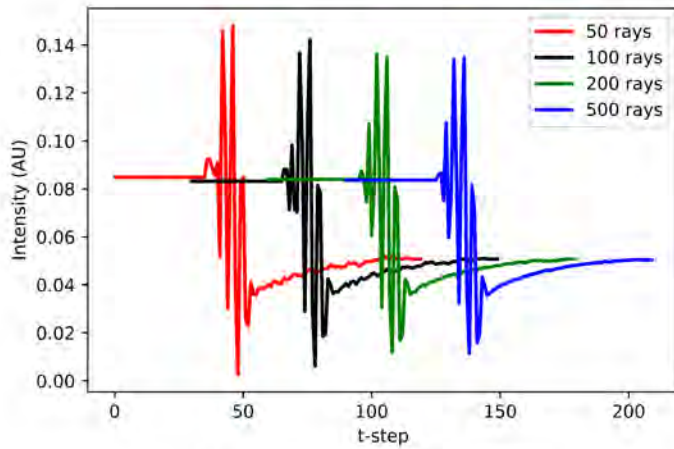


(c) Simulations with integrated interference.

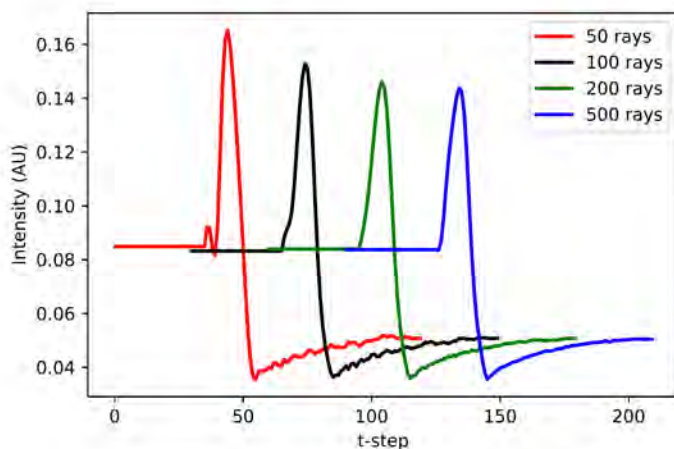
Figure 2.13: The results of the simulations with 3 source ellipses. Shift the profiles on the right of 30 steps was made to simplify the plot clearness.



(a) Simulations without interference.



(b) Simulations with interference.



(c) Simulations with integrated interference.

Figure 2.14: The results of the simulations with 4 source ellipses. Shift the profiles on the right of 30 steps was made to simplify the plot clearness.

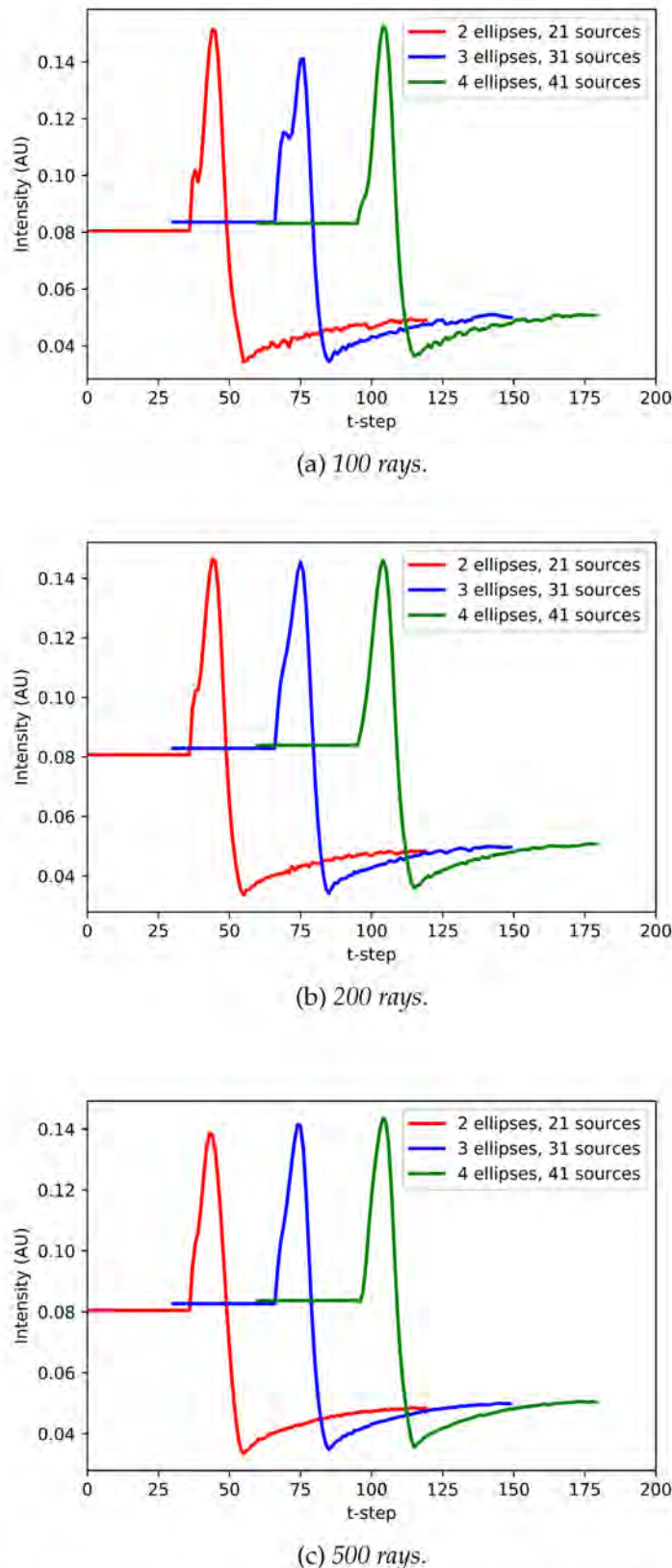


Figure 2.15: The results of the simulations (with integrated interference) fixing the rays and varying the number of sources. Shift the profiles on the right of 30 steps was made to simplify the plot clearness.

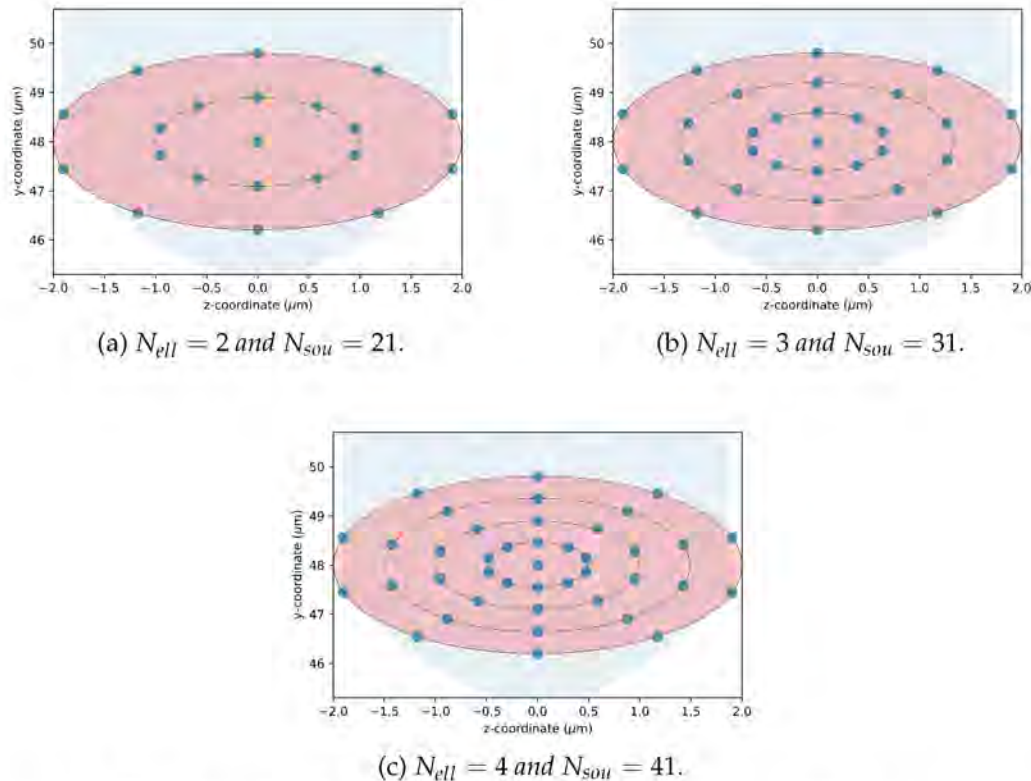


Figure 2.16: The simulated sources used. The distribution of the source points can be easily seen. (a) correspond to the one used to obtain the results in Figure 2.12, (b) for Figure 2.13 and (c) for Figure 2.14.

The following conclusion can be summarized:

- The variation of rays number means a slight variation in the numerical profile for every shape we could give to the source.
Anyway, with 2 and 3 ellipses the shape does not change, but we need at least 200 rays in order to make the interference contribute not variables. With 4 ellipses this problem does not exist and also 100 rays are a good approximation.
- A different number of sources appears to be less important than a different number of rays², apart for the simulations run with 100 rays. Anyway, if we look at the profile with $N_{ell} = 4$ (100 rays), we see that it is better than the other two (in the sense that it fit better the experimental profile).

At the end, we choose the match $N_a = 100$ with $N_{ell} = 4$, also because it makes the simulation heavier from the computational point of view (it reduces the computational time). Alternatively, $N_{ell} = 2$ or $N_{ell} = 3$ can be chosen, but $N_a > 200$ is recommended.

²This is probably because the size of the waveguide is an order of magnitude smaller than the channel width (5 μm against 200 μm respectively).

2.4.2 Dependence on droplet shape

The role of the non physical parameters is not significant , apart some artefacts occurring for low number of rays employed in the simulation ($N_a = 50$). So, $N_{ell} = 4$ and $N_a = 100$ has been fixed in the following. In order to enstablish whether both $z_{fin,real} = 40$ and $k = 1/2$ represent right choices, the impact of these two parameters was investigated.

First of all, in Figure 2.17 is shown the difference in the grown of semiaxes if a different value of k is choosen (namely, $k = 1/2$, $k = 1/3$ and $k = 1/5$).

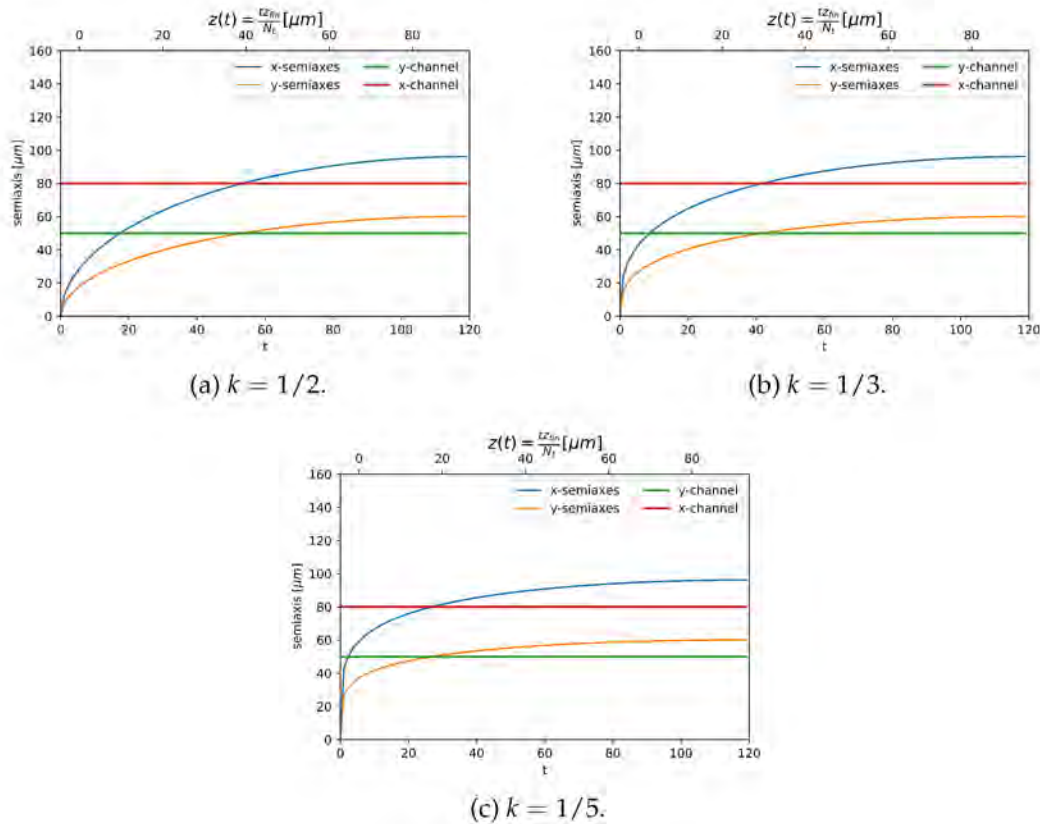


Figure 2.17: The grown of the semiaxes at different values of k . in panel (a) the semiaxes grown setting $k = 1/2$, in (b) $k = 1/3$ and in (c) $k = 1/5$.

As in the previous section, the parameters that we could vary are two: $z_{fin,real}$ and k . It is important to repeat that the role of $z_{fin,real}$ is to fix the t -step at which the semiaxes of the droplet are equal to the sides of the channel.

Setting $z_{fin,real} = 40$, in Figure 2.18 the numerical profiles (with integrated interference) at the different values of k just considered can be seen. Then, in Figure 2.19, the comparison with the data shows that the configuration with $k = 1/2$ is the most performing one, in the sense that both the height and the width of the peak are well reproduced, thing that do not happen for the other values the parameter.

This result is coherent with the fact that equations 2.2 and 2.3 would have $k = 1/2$ as exponent, because the initial intention was to reproduce an ellipsoidal meniscus. Anyway, in order to better understand what happens when the shape of the droplet is changed, we let this exponent vary. The final results is that the first idea was the best and *the ellipsoidal shape is a good choice for the geometry of the meniscus*.

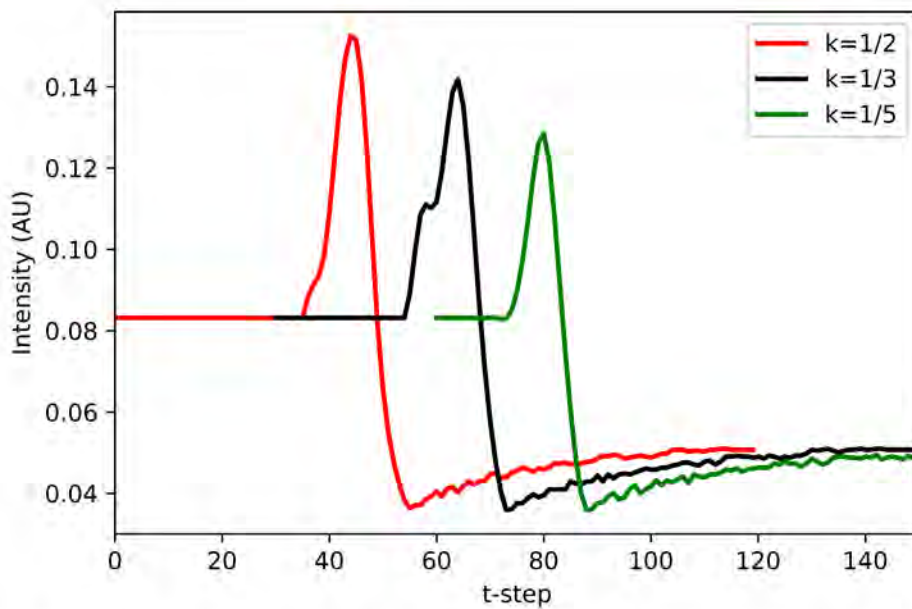


Figure 2.18: Simulation with integrated interference on varying k .

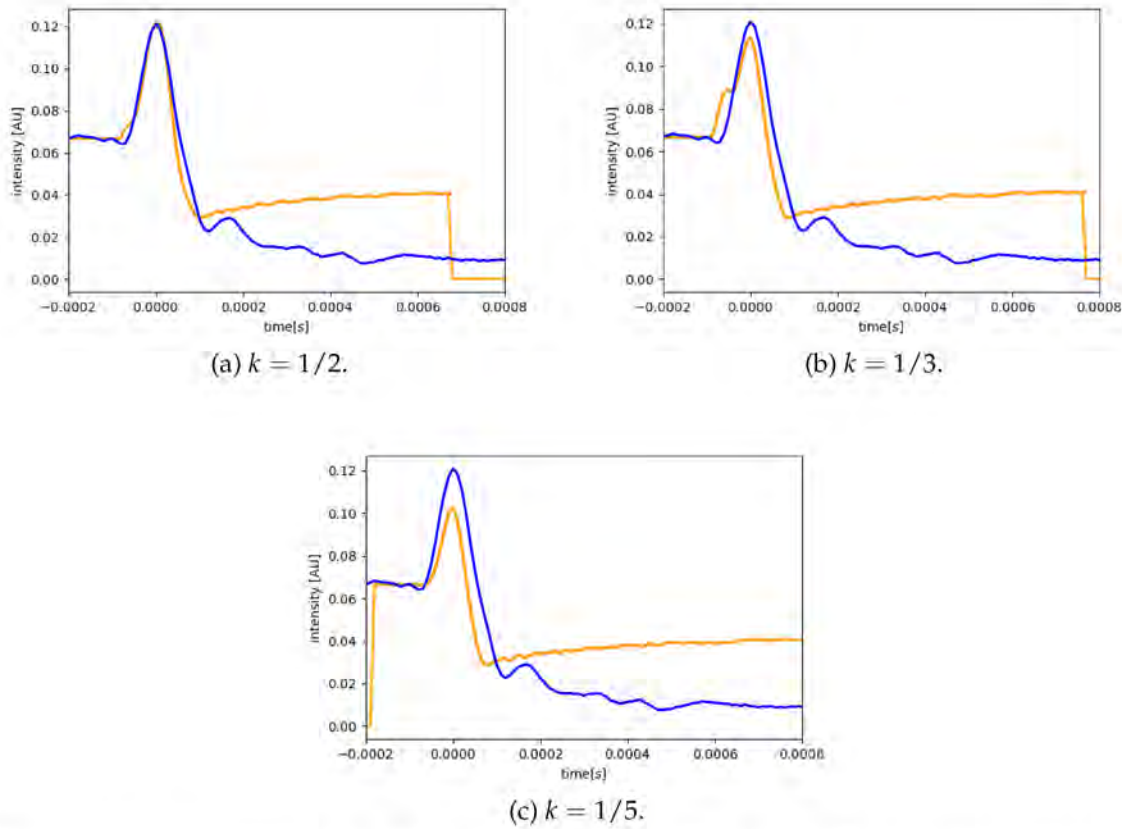


Figure 2.19: Comparison of the numerical profiles with the experimental ones on varying k . We can note that the more the shape of the meniscus differs from an ellipsoid ($k = 1/2$) the more the comparison with the experimental profile is inadequate.

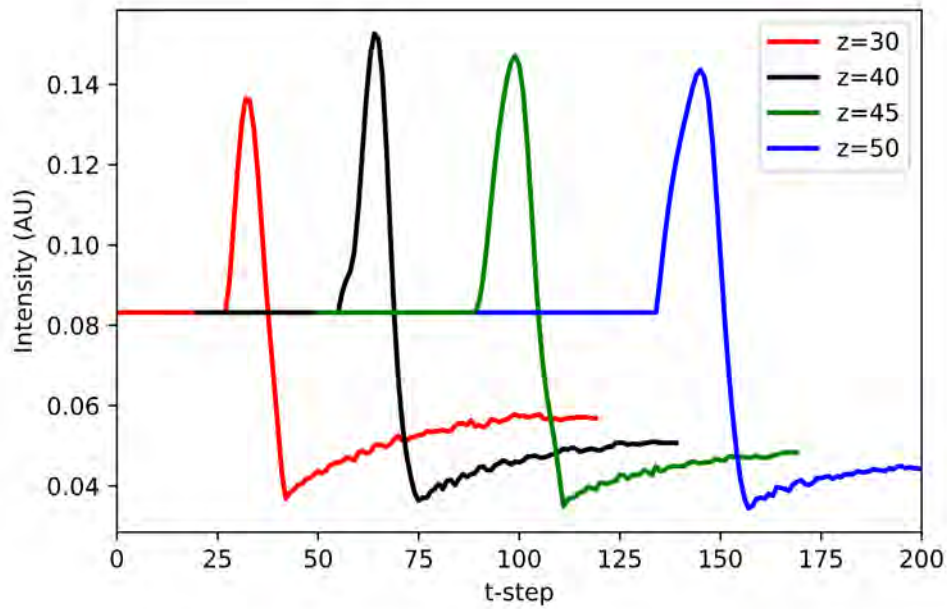


Figure 2.20: Numerical profiles on varying $z_{fin_{real}}$.

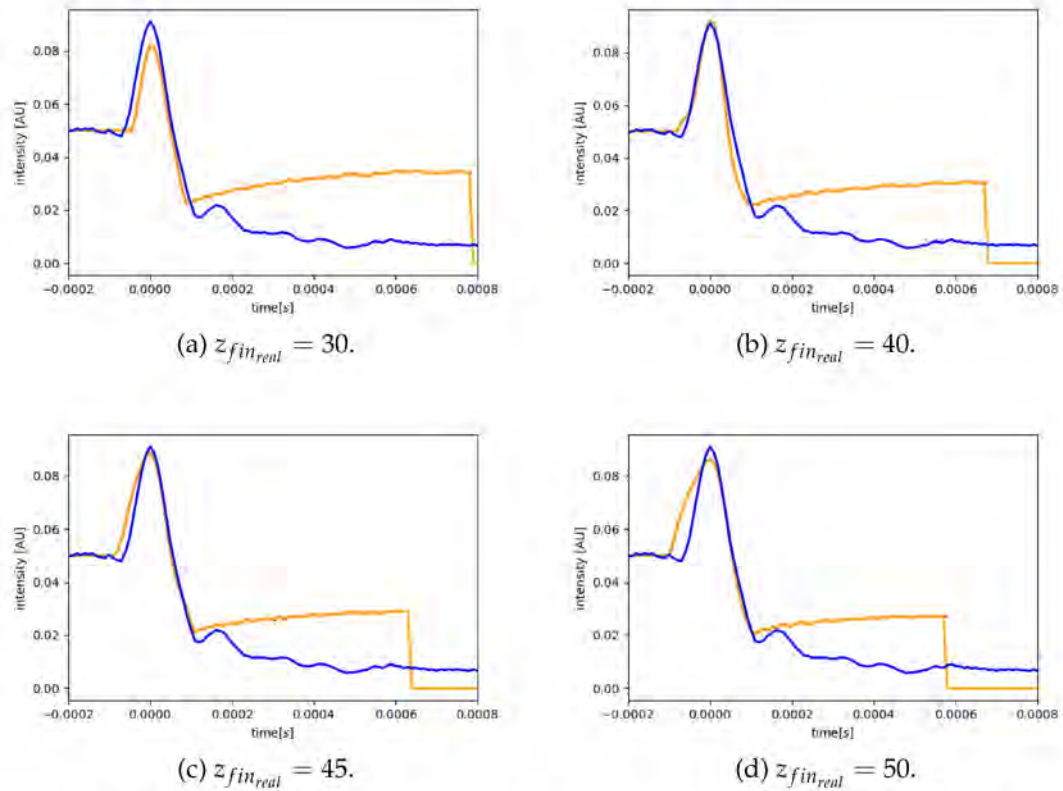


Figure 2.21: Comparison of the numerical profiles with the experimental ones on varying $z_{fin_{real}}$

And finally, the role of $z_{fin_{real}}$ must be investigated. Basing on the results just obtained, we fix $k = 1/2$. In Figure 2.20 the numerical profiles (with integrated interference) with $z_{fin_{real}} = 30, 40, 45$, are shown.

The chosen values are in the range that better reproduces the width of the meniscus of the droplet. In Figure 2.21, the comparison with the experimental data are shown. With $z_{fin_{real}} = 30$ both the width and the height of the numerical profile are not compatible with the ones of the experimental profile, instead with $z_{fin_{real}} = 45$ or $z_{fin_{real}} = 50$ only the width is not compatible. On the contrary $z_{fin_{real}} = 40$ produces a profile that is completely compatible with the experimental one. The above analysis let us confirm that $N_{ell} = 4$ (so $N_{sou} = 41$), $N_a = 100$, $z_{fin_{real}} = 40$ and $k = 1/2$ is a good choice of parameters for the simulation. In the sense that it is the best compromise to limit the computational time without compromising the results accuracy.

2.5 Center of the droplet

If we look at the longer droplets, the plateau of water (namely, the internal zone of constant and very low voltage) basically represents the center of the droplet. However, with the code just presented we are not able to reproduce this part of the acquisition profile.

This is due to the fact that, after $z = z_{fin_{real}}$, the droplet forth across the channel. This not physical behaviour was not a problem when our objective was to reproduce the peak in intensity. On the contrary, we need to solve it if we want to describe other parts of the acquisition profile. So, the software was slightly modified, in order to simulates the middle of a long droplet.

The code is almost the same of the previous sections, with the a difference that a number of steps $N_{filling}$, was added after the N_t . Substancially, the simulation can be divided in two parts:

1. In the initial N_t steps the droplet do not exed the channel. This was obtained setting $z_{fin} = z_{fin_{real}}$. With this hypothesis the semiaxes grow, as a function of z , as in equations 2.7 and 2.8

$$x_{dr}(z) = l_{ch} \left(1 - \left(\frac{z - z_{fin}}{z_{fin}} \right)^2 \right)^{1/2} \quad (2.7)$$

$$y_{dr}(z) = h_{ch} \left(1 - \left(\frac{z - z_{fin}}{z_{fin}} \right)^2 \right)^{1/2} \quad (2.8)$$

2. When the channel has completely filled (so when $t = N_t$) the sections in the (x, y) plane of the droplet must change. In particular, the section now is thought to be composed by the union of four ellipses. It is decided to fix the centers of the ellipses (that generates the entire droplet) in the diagonal of the rectangle (representing the channel) and at every step the semiaxes reduces in a linear way, with the constrain that the ellipse must be aways tangent to the channel. This evolution can be seen in Figure 2.22, where only the evolution of the upper and right part of the sections is shown. The reader must imagine that the

total droplet is the union of four such ellipses, one in each angle of the rectangle.

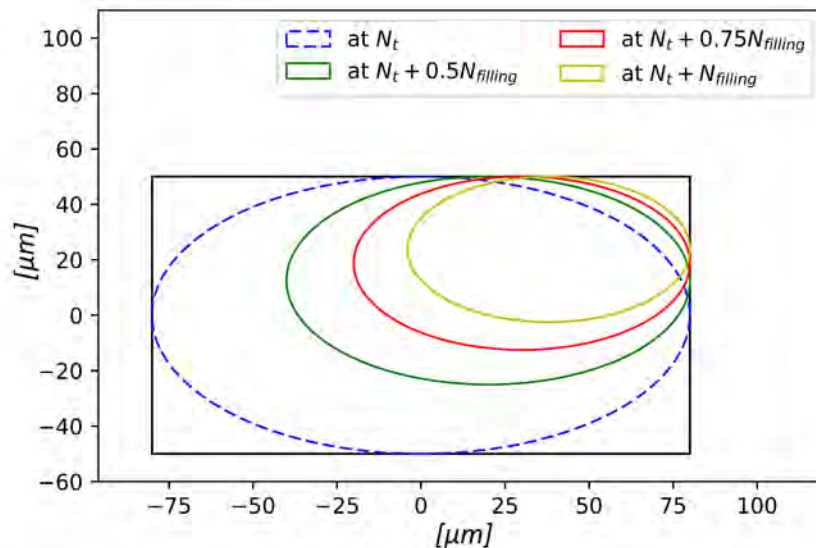


Figure 2.22: The section of the droplet. At the step N_t the section of the droplet is an ellipse perfectly inscribed in the channel, in the other $N_{filling}$ steps it changes its form. In this plot only the right and upper part of the droplet's section.

In this way, the droplet fills completely the channel in N_t steps, and in the other $N_{filling}$ steps modifies its form laying down in the channel, but never exceeds it. The final shape of the droplet is thought to be the one in Figure 2.23.

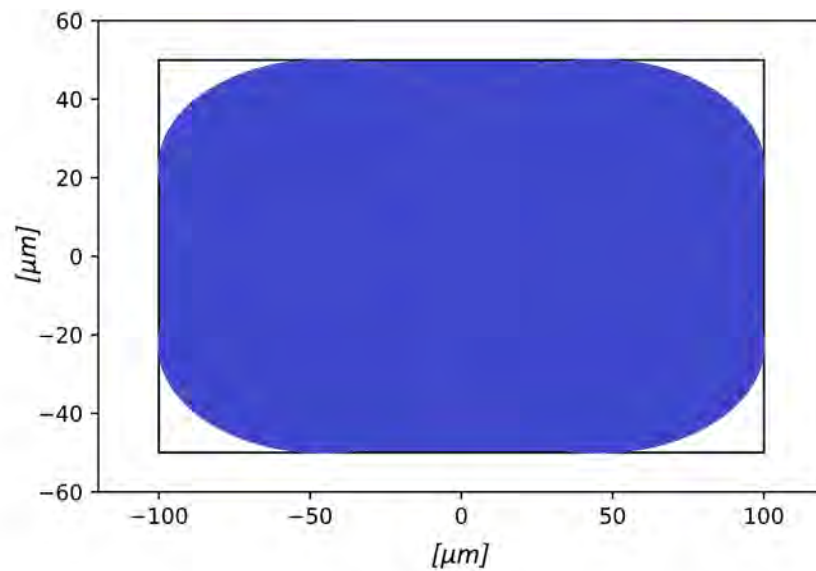


Figure 2.23: The final form of the droplet. The shape at the $N_t + N_{filling}$ step.

It is important to say that we have neglected the role of the microfilm of oil at the wall. This film is necessary for the correct flow of the droplets in the microchannel. Anyway, the hypothesis is justified by the fact that it is some order of magnitude smaller than the other quantity [73, 74, 75].

The code has been run with $N_{filling} = 20$ and, for the other parameters, the same value of the previous chapter (namely, $N_{ell} = 4$, $N_{sou} = 41$, $N_t = 120$, $z_{fin} = 90$) has been chosen.

The software is, in all the aspects, the same of the previous sections, so it computes the directed and refracted rays, the mean angle and the mean optical path of every ray (at every step). The only interest in this analysis is to see what happens in the center of the droplet. We know that the voltage in this zone is very low, i.e. the intensity transmitted by the droplet is almost zero. When the droplet has completely filled the channel the directed rays do not exist anymore and the only possibility to transmit light is through the refracted rays. Substantially, it is sufficient to compute the refracted rays at every step, to understand how they evolve in time. To reproduce the acquisition profile, it is necessary that the refracted rays, during the $N_{filling}$ steps in which the droplet lays down on the channel, goes to zero.

In Figure 2.25, after the step $N_t = 120$, the number of refracted rays (orange dots) begins to decrease, until it reaches a null value. Moreover, we can observe this trend also in the mean angle of the rays, that is shown in Figure 2.24. In fact, after the classical increasing (due to the passage of the meniscus), the mean angle of the refracted rays goes to zero, because no rays effectively arrives to the waveguide facing on the other side of the channel.

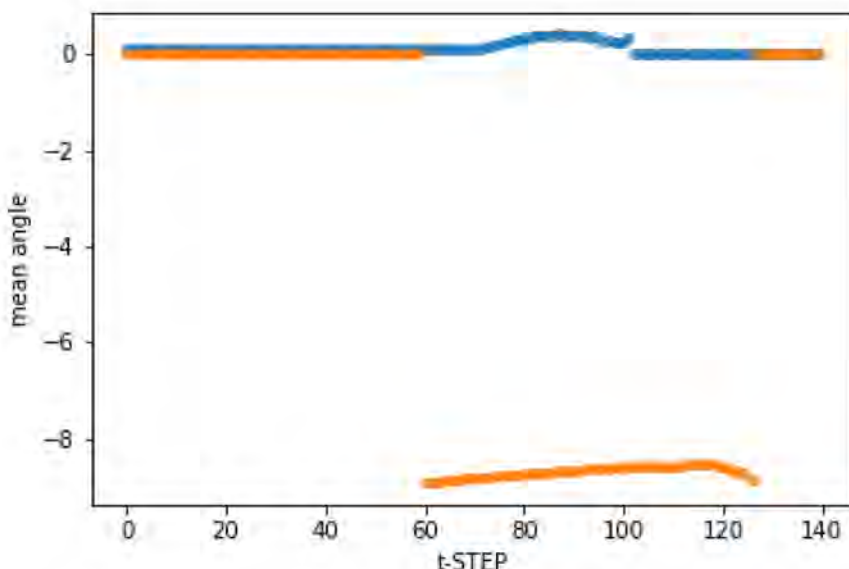


Figure 2.24: **Mean angle of directed and refracted rays.** The blue dots represent the mean angle of directed rays, while the orange dots the one of the refracted rays.

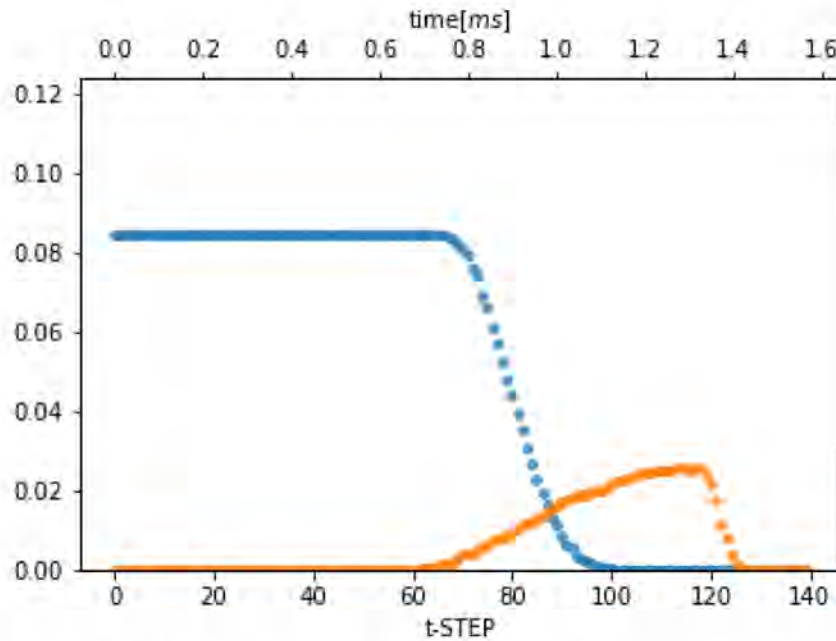


Figure 2.25: **Result of the simulation.** The blue dots represent the directed rays, the orange one the refracted rays. When the droplet begins to lay down in the channel, the number of refracted rays begin to decrease, until they reach zero.

The result of the simulation is promising. The fact that the droplet lays down in the channel (and do not exceed it) permits the refracted rays to decrease until zero (namely, the intensity goes to zero). This is the demonstration that in the middle of a long droplet the water do not fill completely the channel, but assumes a shape similar to the one in Figure 2.23. Therefore, also the plateau of water, like the peaks, is a geometrical phenomenon, in the sense that is completely linked to the shape of the interface water-oil.

We have just seen that a little difference in the shape of the droplet produce a zeroing in the refracted rays. In this context, it is clear that, maybe, the hypothesis made of neglecting the contribute of the microfilm, could not be reality. In fact, this contribute could be very important in the analysis that we want to make.

Chapter 3

Analysis of droplet shape

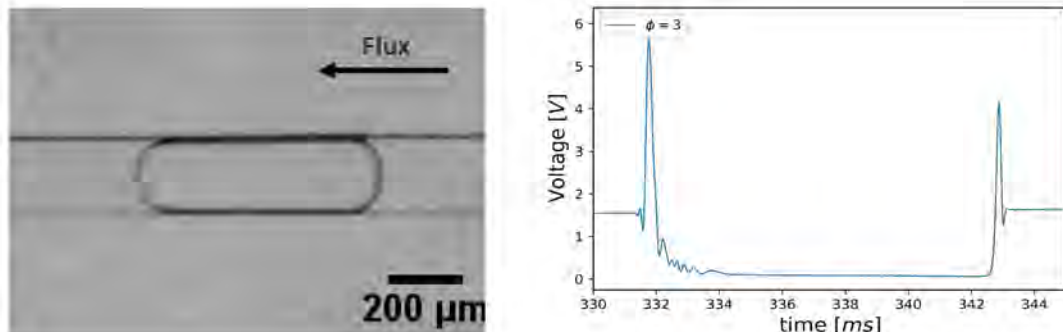
In this chapter we want to analyse the effect of the droplet passage into the optical transmission and to understand the role of every part of the intensity profile. To do this the images of the droplets (at every flux) has been taken with the microscope. The droplets were generated both in the cross-flowing and flow-focussing configurations respectively.

Firstly the images recorded with the microscope, associated with the relative acquisition profile for each flux, are reported all in the same reference system. For the sake of simplicity the unit length is reported in the first picture only. In addition, in every droplet image, the left meniscus is the advancing one and the right is the bottom (in other words, the droplet travel from the right to the left). For the entire chapter ϕ is the ratio of the fluxes of the continuos and dispersed phases. In the case of interest $\phi = \frac{Q_{oil}}{Q_{water}}$, where Q are the $\mu l/min$ of substance injected in the microchannel.

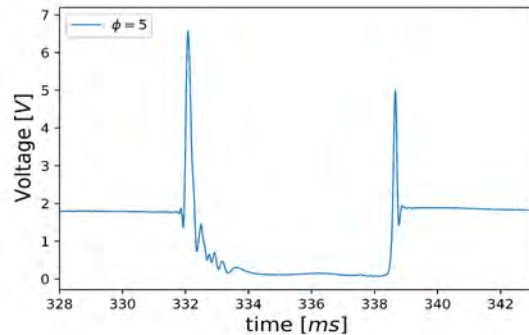
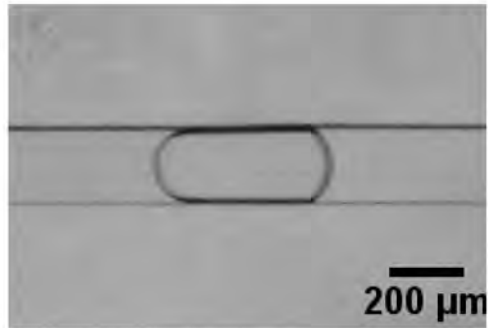
We mantained the same time scale in every acquisition profile, apart for the cross-flowing configuration after $\phi = 22$. In this case the images begin to be too small and there is the risk of missing details, so we had to change it.

- **Cross-flowing** Images taken in the cross-flowing configuration. On the left we can see the microscope acquisitions and on the right the optical transmission profile respectively.

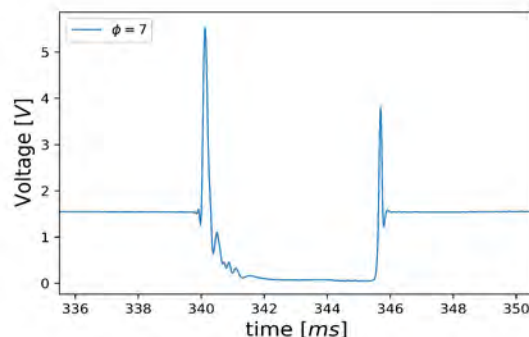
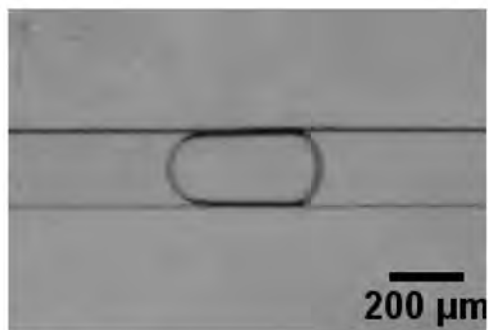
30 $\mu l/min$ oil, 10 $\mu l/min$ water



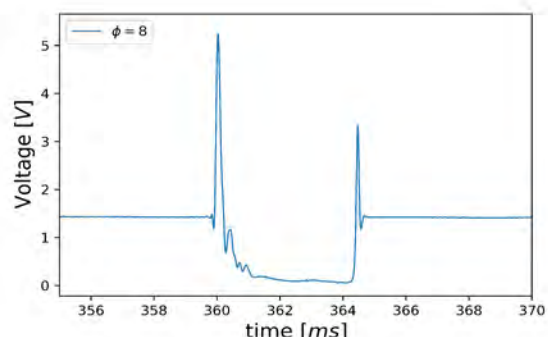
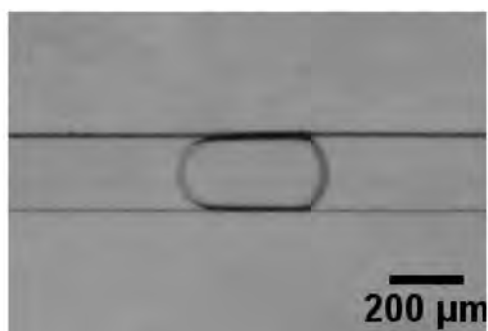
$50 \mu\text{l}/\text{min}$ oil, $10 \mu\text{l}/\text{min}$ water



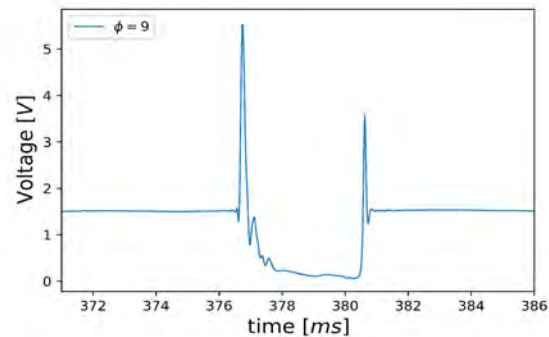
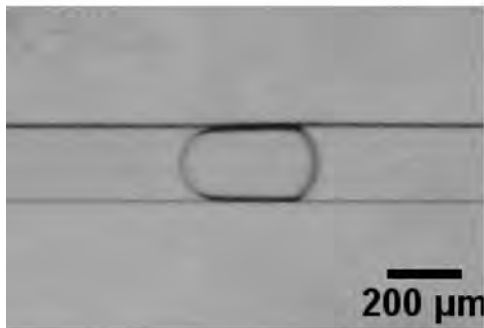
$70 \mu\text{l}/\text{min}$ oil, $10 \mu\text{l}/\text{min}$ water



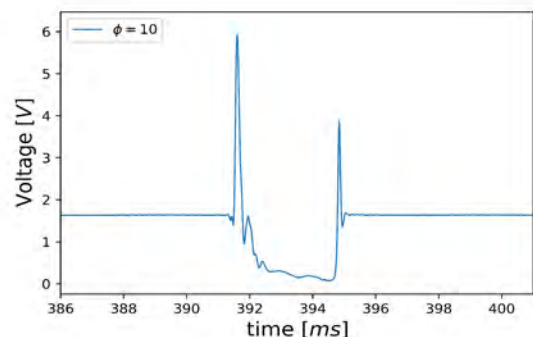
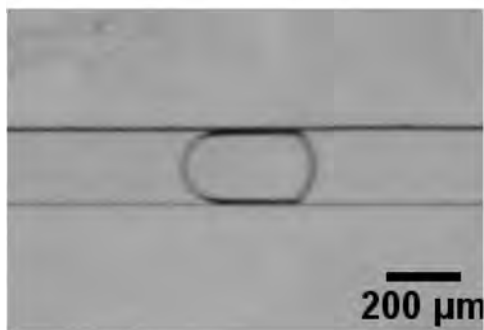
$80 \mu\text{l}/\text{min}$ oil, $10 \mu\text{l}/\text{min}$ water



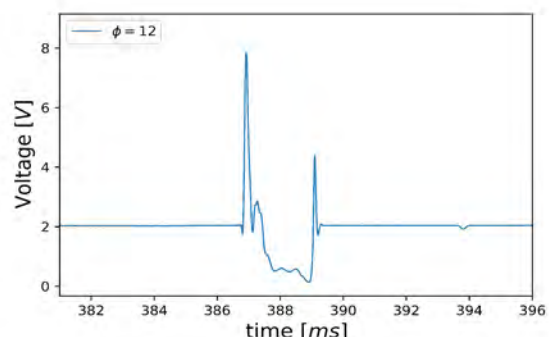
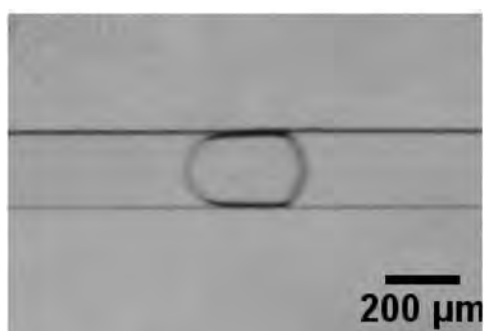
$90 \mu\text{l}/\text{min}$ oil, $10 \mu\text{l}/\text{min}$ water



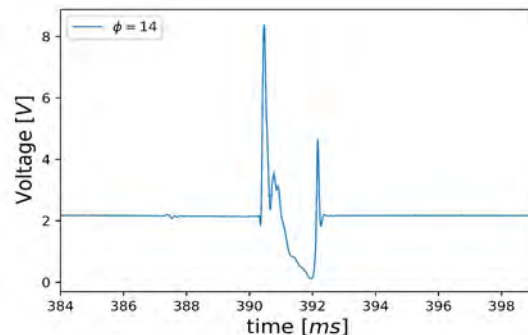
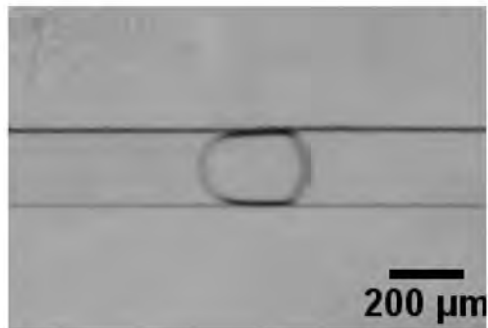
$100 \mu\text{l}/\text{min}$ oil, $10 \mu\text{l}/\text{min}$ water



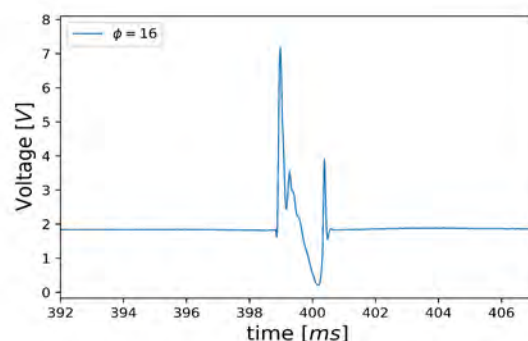
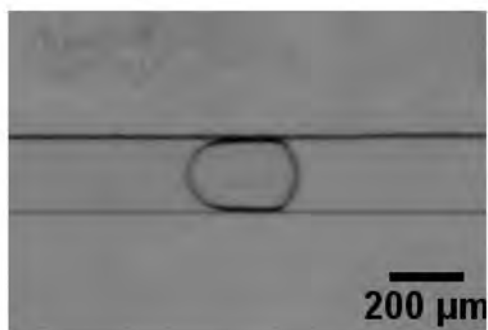
$120 \mu\text{l}/\text{min}$ oil, $10 \mu\text{l}/\text{min}$ water



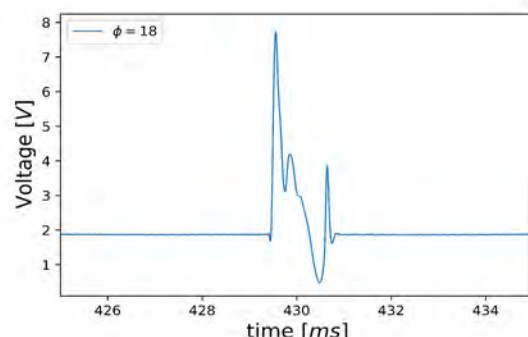
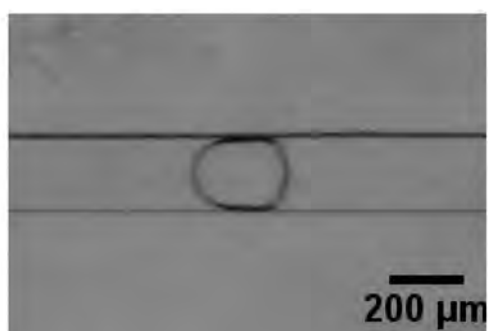
$140 \mu\text{l}/\text{min}$ oil, $10 \mu\text{l}/\text{min}$ water



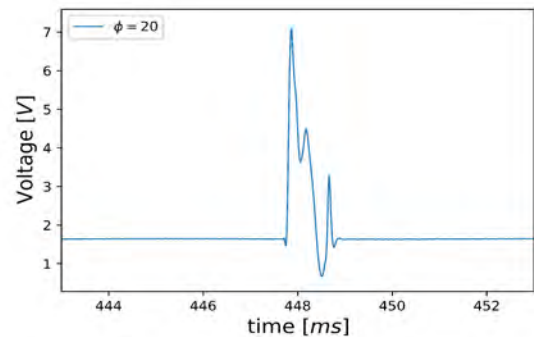
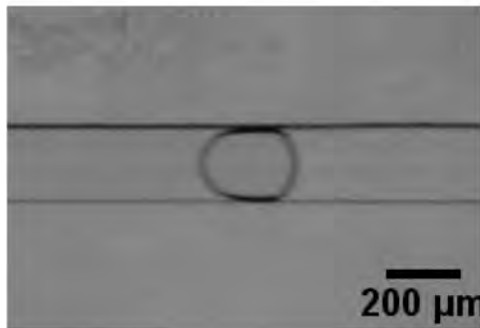
$160 \mu\text{l}/\text{min}$ oil, $10 \mu\text{l}/\text{min}$ water



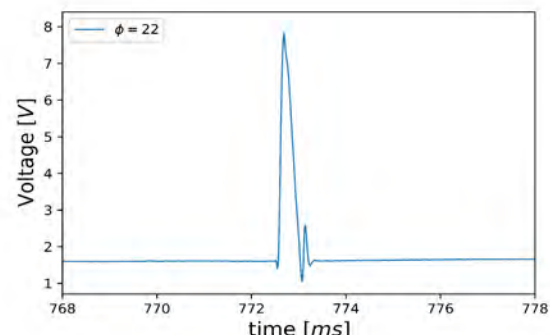
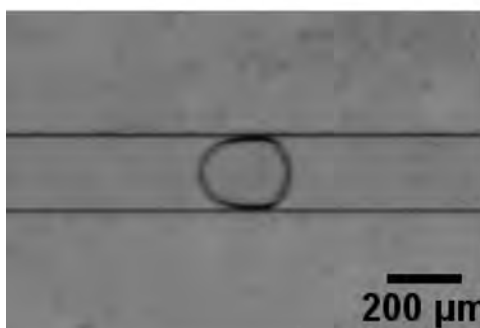
$180 \mu\text{l}/\text{min}$ oil, $10 \mu\text{l}/\text{min}$ water



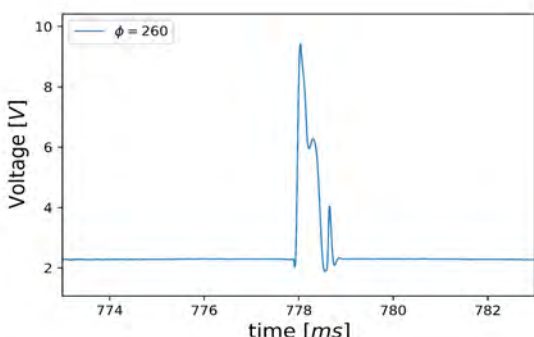
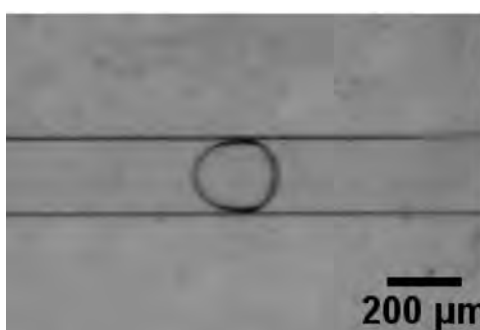
200 $\mu l/min$ oil, 10 $\mu l/min$ water



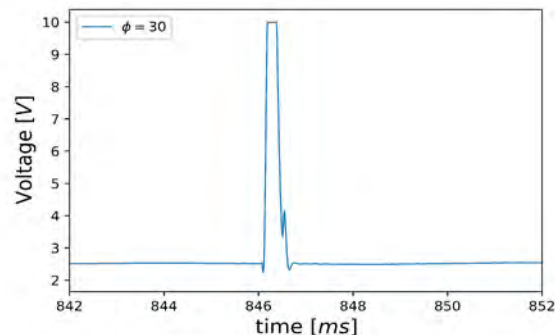
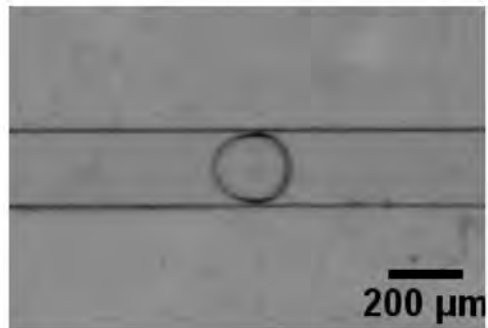
220 $\mu l/min$ oil, 10 $\mu l/min$ water



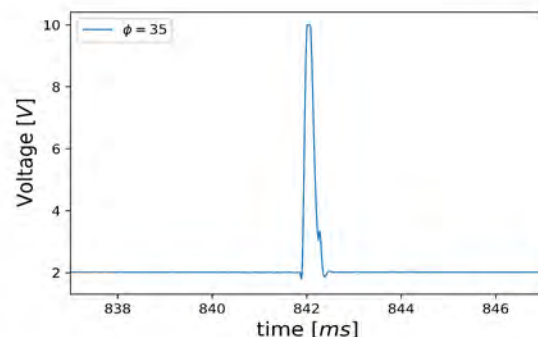
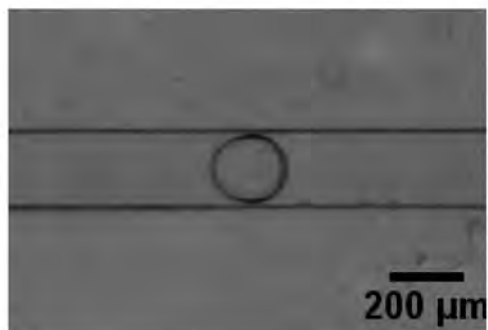
260 $\mu l/min$ oil, 10 $\mu l/min$ water



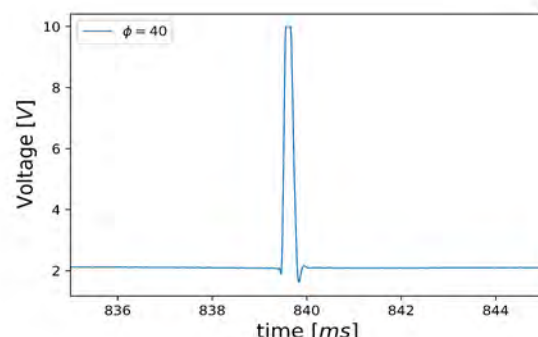
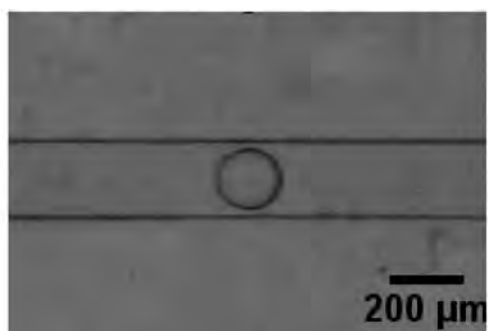
$300 \mu\text{l}/\text{min}$ oil, $10 \mu\text{l}/\text{min}$ water



$350 \mu\text{l}/\text{min}$ oil, $10 \mu\text{l}/\text{min}$ water

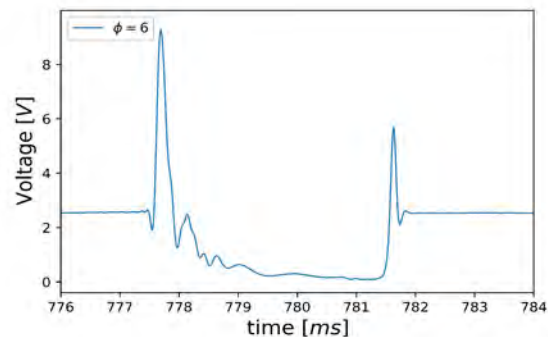
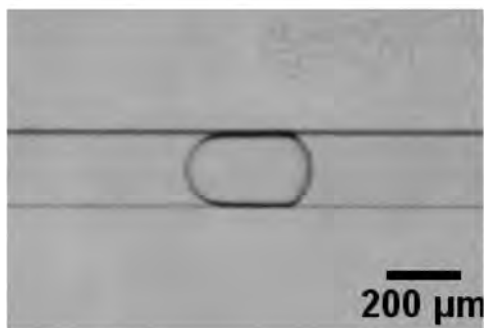


$400 \mu\text{l}/\text{min}$ oil, $10 \mu\text{l}/\text{min}$ water

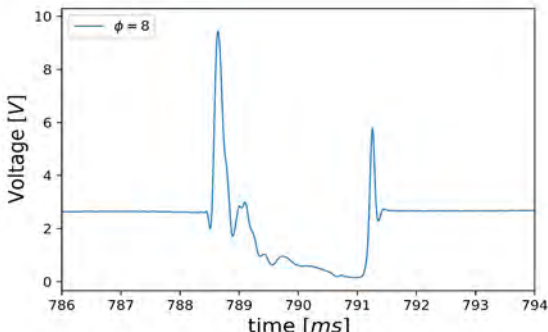
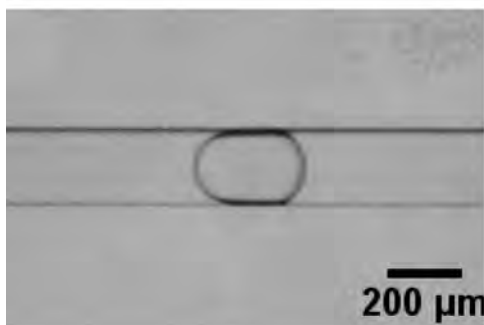


- **Flow-flowing** Images taken in the flow-flowing configuration. The flux relative to oil must be interpreted as the total flux of oil, namely half in the upper channel and half in the lower one.

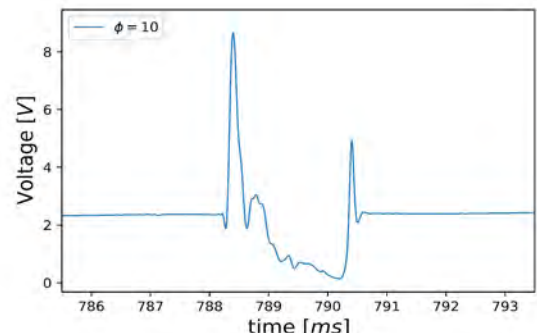
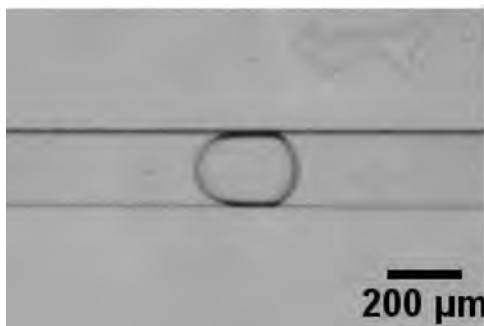
$60 \mu\text{l}/\text{min}$ oil, $10 \mu\text{l}/\text{min}$ water



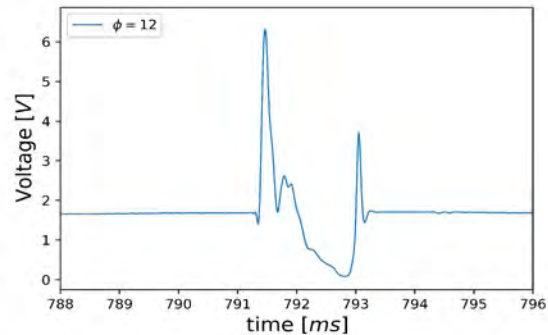
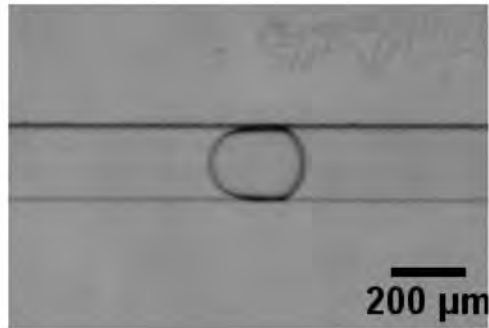
$80 \mu\text{l}/\text{min}$ oil, $10 \mu\text{l}/\text{min}$ water



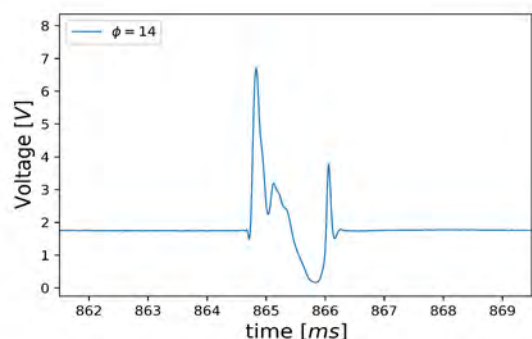
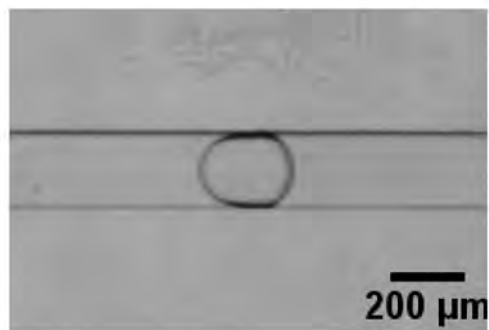
$100 \mu\text{l}/\text{min}$ oil, $10 \mu\text{l}/\text{min}$ water



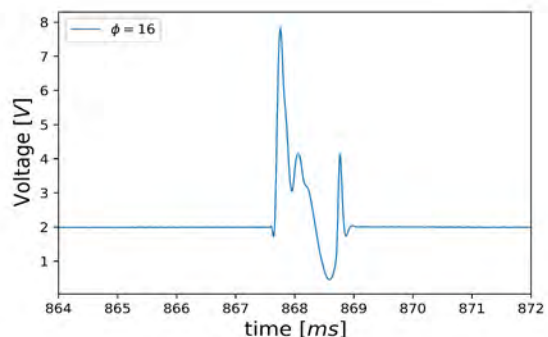
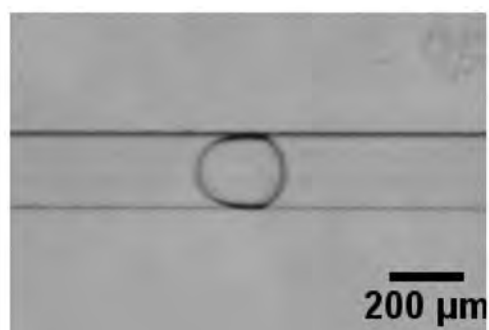
$120 \mu\text{l}/\text{min}$ oil, $10 \mu\text{l}/\text{min}$ water



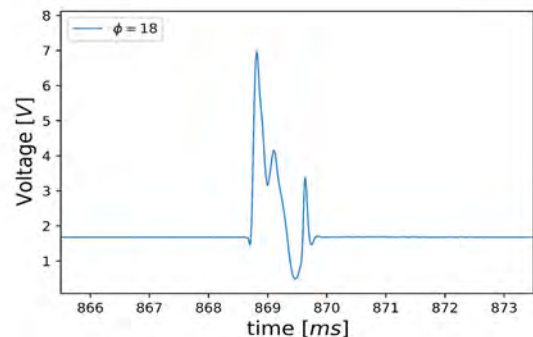
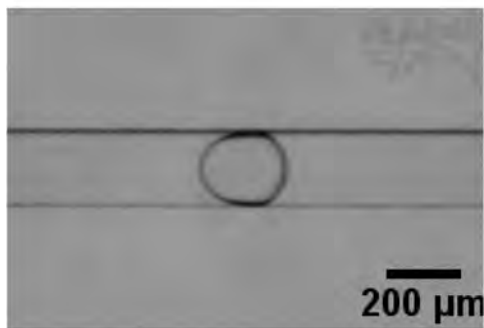
$140 \mu\text{l}/\text{min}$ oil, $10 \mu\text{l}/\text{min}$ water



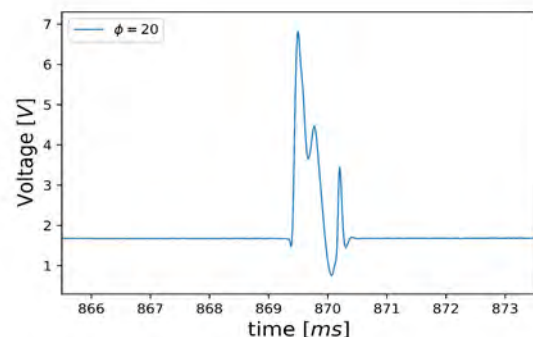
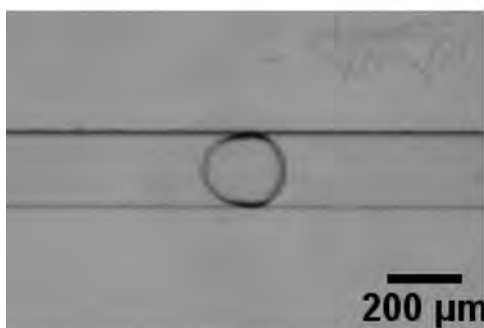
$160 \mu\text{l}/\text{min}$ oil, $10 \mu\text{l}/\text{min}$ water



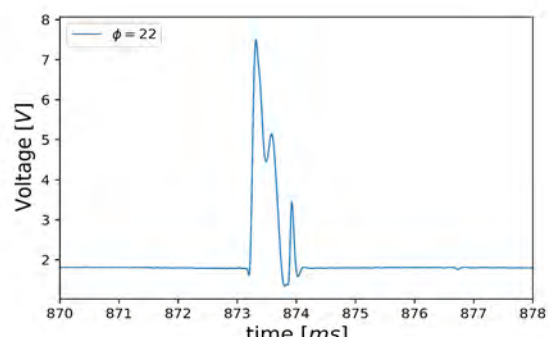
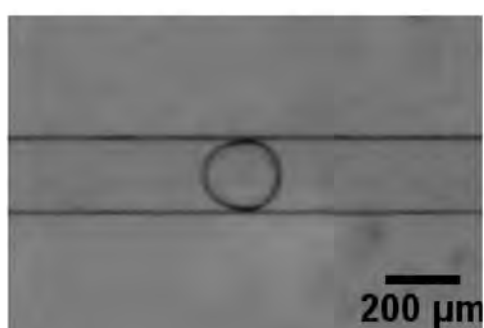
$180 \mu\text{l}/\text{min}$ oil, $10 \mu\text{l}/\text{min}$ water



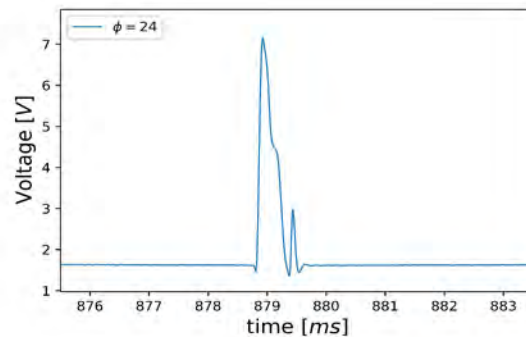
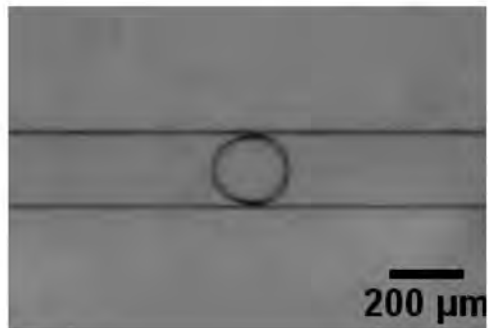
$200 \mu\text{l}/\text{min}$ oil, $10 \mu\text{l}/\text{min}$ water



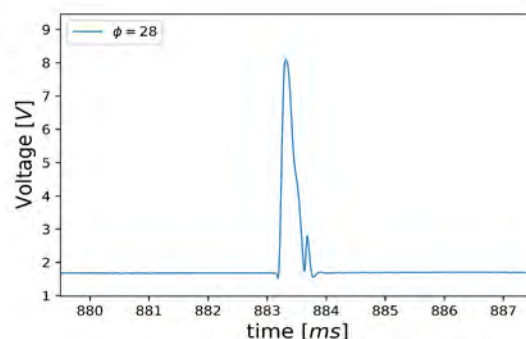
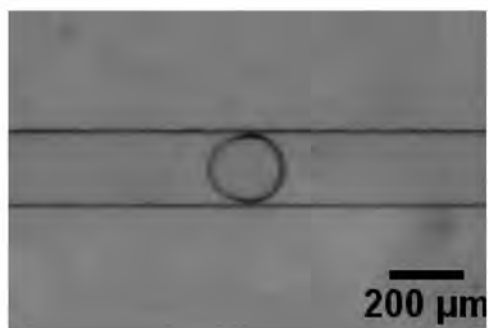
$220 \mu\text{l}/\text{min}$ oil, $10 \mu\text{l}/\text{min}$ water



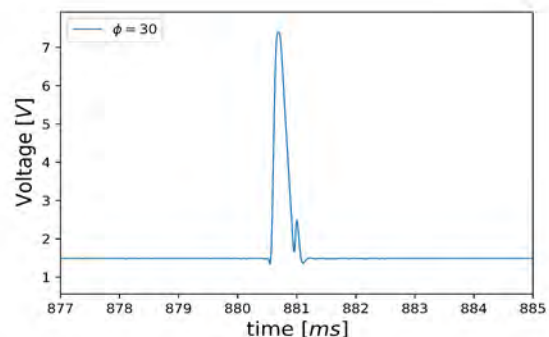
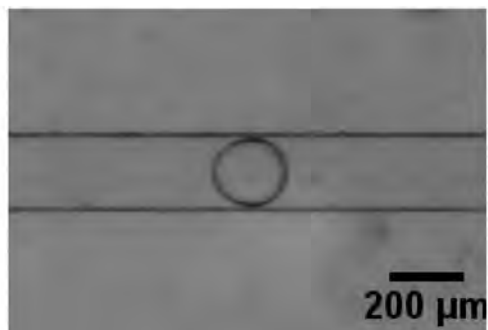
240 $\mu\text{l}/\text{min}$ oil, 10 $\mu\text{l}/\text{min}$ water



280 $\mu\text{l}/\text{min}$ oil, 10 $\mu\text{l}/\text{min}$ water



300 $\mu\text{l}/\text{min}$ oil, 10 $\mu\text{l}/\text{min}$ water



In Figure 3.1 an example of the droplet passage effect is reported in detail. In particular, we have highlighted the *minimun* and the *secondary peaks*. The region between the secondary peaks and the minimun is the plateau of water.

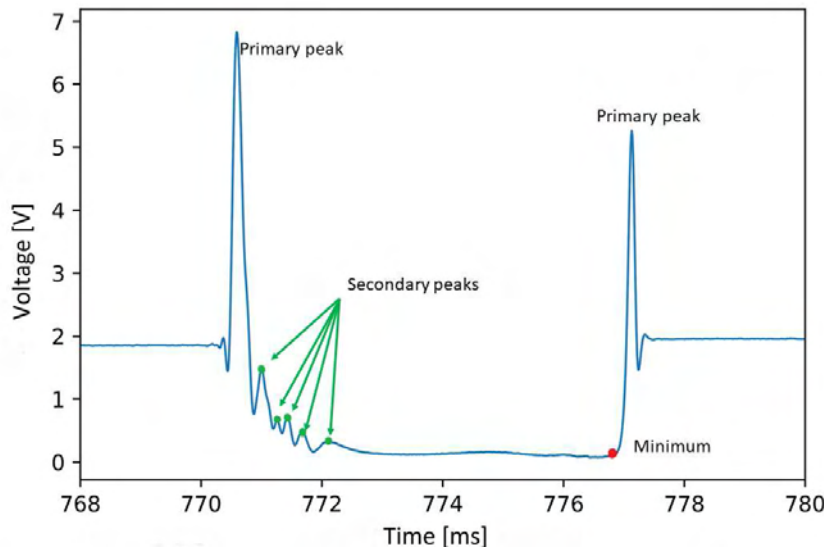


Figure 3.1: Minimum and secondary peaks in the acquisition profile. Profile obtained with the fluxes of $70 \mu\text{l}/\text{min}$ (oil) and $10 \mu\text{l}/\text{min}$ (water) in the cross-flowing configuration. The red dot represent the minimum, the green ones the secondary peaks.

By comparing the shape of the droplets and the optofluidic profiles, there are some relevant aspects deserving attention:

- The “secondary peaks” change significantly their form with the fluxes change;
- The minimum of intensity increases at the increasing of the fluxes;
- Simultaneously with the increasing of the minima the secondary peaks begin to merge into each other, the profile begins to shrink and the plateaux of water reduces consequently. When the shape of the droplet is approximatly spherical, the optical trasmission profile is similar to a gaussian, with no secondary peaks.

In the sections below this evidences will be debated.

3.1 Role of the “secondary peaks”

At the first sight, the shape of every acquisition profile could seem similar for every flux. There are always two peaks, that delimit the droplet, and a region, between them, at very low values of signal intensity (that we call the plateau of water). The length of the droplets can not be directly estimated nor being used as a first indicator, because it is complicated to evaluate it with only a fast look. However, there is a part of the profile strongly dependent on fluxes: the secondary peaks. We can say that they are representative of the droplet shape, but the reason of their origin is still unknown.

Since these fingerprints are common in all the droplets, in this thesis we investigated their effect and origin, from a phenomenological point of view. Let us look at the images of the droplets taken with microscope. In the previous chapter we have demonstrated that the higher intensity peaks correspond to the first part of the meniscus, the one that has a shape comparable with an ellipsoid. If we look with more attention we can notice that the right meniscus (so the receding one) is different from the left one (the advancing one), in particular the rear meniscus is more net than the advancing one, i.e. it can be fitted with an ellipsoid that intersect the channel, as shown in Figure 3.2 (a). On contrary the advancing one tends to lay down on the channel, so, the curvature is different from one of the rear meniscus. In Figure 3.2 (b), we show that it is impossible to interpolate the advancing meniscus with an ellipsoid, so that the curvature is completely different from the one of the rear. We choose to use an ellipsoid just for the sake of simplicity, our scope is only to show the substantial difference from the geometry of the two menisci.

In Figure 3.2 the difference between the two menisci is shown.

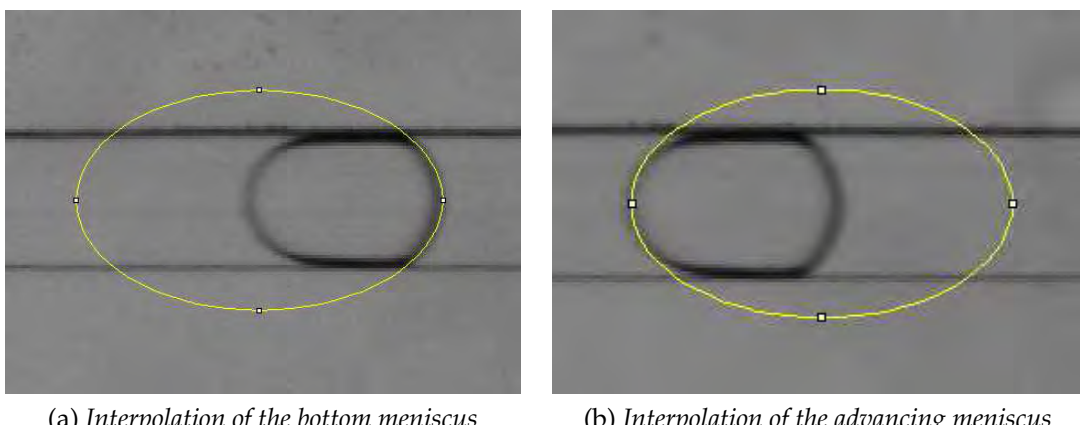


Figure 3.2: Receding and advancing meniscus of the droplet interpolated with an ellipsoid. Droplet obtained with the fluxes of $160 \mu\text{l}/\text{min}$ (oil) and $10 \mu\text{l}/\text{min}$ (water) in the cross-flowing configuration.

If we look at the acquisition profiles, as just said, we can note that the two peaks are not similar. The difference between the advancing and bottom peak relies in the secondary peaks. The bottom one is a net peak that rises directly from the plateaux of water, whereas the advancing one does not end in the plateaux of water in a net way, but it shows the secondary peaks.

The comparison between the microscope images and the profiles is now clear.

- The bottom meniscus has a well defined shape that can be fitted with an ellipsoid. The interface between water and oil has a *discontinuity* in the shape, in the sense that immediately passes from a flat profile to an elliptic one. This is reflected in the acquisition profile: the voltage in the water plateau passes from an almost constant value (with a flat shape) and to a sudden increase. A discontinuity in the shape is reflected in a discontinuity in the voltage. Note that the word "discontinuity" is used in an inappropriate way. It is not a real discontinuity, but only a very sharp edge. If we could have the mathematical form of the acquisition profile, we could state that the derivative, computed in a

right neighbourhood of the minimum (red point in Figure 3.1), should have a very high value.

- The advancing meniscus has a particular shape, it resembles an ellipsoid in the first part but after it change its curvature, laying down on the channel. In this case the interface between water and oil *do not have any discontinuity*, and this affecting also the acquisition profile. The first peak does not fall immediately in a water plateau, but the fall is “soften” by a modulation that produces the secondary peaks.

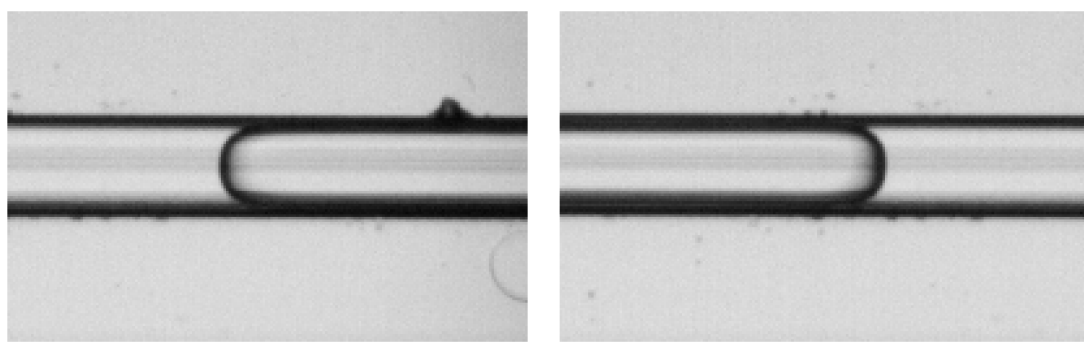
In conclusion, this thesis demonstrates that the secondary peaks are the direct consequence of a curvature (of the meniscus) that is different from an ellipsoidal one. In fact our simulation reproduced perfectly the first peak, but not the secondary ones because we do not have the correct shape of droplet. Instead, the bottom peak is well reproduced by the simulation because its form is coherent with hypothesized one, as we had noted in Figure 3.2 (a).

We want now to prove further the roles of the secondary peaks. We note that the difference between advancing and bottom meniscus is more emphasized at high values of flux. So, at low fluxes the droplet should become approximately symmetric. If the droplet is symmetric (i.e. the two menisci are identical) no difference between the two peaks in the acquisition profile should be present.

In Figure 3.3 we can see the two menisci of a long droplet (namely, the fluxes are fixed to $20 \mu\text{l}/\text{min}$ for oil and $30 \mu\text{l}/\text{min}$ for water) and in Figure 3.4 it is shown its acquisition profile.

The secondary peaks are not completely absent, but they are minimized in intensity. This means that the droplet is not really symmetric, but the advancing meniscus is still a bit different from the rear one. Nevertheless this is a proof that the role of the secondary peaks is exactly the one mentioned above.

This fingerprint allows to detect shape modification or asymmetries otherwise non resolved by standard fast imaging procedure.



(a) *The right meniscus (advancing one)*

(b) *The left meniscus*

Figure 3.3: Long droplet. Droplet obtained with the fluxes of $20 \mu\text{l}/\text{min}$ (oil) and $30 \mu\text{l}/\text{min}$ (water) in the cross-flowing configuration. It is impossible to show all the droplet (is too long), so only the two menisci are reported.

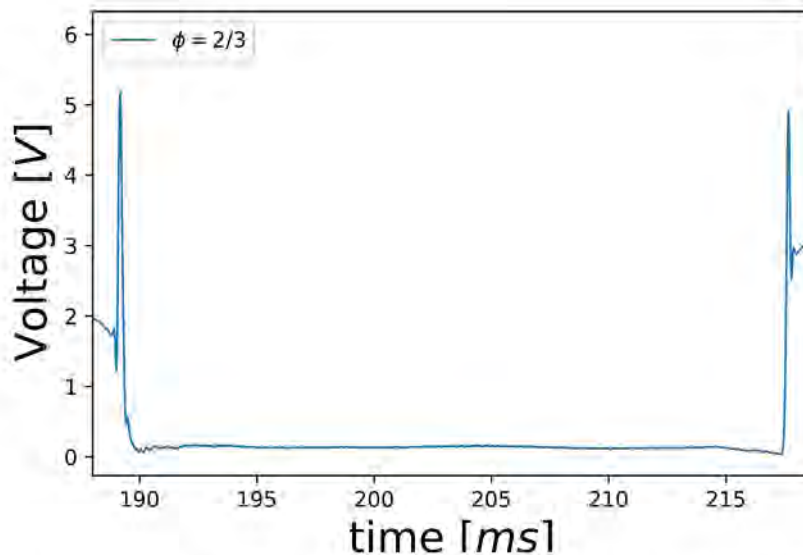


Figure 3.4: **Acquisition profile of a long droplet.** Droplet obtained with the fluxes of $20 \mu\text{l}/\text{min}$ (oil) and $30 \mu\text{l}/\text{min}$ (water).

Another demonstration of the role of the secondary peaks can be the fact that they begin to disappear at high fluxes. When we reach a very high value of ϕ the secondary peaks begin to merge together until they disappear. This happens when the shape of the droplet begins to be an *oval*, so there is no more a net difference between the first and the second part of the meniscus (no more zones could be fitted with ellipsoids and other with different shapes).

In this section we have only analysed the images and given a phenomenological description of the secondary peaks. The physical meaning of their form, namely a complete theoretical description of the phenomenon, is still ongoing.

3.2 High production frequency analysis

The other aspect that can be noted is the variation of the minimum value V_{\min} of intensity. If we look at all the fluxes we can observe that the minimum becomes important when the plateaux of water disappears, namely when $\phi > 12$. The difference begins to appear at very high values of the oil flux. In Figure 3.5 the best values of flux has been chosen to let the reader appreciate this difference.

If we look also at the images taken with the microscope of the droplets at this fluxes, it emerges that the shape changes dramatically. The higher is the flux of oil, the lower the droplet touches the sides of the channel. When the minimum in intensity is completely disappeared, the droplet does not touch the sides of the channel anymore.

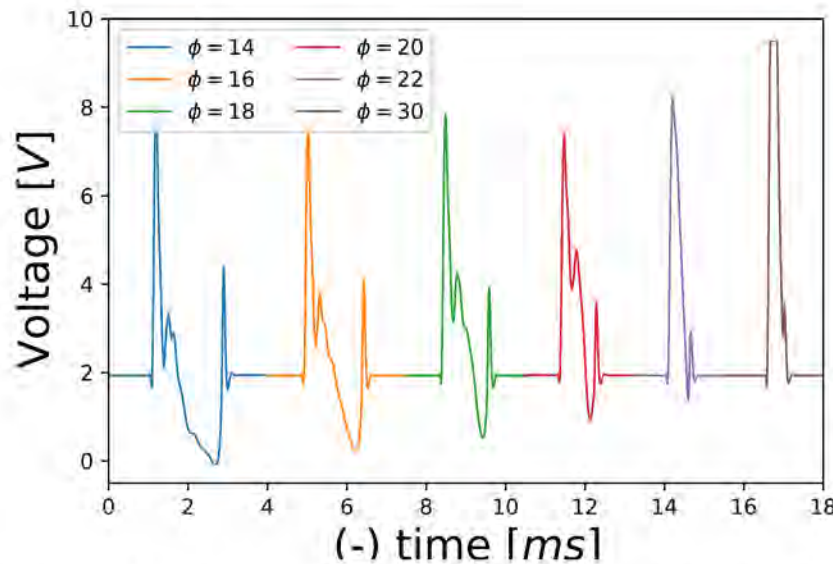


Figure 3.5: A complete vision of the variation of the minima in the voltage. Some fluxes have been chosen to let the reader note the difference between them. When the flux of oil is very high ($300 \mu\text{l}/\text{min}$) there is no minimum.

So, the idea is that the values of the minimum (V_{min}) can be a marker of how much the droplet is attached to the channel.

In Chapter 1 all the different operational regimes have been presented. Since there is a minimum in intensity we can say that we are in the *squeezing* regime. Otherwise, when the minimum disappeared we can say there is a transition to the *dripping* regime. In this thesis we investigate the role of V_{min} and established that it is the representative parameter of this transition.

For every flux ϕ , the minimum value V_{min} was estimated for every droplet in the file. In order to compare features from different conditions, this minimum is divided by the voltage of the continuous phase, V_{oil} . For each flux we have a file of about 200 droplets, so the software that analyses every file shows as final result an histogram. The code computes the mean value and, as associated error, was chosen the standard deviation. The error of the quantity V_{min}/V_{oil} is obtained by the propagation of error formula.

The data has been taken both in the cross-flowing and flow-focussing configuration, so the analysis below is made for both.

In the tables below we can see the computed values of V_{min} , V_{oil} and V_{min}/V_{oil} for every flux¹ with the relative error. For high value of fluxes, the minimum does not exist, so the ratio has been fixed to one. Firstly we reported the results for the cross-flowing configuration.

The values in Table 3.1 can be plotted, as in Figure 3.6, with the relative error.

¹Both the chosen flux ϕ_{theo} and the experimental flux ϕ_{exp} with its error were reported. The experimental values were evaluated as just made in the first chapter.

Table 3.1: The values of V_{min} , V_{oil} and V_{min}/V_{oil} for every flux, with the relative error, for the cross-flowing configuration.

ϕ_{theo}	ϕ_{exp}	$\sigma_{\phi_{exp}}$	$V_{min}(\text{V})$	$\sigma_{V_{min}}(\text{V})$	$V_{oil}(\text{V})$	$\sigma_{V_{oil}}(\text{V})$	$\frac{V_{min}}{V_{oil}}$	$\sigma_{\frac{V_{min}}{V_{oil}}}$
3	3.001	0.008	0.072	0.006	1.794	0.008	0.040	0.003
5	4.99	0.01	0.063	0.006	1.18	0.04	0.053	0.005
6	6.00	0.02	0.069	0.007	1.72	0.02	0.040	0.004
7	7.00	0.02	0.065	0.007	1.53	0.01	0.042	0.005
8	8.00	0.02	0.078	0.007	1.47	0.03	0.053	0.005
9	9.00	0.03	0.081	0.009	1.53	0.01	0.053	0.006
10	10.00	0.03	0.090	0.003	1.635	0.003	0.055	0.002
12	12.01	0.03	0.14	0.06	2.14	0.08	0.07	0.03
14	14.00	0.04	0.119	0.004	2.16	0.01	0.055	0.002
16	16.00	0.05	0.22	0.01	1.91	0.05	0.115	0.006
18	18.01	0.05	0.46	0.02	1.82	0.08	0.25	0.02
20	19.94	0.06	0.64	0.02	1.64	0.01	0.39	0.01
22	22.02	0.06	1.09	0.03	1.7	0.1	0.66	0.04
26	26.00	0.07	1.89	0.08	2.33	0.08	0.81	0.04
30	30.08	0.08	//	//	//	//	1	//
35	35.0	0.1	//	//	//	//	1	//
40	40.1	0.1	//	//	//	//	1	//

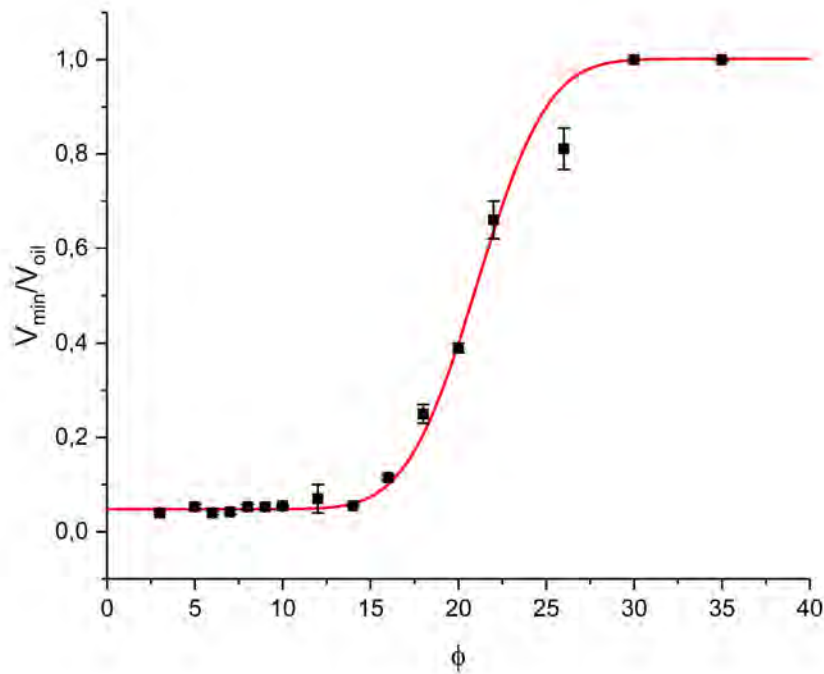


Figure 3.6: Transition from *squeezing* to *dripping* in the cross-flowing configuration.

We can notice that the transition, in the case of cross-flowing, occurs between $\phi = 15$ and $\phi = 30$, where the dripping regime replaces the squeezing one.

- For $\phi < 15$ the acquisition profiles present a stable value for the minimum and a plateau of water actually exists² (if we look at the microscope images we can observe that effectively the droplet look attached to the channel).
- From $15 < \phi < 30$ the plateau of water does not exist anymore and the minimum begins to have a crucial role, the droplet is going to detached from the channel, but a little zone attached still exists.
- For $\phi > 30$ the minimum disappeared³ and the transition to dripping regime is completely happened.

In Figure 3.7 we can see the difference between $\phi = 10$ and $\phi = 35$ (so before the beginning of transition, and when the transition is occurred).

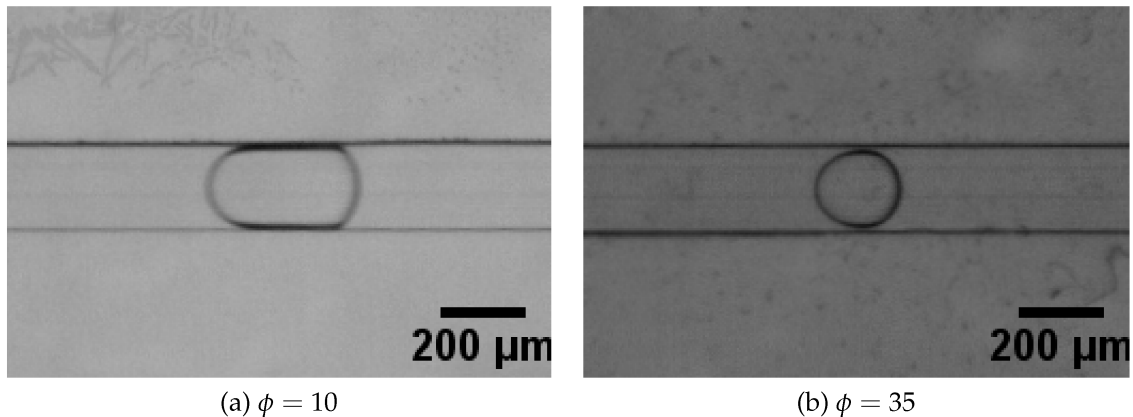


Figure 3.7: Detachment of the droplet from the channel in cross-flowing configuration. On the left the microscope image for $\phi = 10$, on the right for $\phi = 30$.

Now, the same analysis will be made for the flow-focussing configuration. In Table 3.2 are reported the computed values of voltages and in Figure 3.8 the plot of them.

The situation is the same of the cross-flowing configuration. The only difference is that, in flow-focussing, the detachment takes place at smaller values of ϕ . The difference between $\phi = 12$, before the beginning of transition, and $\phi = 28$, when it is occurred) can be seen in Figure 3.9.

²The plateau of water shrinks at the increasing of the fluxes, but it still exists.

³In the sense that the “minimum” is at higher voltage than the oil, so it is no more a minimum.

Table 3.2: The values of V_{min} , V_{oil} and V_{min}/V_{oil} for every flux, with the relative error, for the flow-focussing configuration.

ϕ_{theo}	ϕ_{exp}	$\sigma_{\phi_{exp}}$	$V_{min}(\text{V})$	$\sigma_{V_{min}}(\text{V})$	$V_{oil}(\text{V})$	$\sigma_{V_{oil}}(\text{V})$	$\frac{V_{min}}{V_{oil}}$	$\sigma_{\frac{V_{min}}{V_{oil}}}$
6	6.01	0.01	0.11	0.01	2.5	0.1	0.044	0.004
8	8.00	0.02	0.16	0.01	2.6	0.2	0.062	0.006
10	10.01	0.02	0.14	0.03	2.4	0.1	0.06	0.01
12	12.00	0.02	0.085	0.004	1.72	0.08	0.049	0.003
14	14.01	0.03	0.18	0.02	1.9	0.1	0.09	0.01
16	16.03	0.03	0.46	0.02	1.99	0.01	0.23	0.01
18	18.01	0.04	0.5	0.03	1.74	0.06	0.29	0.02
20	20.04	0.04	0.73	0.07	1.65	0.04	0.44	0.04
22	22.04	0.04	1.38	0.03	1.81	0.03	0.76	0.02
24	24.03	0.05	1.53	0.08	1.83	0.08	0.84	0.06
28	28.00	0.06	//	//	//	//	1	//
30	30.05	0.06	//	//	//	//	1	//

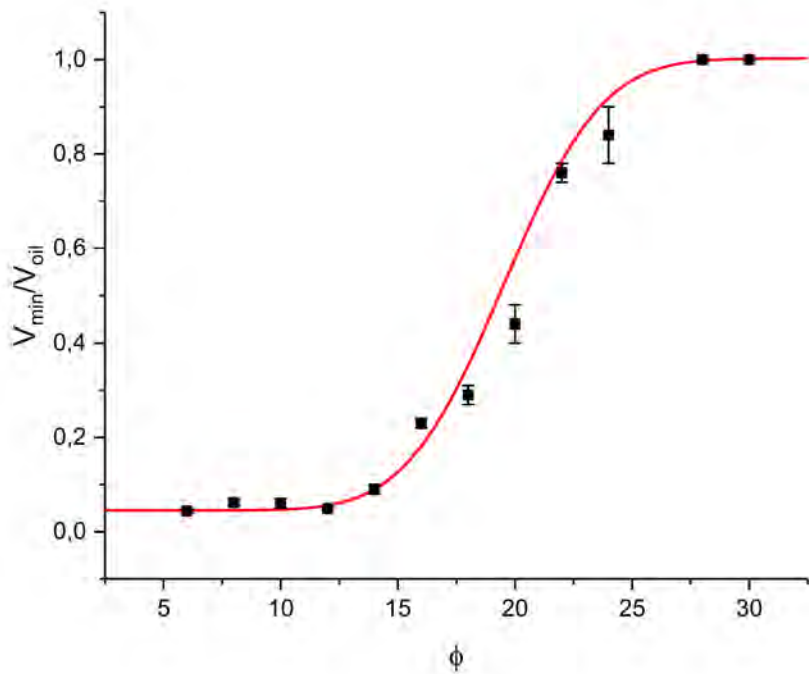


Figure 3.8: Transition from *squeezing* to *dripping* in the flow-flowing configuration.

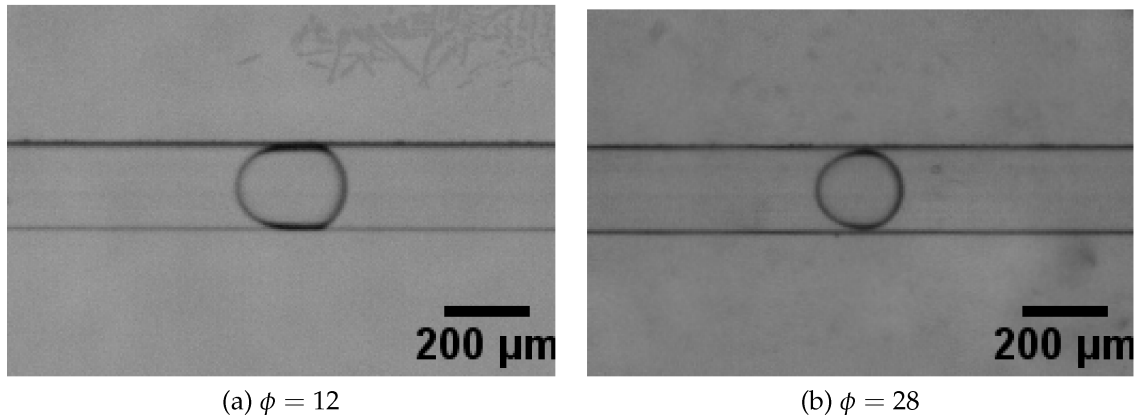


Figure 3.9: Detachement of the droplet from the channel in flow-focussing configuration. On the left the microscope image for $\phi = 12$, on the right for $\phi = 28$.

The points in Figures 3.6 and 3.8 were interpolated with an *erf* function like in equation 3.1.

$$\frac{V_{min}}{V_{oil}} = A \operatorname{erf}[B(\phi - \phi_0)] - y_0 \quad (3.1)$$

The results are reported in table 3.3 both for cross-flowing and flow-focussing configurations.

	A	B	ϕ_0	y_0
cross-flowing	0.477 ± 0.002	0.22 ± 0.02	21.1 ± 0.2	-0.525 ± 0.002
flow-focussing	0.479 ± 0.004	0.21 ± 0.02	19.5 ± 0.3	-0.524 ± 0.004
compatibility	0.4	0.4	4.4	0.2

Table 3.3: Results of the interpolation with an *erf* function $\frac{V_{min}}{V_{oil}} = A \operatorname{erf}[B(\phi - \phi_0)] - y_0$.

The compatibility between the parameters obtained by the interpolation for the two configurations is excellent. Independently from the microfluidic configuration, the overall trend and functional dependence on the physical parameters of the transitions is the same. The only difference occurs in the range of fluxes at which the transition takes place.

3.3 Droplet’s shape evolution dynamics

When the flux increase⁴ the quantity of water that is carried by the oil decrease, so the length of the droplet change (decrease). With a lower quantity of liquid available, the shape of the droplet has to change. Obviously, this modification of the form is more pronounced at very high values of flux, when the quantity of water available is so small that it can not fill completely the channel and the droplet has to arrange in

⁴When we say “flux” we mean ϕ . However, because the flux of the dispersed phase is fixed (to 10 $\mu\text{l}/\text{min}$) when we say “the flux increase” is implicit that the only thing that can change is Q_c , namely the flux of oil.

an almost spherical shape. The reasons of the particular shape of the droplet and the dynamics of its evolution as functions of the flux have not been known yet.

Practically, we must understand how the form of the advancing meniscus influences or determines the form of the bottom one. In fact the two menisci must be correlated, being part of the same droplet.

The final shape of the droplet is different from the one at the beginning (so when the droplet was formed in the T-junction). In Figure 3.10 (a) and (b) we can see this difference in the case of a flow-focussing configuration and with $\phi = 22$.

Basically, we have to wait a period of time for the complete stabilization of the shape, so we must make the optical measure far away from the T-junction.



(a) Shape of the droplet soon after the formation in the T-junction.



(b) Shape of the droplet in a successive instant to that of panel (a).

Figure 3.10: **Difference in the droplet shape at the formation.** Soon after the formation (a) the droplet has a different shape than in (b). Droplet obtained in the flow-focussing configuration with $220 \mu\text{l}/\text{min}$ of oil and $10 \mu\text{l}/\text{min}$ of water.

To understand the variation of the shape of the droplet with the flux, the measure must be carried out at a suitable distance from the cross. Otherwise, the oscillation in the shape caused by the normal relaxation of the just-formed droplet may be confused with that induced by the flow changing.

Now we can search for new observables characterizing the system.

3.3.1 Droplet as a lens

We have understood that, when the flux changes, the shape of the droplet is modified. This modification alters some physical properties of the droplets. We have just seen that the peaks in the acquisition profile are caused by the passage of the menisci. So, each meniscus behaves like a lens. In a certain sense, all the droplet behaves like a lens. To better understand this optical property of the droplet was decided to compute the integral of the entire profile for each flux⁵. With "integral" we mean the area under the acquisition profile from the first peak to the second one. In Figure 3.11 we can see an example of the area under the profile (and of the distance D , see next section).

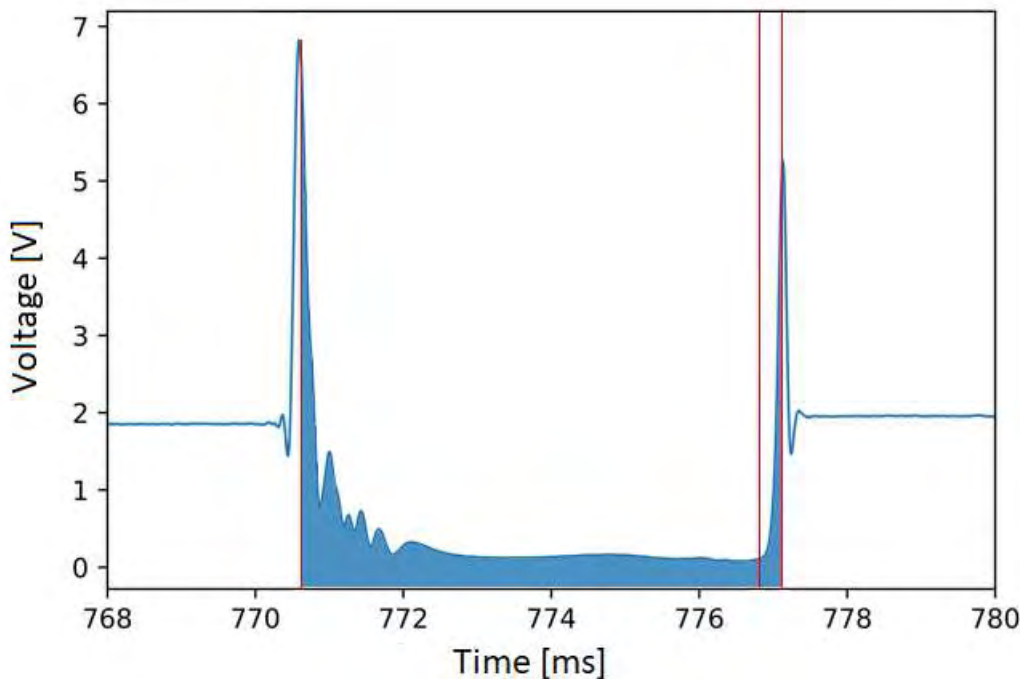


Figure 3.11: **Integral of the acquisition profile and distance D .** The blue zone is the area under the profile. The distance between the two red vertical lines is the distance D . Profile obtained in the cross-flowing configuration with $50 \mu\text{l}/\text{min}$ of oil and $10 \mu\text{l}/\text{min}$ of water.

As a matter of fact the voltage is directly proportional to the intensity transmitted, so if we compute the integral (I) we have therefore a measure of the transmitted intensity for all the period of passage of the droplet.⁶ Practically, we are measuring how much the droplet behaves like a lens.

In Figure 3.12 we can see the rescaled integral ($I_{rescaled}$) as a function of ϕ . For rescaled integral we mean

$$I_{rescaled} = \frac{I(V \cdot ms)}{V_{oil}(V)L(ms)}$$

where L is the length of the droplet (in ms , the one computed in chapter 1). Substantially, $I_{rescaled}$ is the total area divided by the area that we would compute if, for the

⁵In this section all the measure has been done in the cross-flowing configuration.

⁶In fact the unit of measure of the integral is a voltage times a time ($I = V \cdot s$).

same period of time, only oil would pass.

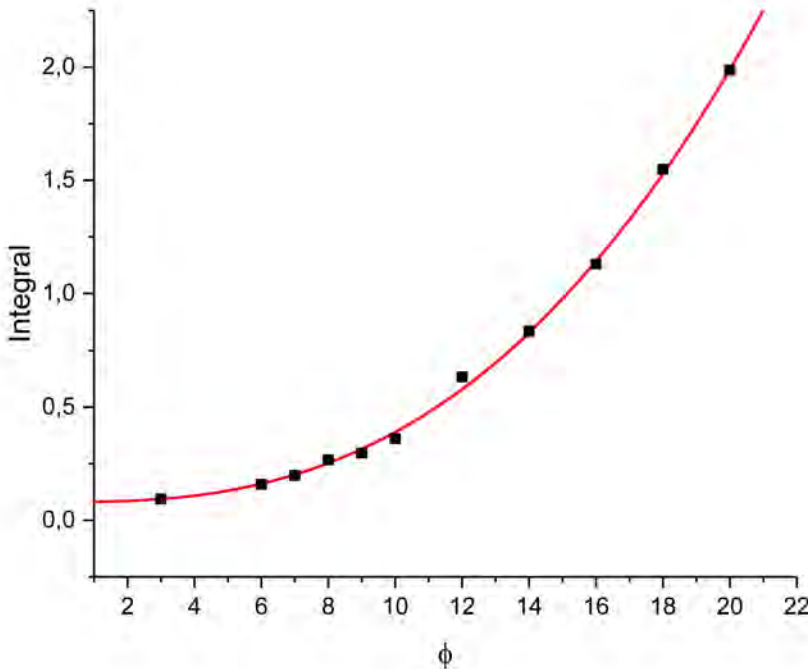


Figure 3.12: **Integral of the acquisition profile as function of the flux.** The integral is the area under the profile from the first to the second peak.

The points were interpolated with a power law

$$I_{rescaled} = A\phi^C + B \quad (3.2)$$

and the results are shown in table 3.4.

A	B	C
$7 \cdot 10^{-4} \pm 1 \cdot 10^{-4}$	0.081 ± 0.004	2.63 ± 0.05

Table 3.4: Results of the interpolation with a power law $I_{rescaled} = A\phi^C + B$.

As we can note the transmitted intensity grown as a positive power of the flux, in particular

$$I_{rescaled} \propto \phi^{2.63} \quad (3.3)$$

Substantially, the more the droplet reduces its length, the more it behaves like a lens. With increasing fluxes, the water plateau reduces and the two menisci assume a more important role in the physics of the droplet.

As we can see, when $\phi = 20$ the droplet transmits twice the optical intensity than it would do the same quantity of oil. At $\phi \sim 15$ oil and the water droplet transmits the same.

3.3.2 Spherical droplets

For a better understanding the evolution of the menisci with flux, we decided to compute the distance (D) between the minimum in the acquisition profile and the second peak (Figure 3.11). This values let us know the size of the second meniscus. If we divide D by the length of the droplet we have an estimate of the weight of the second meniscus over the length, i.e. an indicator on how much the meniscus is important for the shape. The results can be seen in Figure 3.13 for the usual two configurations.

If we look at the images taken with the microscope, the first impression is that the only meniscus that changes is the advancing one. Anyway if we look at the graphics above we can notice that also the second meniscus has an important role. As just said there is correlation between the menisci, when one of them changes the other follows.

We performed a systematical analysis to correlate this evidence with what said in § 3.2. We show that after a certain flux a transition from squeezing to dripping takes place and the process is characterized by the minimum in the potential.

This transition is important also for the description of the shape of the droplets. In fact, the detachment from the channel can take place only if the droplet has a certain shape, namely an oval one. Practically, the minimum in the acquisition profile is another important parameter to understand the shape of the droplet.

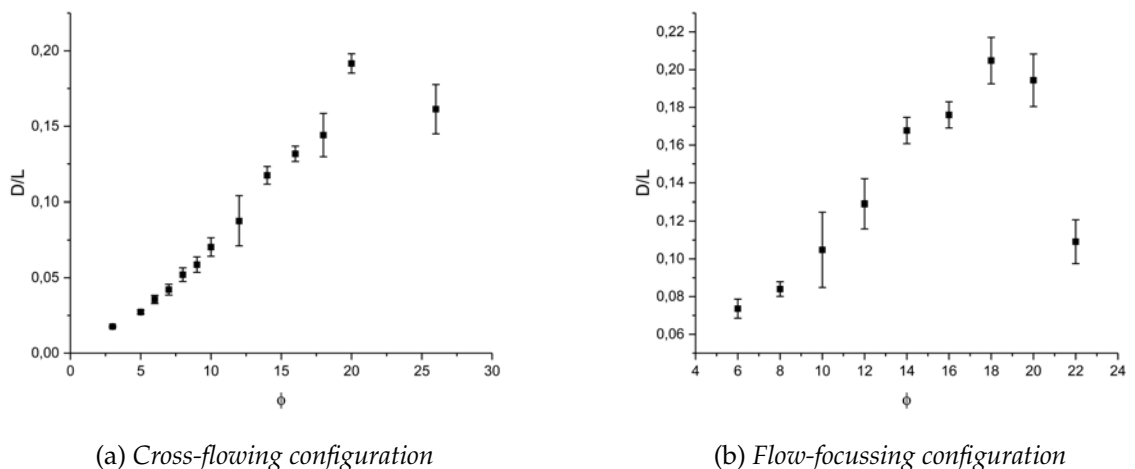


Figure 3.13: **The quantity D/L .** (a) in the cross-flowing configuration, (b) for the flow-focussing one.

We investigated what happens when the plateaux of water has disappeared, namely when $\phi > 12$ ⁷. Two relevant processes occur at the same time:

- The secondary peaks collapse on the first peak, until (for $\phi = 22$) they merge completely in an unique large peak. In Figure 3.14 we can see this process;

⁷The dynamics is the same for both the flow-focussing and cross-flowing configuration, but every example with the flux is relative to the cross-flowing configuration.

- The second peak (the second meniscus) increases its width (namely, D grows), but transmits less (namely, its height decreases). This because it begins to merge with the first peak. When the second peak is completely melted, so there is only one large peak, we can say that the droplet is spherical (for $\phi = 40$). In Figure 3.15 we can see this process.

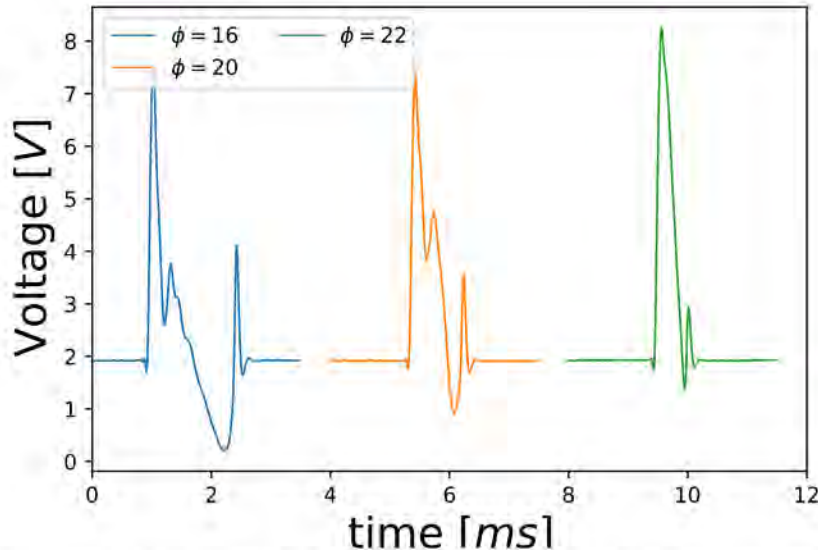


Figure 3.14: **The melding of the secondary peaks.** Acquisition profile for $\phi = 16, 20, 22$, showing the melding of the secondary peaks (acquisition taken in the cross-flowing configuration).

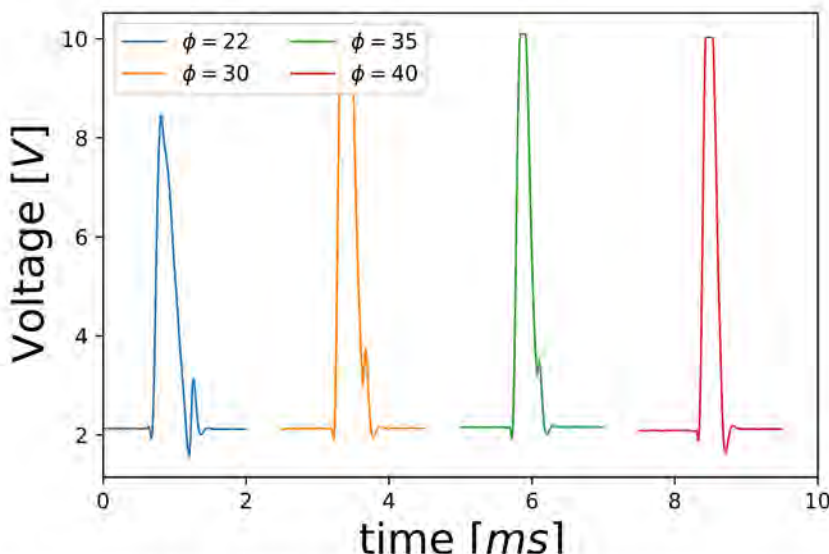


Figure 3.15: **The melding of the first with the second peak.** Acquisition profile for $\phi = 22, 30, 35, 40$, showing how the two menisci deform to create a spherical droplet (acquisition taken in the cross-flowing configuration).

When the minimum disappears we can say that the second meniscus does not exist alone anymore, but it is a continuum with the first one. Substantially, the droplet is assuming an oval form and the two menisci are directly connected in a continuous way. This implies that the bottom meniscus must "stretch" towards the first one (this means that it must grow) and this is sealed by the Figure 3.13. Exactly in these plots we can notice a strange behaviour. For $\phi = 26$ and $\phi = 22$, respectively for the cross-flowing and flow-focussing configurations, the values of D/L decrease after a quite good linear growth. This may be due to the fact that the droplet is going to detach from the channel and the second peak begins to merge with the first one. In this region of fluxes we have just said that the second meniscus does not exist anymore, so D/L may assume another role.⁸

Anyway, when the two peaks collapse in an unique one, there are no more differences between the two menisci and consequently the droplet assumes a spherical shape.

3.4 Reconstruction of droplet shape

In conclusion we summarize the experimental evidence. The systematic analysis on the shape of droplet depending on fluxes and the effects on optical intensity transmission allowed to define fingerprints in the recorded spectra never reported in literature.

By referring to Figures 3.16 (for low fluxes, in the cross-flowing configuration) and 3.17 (for high fluxes, in the flow-focussing configuration), we want to give a scheme that gives a comparison between every part of the droplet and its acquisition profile. The figures are divided in zones, colored in a different way. Every zone in the acquisition profile (panel (a) in the figures) is related (by the color) to one in the image of the droplet taken with the microscope (panel (b)).

- **The green zone** is the second peak and is associated to the bottom meniscus of the droplet. It is the most intuitive part of the droplet and the most appropriate for a simulation, for the reason explained in §1.1 (its form is more approximable to an ellipse than the one of the first peak);
- **The blue zone** is the plateaux of water, so the zone that, in the acquisition profile, is at a constant and low value of voltage. In the droplet, instead, is the zone where the water "touches" the channel's sides.⁹ The section of this part of droplet can be seen in Figure 2.23 in the second chapter;
- **The orange and red zones** are associated to the advancing meniscus. Both with $\phi = 5$ and $\phi = 14$ the red zone (the peak in the acquisition profile) is relative to the so called "geometrical part" of the meniscus, so the one that is reproduced by the code in Chapter 2. The orange part, instead, is more complex. In Figure 3.16 (b) one can confuse the zone of the secondary peak with the plateaux of water. In fact, with the naked eye, it is almost impossible to distinguish them in

⁸Moreover, the calculation of D/L is quite difficult from a computational point of view. In fact, the code that analyses the experimental data has to detect very small distance and it is easy to fool it. This is the reason also for the big error in the data. Anyway the computational analysis for this kind of measure is improving and we hope to obtain better results in the future.

⁹There should be the microfilm of oil between the droplet and the channel, but, as just said in chapter 2, we neglet it.

the microscope image. It is only because we are aware that such a zone must exist that we can observe the difference. On the contrary, when the droplet becomes enough small the difference can be noted (Figure 3.17 (b)).

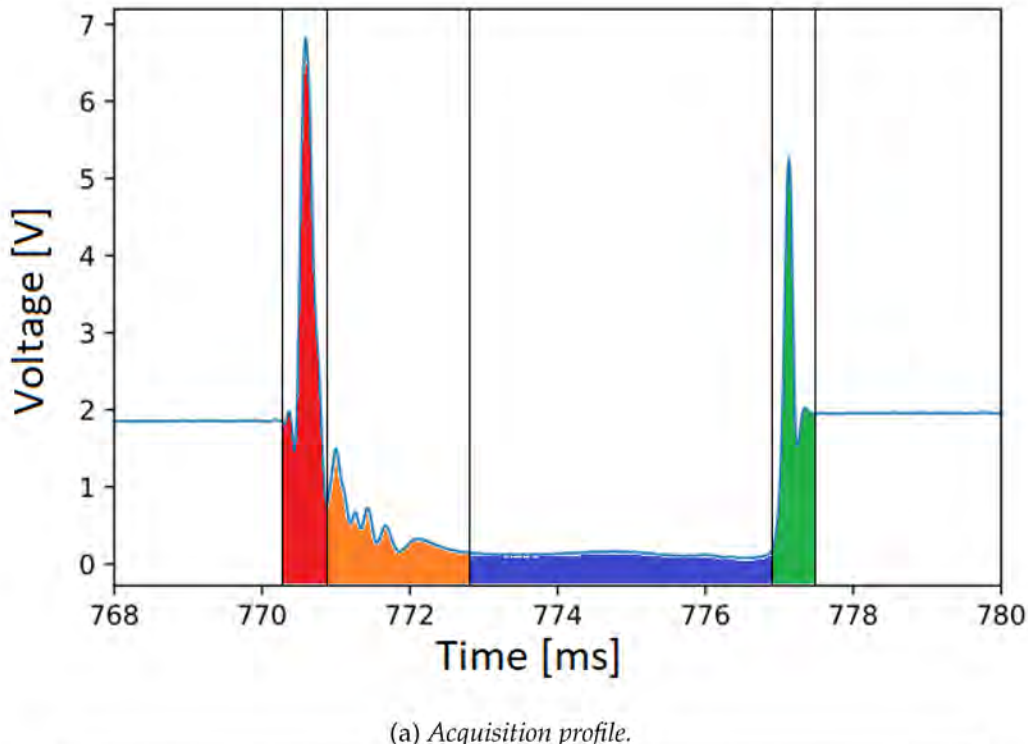
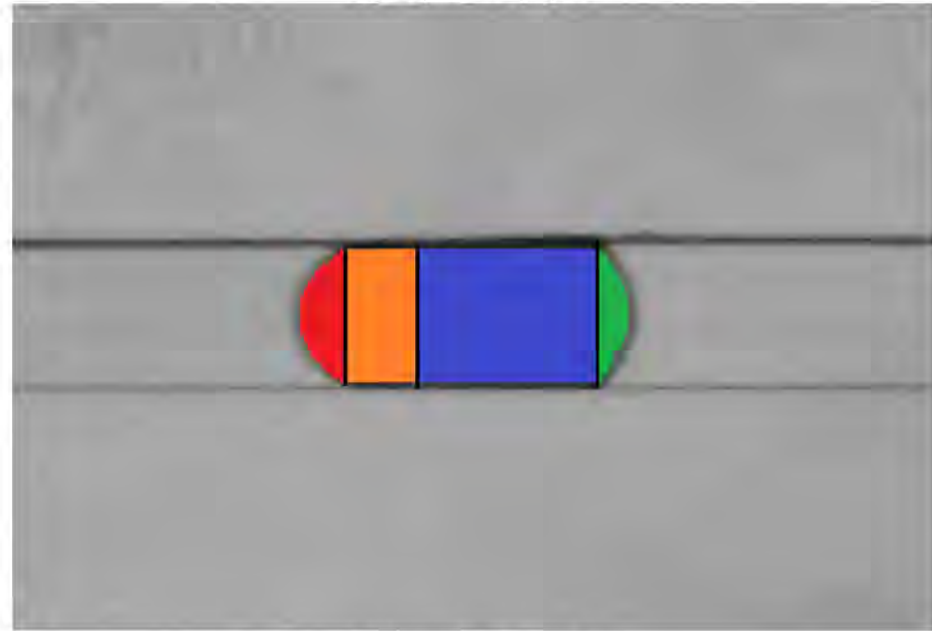
(a) *Acquisition profile.*(b) *Image of the droplet.*

Figure 3.16: Acquisition profile and image of the droplet for $\phi = 5$ in the cross-flowing configuration. The green zone in the acquisition profile (a) represents the bottom meniscus of the droplet, the blue one the plateaux of water, the orange and the red ones the two parts of the advancing meniscus. The red zone is the "geometrical part" of the first meniscus, the one that we are able to simulate using an elliptical droplet, the orange one (the secondary peaks) the part of the meniscus that lay down on the channel. The colored zones in the image of the droplet (b) are the one associated to the same color in the acquisition profile.

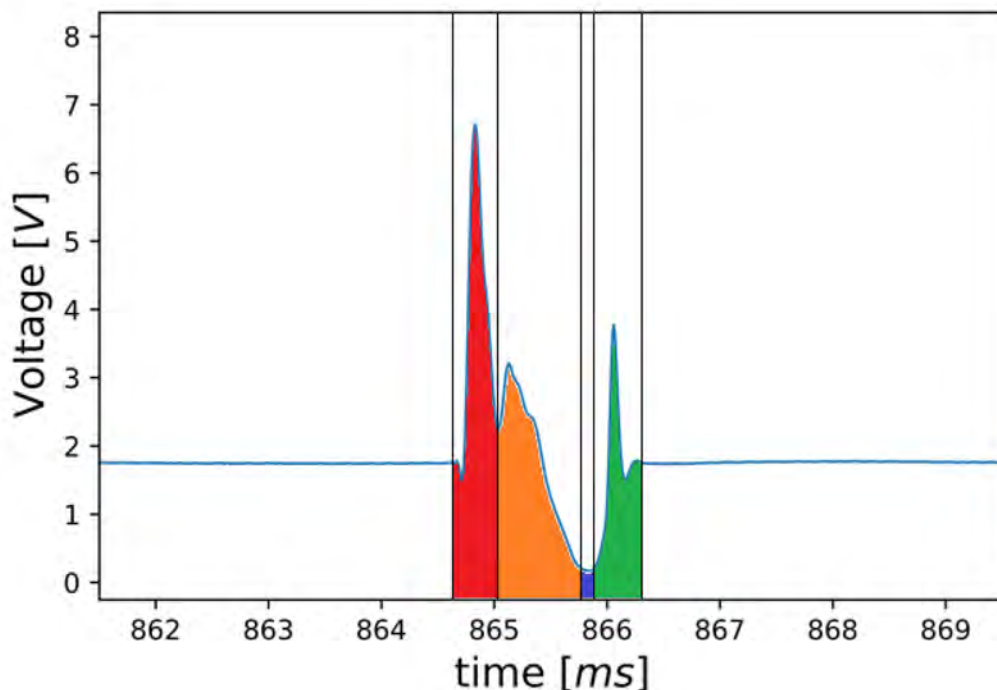
(a) *Acquisition profile.*(b) *Image of the droplet.*

Figure 3.17: Acquisition profile and image of the droplet for $\phi = 14$ in the flow-flowing configuration. The associations between colors and zones of the acquisition profile (or droplet), are the same of Figure 3.16. We can note that the plateaux of water is limited to a very small zone of the droplet.

Conclusion

This thesis aimed to study the interaction of light, coming from an optical waveguide, with a droplet moving in a microfluidic channel. The final objective was to find fingerprints able to identify the droplet passage, so that to estimate its length with perspectives of setting up an automatized and fast data analysis procedure, exploiting an integrated opto-microfluidic device, independent from the standard imagining processes. In fact, the classic analysis, commonly uses microscopes, image recording and post-processing which need a continuous calibration of the acquisition parameters that can not be pre-selected. Instead, with the optofluidic method the analysis is automated, since the acquisition rate depends only on detector (photodiode) and electronics.

In order to reach this objective, the interaction of light with the droplet was simulated by a 2D ray optics approach in order to evaluate the optical transmission across the droplet by a light intensity profile spanning that experimentally observed. The simulation was compared to the experimental measures of different shaped droplets of water dispersed in oil in different microfluidic regimes and configurations.

Moreover, a systematic analysis of the physical parameters' correlation effect with the droplet transmission was carried out, with special care of the role of the flux ratio between the continuous and the dispersed phases $\phi = \frac{Q_c}{Q_d}$.

The main results of this work can be summarised as follows:

1. demonstration that the droplet length L as a function of ϕ follows a power law over a wide range of fluxes ratio. This result represents an advance with respect to already published works, where predictions claimed a linear dependence;
2. the optical transmitted intensity contains fingerprints of the geometrical shape of a given droplet. In the optical transmission recorded by way of the opto-microfluidic set-up, in fact, we demonstrated that the major peaks in the intensity profile are the direct result of the lens effect of the droplet meniscus.

The code developed within this work, in fact, simulates the interaction between the waveguided light and the droplet, adopting some hypothesis like ray optic, and a 2D description of the dynamic. The results was that the refracted (from the droplet) and directed rays interfere when reaching the waveguide facing on the other side of the channel and the constructive interference produces an increase in the transmitted intensity.

Basically, the peaks in transmitted optical intensity are due to the geometry of

the meniscus.

Moreover, we analyse all the central zone of the droplet, divided in two parts: the *water plateau* and the *secondary peaks*. Another software was written to simulate the plateau of water, that is intuitively associated to the center of the droplet. A particular section for a long droplet was chosen in order to reproduce its center and the same interaction of the previous code was performed. The result was that the transmitted optical intensity corresponding to the middle of the droplet is due to the geometrical shape of the interface water-oil, exactly as for the peak in intensity. For the secondary peaks a phenomenological analysis shows that they are essentially the continuation of the advancing meniscus. Essentially, the receding and advancing meniscus have a different curvature: the first can be fitted with an ellipsoid and has a well defined shape; the second, instead, tends to lay down on the channel walls. This is reflected in the optical transmission profile, where the second peak (representing the receding meniscus) suddenly rise from the plateau of water, whereas the first peak (representing the advancing meniscus) is softened by a modulation that produces the secondary peaks. This phenomenological observation is demonstrated observing the optical intensity profiles of long droplets, where, thanks to its symmetry (advancing and receding meniscus are almost equal in shape), we expect to find no secondary peak. The experimental data confirm what we predicted and the role of the secondary peak was therefore established;

3. sensibility of the optical transmitted light from the overall geometrical shape of the droplet. This conclusion was got by comparing the optical transmitted light with a synchronous acquisition of the shape of the droplets by way of standard optical microscopy and fast imagining recording. The analysis of the data over a wide range of ϕ ($3 < \phi < 40$) showed that the more flux increases, the more every parts of the optical transmitted profile changes corresponding to different geometrical shape assumed by the droplet at different ϕ values. At the beginning, the plateau of water shrinks until it disappears ($\phi \sim 12$). For $12 < \phi < 26$ the minimum value of the optical transmitted signal increases and the secondary peaks merge together. For $\phi > 26$, all the remaining peaks begins to merge, until only one remains. The one-to-one comparison, with the correspondent microscope image of the droplets at the same value of flux, let us understand that the minimum is associated to a transition between the squeezing and the dripping regimes. The classical oval form of a short droplet, begins to be almost spherical for $\phi \sim 40$ and this means that the unique peak of the intensity profile is associated to such a shape of the droplet. The transition was shown plotting the minimum points (accurately normalized at the oil's signal) as function of the fluxes ratio ϕ and interpolating them with an error function. The interesting aspect of the transition is that it is the same for both the cross-flowing and flow-focussing configurations, i.e. the interpolation with an error function for both configurations given compatible results. In flow-focussing a lower value of ϕ is needed for the detachment of the droplet from the channel wall ($\phi \sim 28$ instead of $\phi \sim 30$ for cross-flowing), but anyway the trend of the transition is the same.

Bibliography

- [1] Eric K Sackmann, Anna L Fulton, and David J Beebe. The present and future role of microfluidics in biomedical research. *Nature*, 507(7491):181, 2014.
- [2] A Liga, ADB Vliegenthart, W Oosthuyzen, JW Dear, and M Kersaudy-Kerhoas. Exosome isolation: a microfluidic road-map. *Lab on a Chip*, 15(11):2388–2394, 2015.
- [3] Daiying Zhang, Liqiu Men, and Qiying Chen. Microfabrication and applications of opto-microfluidic sensors. *Sensors*, 11(5):5360–5382, 2011.
- [4] Kin Fong Lei. Microfluidic systems for diagnostic applications: A review. *Journal of laboratory automation*, 17(5):330–347, 2012.
- [5] Günter Gauglitz. Point-of-care platforms. *Annual review of analytical chemistry*, 7: 297–315, 2014.
- [6] Jong-ryul Choi, Hyerin Song, Jong Hwan Sung, Donghyun Kim, and Kyujung Kim. Microfluidic assay-based optical measurement techniques for cell analysis: A review of recent progress. *Biosensors and Bioelectronics*, 77:227–236, 2016.
- [7] Jonathan P McMullen and Klavs F Jensen. Integrated microreactors for reaction automation: new approaches to reaction development. *Annual review of analytical chemistry*, 3:19–42, 2010.
- [8] P Abgrall and AM Gue. Lab-on-chip technologies: making a microfluidic network and coupling it into a complete microsystem—a review. *Journal of Micromechanics and Microengineering*, 17(5):R15, 2007.
- [9] Howard A Stone, Abraham D Stroock, and Armand Ajdari. Engineering flows in small devices: microfluidics toward a lab-on-a-chip. *Annu. Rev. Fluid Mech.*, 36:381–411, 2004.
- [10] Paul Watts and Stephen J Haswell. The application of micro reactors for organic synthesis. *Chemical Society Reviews*, 34(3):235–246, 2005.
- [11] C Monat, P Domachuk, and BJ Eggleton. Integrated optofluidics: A new river of light. *Nature photonics*, 1(2):106–114, 2007.

- [12] Pavel Neuží, Stefan Giselbrecht, Kerstin Länge, Tony Jun Huang, and Andreas Manz. Revisiting lab-on-a-chip technology for drug discovery. *Nature reviews. Drug discovery*, 11(8):620, 2012.
- [13] Vijay Srinivasan, Vamsee K Pamula, and Richard B Fair. An integrated digital microfluidic lab-on-a-chip for clinical diagnostics on human physiological fluids. *Lab on a Chip*, 4(4):310–315, 2004.
- [14] Lin Pang, H Matthew Chen, Lindsay M Freeman, and Yeshaiahu Fainman. Optofluidic devices and applications in photonics, sensing and imaging. *Lab on a Chip*, 12(19):3543–3551, 2012.
- [15] Jochen Guck, Revathi Ananthakrishnan, Hamid Mahmood, Tess J Moon, C Casey Cunningham, and Josef Käs. The optical stretcher: a novel laser tool to micromanipulate cells. *Biophysical journal*, 81(2):767–784, 2001.
- [16] Revathi Ananthakrishnan, Jochen Guck, Falk Wottawah, Stefan Schinkinger, Bryan Lincoln, Maren Romeyke, Tess Moon, and Josef Käs. Quantifying the contribution of actin networks to the elastic strength of fibroblasts. *Journal of theoretical biology*, 242(2):502–516, 2006.
- [17] Bryan Lincoln, Stefan Schinkinger, Kort Travis, Falk Wottawah, Susanne Ebert, Frank Sauer, and Jochen Guck. Reconfigurable microfluidic integration of a dual-beam laser trap with biomedical applications. *Biomedical microdevices*, 9(5):703–710, 2007.
- [18] Pietro Cicuta and Athene M Donald. Microrheology: a review of the method and applications. *Soft Matter*, 3(12):1449–1455, 2007.
- [19] Ning Wang, James P Butler, and Donald E Ingber. Mechanotransduction across the cell surface and through the cytoskeleton. *Science*, pages 1124–1127, 1993.
- [20] David N Breslauer, Philip J Lee, and Luke P Lee. Microfluidics-based systems biology. *Molecular Biosystems*, 2(2):97–112, 2006.
- [21] Christopher E Sims and Nancy L Allbritton. Analysis of single mammalian cells on-chip. *Lab on a Chip*, 7(4):423–440, 2007.
- [22] Leonard J Blackwell, Steve Birkos, Rhonda Hallam, Gretchen Van De Carr, Jamie Arroway, Carla M Suto, and William P Janzen. High-throughput screening of the cyclic amp-dependent protein kinase (pka) using the caliper microfluidic platform. *High Throughput Screening: Methods and Protocols, Second Edition*, pages 225–237, 2009.
- [23] Genni Testa, Gianluca Persichetti, Pasqualina M Sarro, and Romeo Bernini. A hybrid silicon-pdms optofluidic platform for sensing applications. *Biomedical optics express*, 5(2):417–426, 2014.
- [24] Martha-Elizabeth Baylor, Benjamin W Cerjan, Charlotte R Pfiefer, Robert W Boyne, Charles L Couch, Neil B Cramer, Christopher N Bowman, and Robert R McLeod. Monolithic integration of optical waveguide and fluidic channel structures in a thiol-ene/methacrylate photopolymer. *Optical Materials Express*, 2(11):1548–1555, 2012.

- [25] Francesca Bragheri, Lorenzo Ferrara, Nicola Bellini, Krishna C Vishnubhatla, Paolo Minzioni, Roberta Ramponi, Roberto Osellame, and Ilaria Cristiani. Optofluidic chip for single cell trapping and stretching fabricated by a femtosecond laser. *Journal of biophotonics*, 3(4):234–243, 2010.
- [26] N Bellini, KC Vishnubhatla, F Bragheri, L Ferrara, P Minzioni, R Ramponi, I Cristiani, and R Osellame. Femtosecond laser fabricated monolithic chip for optical trapping and stretching of single cells. *Optics Express*, 18(5):4679–4688, 2010.
- [27] Rafael R Gattass and Eric Mazur. Femtosecond laser micromachining in transparent materials. *Nature photonics*, 2(4):219–225, 2008.
- [28] G Della Valle, R Osellame, and P Laporta. Micromachining of photonic devices by femtosecond laser pulses. *Journal of Optics A: Pure and Applied Optics*, 11(1):013001, 2008.
- [29] Valeria Maselli, Roberto Osellame, Giulio Cerullo, Roberta Ramponi, Paolo Laporta, Luca Magagnin, and Pietro Luigi Cavallotti. Fabrication of long microchannels with circular cross section using astigmatically shaped femtosecond laser pulses and chemical etching. *Applied physics letters*, 88(19):191107, 2006.
- [30] Venkatachalam Chokkalingam, Boris Weidenhof, Michael Krämer, Wilhelm F Maier, Stephan Herminghaus, and Ralf Seemann. Optimized droplet-based microfluidics scheme for sol–gel reactions. *Lab on a Chip*, 10(13):1700–1705, 2010.
- [31] Paul Watts and Stephen J Haswell. The application of micro reactors for organic synthesis. *Chemical Society Reviews*, 34(3):235–246, 2005.
- [32] Gordon F Christopher and Shelly L Anna. Microfluidic methods for generating continuous droplet streams. *Journal of Physics D: Applied Physics*, 40(19):R319, 2007.
- [33] Mandy LY Sin, Jian Gao, Joseph C Liao, and Pak Kin Wong. System integration—a major step toward lab on a chip. *Journal of biological engineering*, 5(1):6, 2011.
- [34] M Chauvet, L Al Fares, B Guichardaz, F Devaux, and S Ballandras. Integrated optofluidic index sensor based on self-trapped beams in linbo₃. *Applied Physics Letters*, 101(18):181104, 2012.
- [35] Bor-Shyh Lin, Yu-Ching Yang, Chong-Yi Ho, Han-Yu Yang, and Hsiang-Yu Wang. A pdms-based cylindrical hybrid lens for enhanced fluorescence detection in microfluidic systems. *Sensors*, 14(2):2967–2980, 2014.
- [36] Marco Bazzan and Cinzia Sada. Optical waveguides in lithium niobate: Recent developments and applications. *Applied Physics Reviews*, 2(4):040603, 2015.
- [37] Tatyana Volk and Manfred Wöhlecke. *Lithium niobate: defects, photorefraction and ferroelectric switching*, volume 115. Springer Science & Business Media, 2008.
- [38] Giacomo Bettella. *Integrated Opto-Microfluidic Lab-on-a-Chip in Lithium Niobate for Droplet Generation and Sensing*. PhD thesis, Department of Physics in Università degli Studi di Padova, 9 2015.

- [39] Flavie Sarrazin, Karine Loubiere, Laurent Prat, Christophe Gourdon, Thomas Bonometti, and Jacques Magnaudet. Experimental and numerical study of droplets hydrodynamics in microchannels. *AICHE Journal*, 52(12):4061–4070, 2006.
- [40] Flavie Sarrazin, Thomas Bonometti, Laurent Prat, Christophe Gourdon, and Jacques Magnaudet. Hydrodynamic structures of droplets engineered in rectangular micro-channels. *Microfluidics and Nanofluidics*, 5(1):131–137, 2008.
- [41] Lucie Campagnolo, Milan Nikolić, Julien Perchoux, Yah Leng Lim, Karl Bertling, Karine Loubiere, Laurent Prat, Aleksandar D Rakić, and Thierry Bosch. Flow profile measurement in microchannel using the optical feedback interferometry sensing technique. *Microfluidics and Nanofluidics*, 14(1-2):113–119, 2013.
- [42] Shufang Zhao, Antoine Riaud, Guangsheng Luo, Yong Jin, and Yi Cheng. Simulation of liquid mixing inside micro-droplets by a lattice boltzmann method. *Chemical Engineering Science*, 131:118–128, 2015.
- [43] Todd Thorsen, Richard W Roberts, Frances H Arnold, and Stephen R Quake. Dynamic pattern formation in a vesicle-generating microfluidic device. *Physical review letters*, 86(18):4163, 2001.
- [44] M Chauvet, L Al Fares, B Guichardaz, F Devaux, and S Ballandras. Integrated optofluidic index sensor based on self-trapped beams in linbo₃. *Applied Physics Letters*, 101(18):181104, 2012.
- [45] Maartje LJ Steegmans, Jolet De Ruiter, Karin GPH Schroën, and Remko M Boom. A descriptive force-balance model for droplet formation at microfluidic y-junctions. *AICHE journal*, 56(10):2641–2649, 2010.
- [46] Piotr Garstecki, Michael J Fuerstman, Howard A Stone, and George M Whitesides. Formation of droplets and bubbles in a microfluidic t-junctionscaling and mechanism of break-up. *Lab on a Chip*, 6(3):437–446, 2006.
- [47] M De Menech, P Garstecki, F Jousse, and HA Stone. Transition from squeezing to dripping in a microfluidic t-shaped junction. *Journal of fluid mechanics*, 595: 141–161, 2008.
- [48] Gordon F Christopher, N Nadia Noharuddin, Joshua A Taylor, and Shelley L Anna. Experimental observations of the squeezing-to-dripping transition in t-shaped microfluidic junctions. *Physical Review E*, 78(3):036317, 2008.
- [49] Howard A Stone. On lubrication flows in geometries with zero local curvature. *Chemical engineering science*, 60(17):4838–4845, 2005.
- [50] G Pozza, S Kroesen, G Bettella, A Zaltron, M Esseling, G Mistura, P Sartori, E Chiarello, M Pierno, C Denz, et al. T-junction droplet generator realised in lithium niobate crystals by laser ablation. *Optofluidics, Microfluidics and Nanofluidics*, 1(1), 2014.
- [51] Riccardo Zamboni. Optofluidic application of a mach-zehnder interferometer integrated in lithium niobate for droplet sensing. Master’s thesis, Department of Physics in Università degli Studi di Padova, 9 2016.

- [52] H Hu, R Ricken, W Sohler, and RB Wehrspohn. Lithium niobate ridge waveguides fabricated by wet etching. *IEEE Photonics Technology Letters*, 19(6):417–419, 2007.
- [53] Masashi Tamura and Shinzo Yoshikado. Etching characteristics of linbo 3 crystal by fluorine gas plasma reactive ion etching. *Science and Technology of Advanced Materials*, 2(3):563–569, 2001.
- [54] Z Ren, PJ Heard, Joseph Michael Marshall, Pam A Thomas, and S Yu. Etching characteristics of linbo 3 in reactive ion etching and inductively coupled plasma. *Journal of applied physics*, 103(3):034109, 2008.
- [55] F. A. Stevie, L. A. Giannuzzi, B. I. Prenitzer (auth.), Lucille A. Giannuzzi, and Fred A. Stevie (eds.). *Introduction to focused ion beams: instrumentation, theory, techniques and practice*. Springer US, 1 edition, 2005.
- [56] G Della Valle, R Osellame, and P Laporta. Micromachining of photonic devices by femtosecond laser pulses. *Journal of Optics A: Pure and Applied Optics*, 11(1):013001, 2008.
- [57] Rafael R Gattass and Eric Mazur. Femtosecond laser micromachining in transparent materials. *Nature photonics*, 2(4):219–225, 2008.
- [58] Zeyad Yousif Abdoon Al-Shibaany, John Hedley, Dehong Huo, and Zhongxu Hu. Micromachining lithium niobate for rapid prototyping of resonant biosensors. 65(1):012030, 2014.
- [59] G Bettella, G Pozza, A Zaltron, MV Ciampolillo, N Argiolas, C Sada, M Chauvet, and B Guichardaz. Integrated opto-microfluidics platforms in lithium niobate crystals for sensing applications. In *Proc. SPIE*, volume 9365, page 936517, 2015.
- [60] John Shipley Rowlinson and Benjamin Widom. *Molecular theory of capillarity*. Courier Corporation, 2013.
- [61] Kock-Yee Law and Hong Zhao. *Surface wetting: characterization, contact angle, and fundamentals*. Springer, 2015.
- [62] Kiyomasa Sugii, Masaharu Fukuma, and Hiroshi Iwasaki. A study on titanium diffusion into linbo 3 waveguides by electron probe analysis and x-ray diffraction methods. *Journal of Materials Science*, 13(3):523–533, 1978.
- [63] RV Schmidt and IP Kaminow. Metal-diffused optical waveguides in linbo3. *Applied Physics Letters*, 25(8):458–460, 1974.
- [64] Yu N Korkishko and Vyacheslav A Fedorov. *Ion exchange in single crystals for integrated optics and optoelectronics*. Cambridge Int Science Publishing, 1999.
- [65] F. Chen, Xl. Wang, and KM. Wang. Development of ion-implanted optical waveguides in optical materials: A review. *Optical materials*, 29(11):1523–1542, 2007.

- [66] Ovidio Peña-Rodríguez, José Olivares, Mercedes Carrascosa, Ángel García-Cabañas, Antonio Rivera, and Fernando Agulló-López. Optical waveguides fabricated by ion implantation/irradiation: A review. *Ion Implantation, Prof. Mark Goorsky (Ed.), ISBN*, pages 978–953, 2012.
- [67] GG Bentini, M Bianconi, L Correra, M Chiarini, P Mazzoldi, C Sada, N Argiolas, M Bazzan, and R Guzzi. Damage effects produced in the near-surface region of x-cut linbo₃ by low dose, high energy implantation of nitrogen, oxygen, and fluorine ions. *Journal of applied physics*, 96(1):242–247, 2004.
- [68] JJ. Yin, F. Lu, and XB. et al Ming. Theoretical modeling of refractive index in ion implanted LiNbO₃ waveguides. *Journal of Applied Physics*, 108(3):033105, 2010.
- [69] K. Itoh, O. Matobe, and Y. Ichioka. Fabrication experiment of photorefractive three-dimensional waveguides in lithium niobate. *Optics Letters*, 19(9):652–654, 1994.
- [70] Jonas Burghoff, Christian Grebing, Stefan Nolte, and Andreas Tünnermann. Waveguides in lithium niobate fabricated by focused ultrashort laser pulses. *Applied surface science*, 253(19):7899–7902, 2007.
- [71] Thomas Cubaud and Thomas G Mason. Capillary threads and viscous droplets in square microchannels. *Physics of Fluids*, 20(5):053302, 2008.
- [72] Bahaa. E. A. Saleh and Malvin Carl Teich. *Fundamentals of photonics*. Wiley Interscience, Canada, 1991.
- [73] Axel Huerre, Olivier Theodoly, Alexander M Leshansky, Marie-Pierre Valignat, Isabelle Cantat, and Marie-Caroline Jullien. Droplets in microchannels: dynamical properties of the lubrication film. *Physical review letters*, 115(6):064501, 2015.
- [74] A Huerre, M-C Jullien, O Theodoly, and M-P Valignat. Absolute 3d reconstruction of thin films topography in microfluidic channels by interference reflection microscopy. *Lab on a Chip*, 16(5):911–916, 2016.
- [75] Olivier Theodoly, Z-H Huang, and M-P Valignat. New modeling of reflection interference contrast microscopy including polarization and numerical aperture effects: application to nanometric distance measurements and object profile reconstruction. *Langmuir*, 26(3):1940–1948, 2009.
- [76] Pijush K. Kundu, Ira M. Cohen, and D. R. Dowling. *Fluid Mechanics 6th*. Elsevier, Oxford, 2016.
- [77] RS Weis and TK Gaylord. Lithium niobate: summary of physical properties and crystal structure. *Applied Physics A: Materials Science & Processing*, 37(4):191–203, 1985.
- [78] Carlo Montevercchi. Integrated opto-microfluidic lab-on-a-chip in lithium niobate for sensing applications. Master's thesis, Department of Physics in Università degli Studi di Padova, 3 2015.

- [79] Nam-Trung Nguyen, Sumantri Lassemmono, and Franck Alexis Chollet. Optical detection for droplet size control in microfluidic droplet-based analysis systems. *Sensors and actuators B: Chemical*, 117(2):431–436, 2006.
- [80] Yu-Wen Hsieh, An-Bang Wang, Xuan-Yi Lu, and Lon A Wang. High-throughput on-line multi-detection for refractive index, velocity, size, and concentration measurements of micro-two-phase flow using optical microfibers. *Sensors and Actuators B: Chemical*, 237:841–848, 2016.
- [81] Benjamín Vazquez, Naser Qureshi, Laura Oropeza-Ramos, and Luis F Olguin. Effect of velocity on microdroplet fluorescence quantified by laser-induced fluorescence. *Lab on a Chip*, 14(18):3550–3555, 2014.
- [82] Gavin DM Jeffries, Robert M Lorenz, and Daniel T Chiu. Ultrasensitive and high-throughput fluorescence analysis of droplet contents with orthogonal line confocal excitation. *Analytical chemistry*, 82(23):9948–9954, 2010.
- [83] Nathalie Di Miceli Raimondi, Laurent Prat, Christophe Gourdon, and Patrick Cognet. Direct numerical simulations of mass transfer in square microchannels for liquid–liquid slug flow. *Chemical Engineering Science*, 63(22):5522–5530, 2008.
- [84] Xiaoming Chen, Tomasz Glawdel, Naiwen Cui, and Carolyn L Ren. Model of droplet generation in flow focusing generators operating in the squeezing regime. *Microfluidics and Nanofluidics*, 18(5-6):1341–1353, 2015.
- [85] Xiao-Bin Li, Feng-Chen Li, Juan-Cheng Yang, Haruyuki Kinoshita, Masamichi Oishi, and Marie Oshima. Study on the mechanism of droplet formation in t-junction microchannel. *Chemical engineering science*, 69(1):340–351, 2012.
- [86] Maartje LJ Steegmans, Jolet De Ruiter, Karin GPH Schroën, and Remko M Boom. A descriptive force-balance model for droplet formation at microfluidic y-junctions. *AICHE journal*, 56(10):2641–2649, 2010.
- [87] Manfred Radmacher. 4.-measuring the elastic properties of living cells by the atomic force microscope. *Methods in cell biology*, 68(1):67–90, 2002.
- [88] Liron Stern, Avraham Bakal, Mor Tzur, Maya Veinguer, Noa Mazurski, Nadav Cohen, and Uriel Levy. Doppler-based flow rate sensing in microfluidic channels. *Sensors*, 14(9):16799–16807, 2014.
- [89] Karan VIS Kaler and Ravi Prakash. Droplet microfluidics for chip-based diagnostics. *Sensors*, 14(12):23283–23306, 2014.
- [90] N Craig Carville, Liam Collins, Michele Manzo, Katia Gallo, Bart I Lukasz, Katey K McKayed, Jeremy C Simpson, and Brian J Rodriguez. Biocompatibility of ferroelectric lithium niobate and the influence of polarization charge on osteoblast proliferation and function. *Journal of Biomedical Materials Research Part A*, 103(8):2540–2548, 2015.